

SUSY QCD one-loop effects in (un)polarized top-pair production at hadron colliders

Stefan Berge,^{1*} Wolfgang Hollik,^{2†} Wolf M. Mosle,[‡] and Doreen Wackeroth,^{3§}

¹*Institut für Theoretische Physik, RWTH Aachen, D-52056 Aachen, Germany*

²*Max-Planck-Institut für Physik (Werner-Heisenberg-Institut),*

Föhringer Ring 6, D-80805 Munich, Germany

³*Department of Physics, University at Buffalo,*

The State University of New York, Buffalo, NY 14260-1500, U.S.A.

(Dated: July 4, 2018)

Abstract

We study the effects of $\mathcal{O}(\alpha_s)$ supersymmetric QCD (SQCD) corrections on the total production rate and kinematic distributions of polarized and unpolarized top-pair production in pp and $p\bar{p}$ collisions. At the Fermilab Tevatron $p\bar{p}$ collider, top-quark pairs are mainly produced via quark-antiquark annihilation, $q\bar{q} \rightarrow t\bar{t}$, while at the CERN LHC pp collider gluon-gluon scattering, $gg \rightarrow t\bar{t}$, dominates. We compute the complete set of $\mathcal{O}(\alpha_s)$ SQCD corrections to both production channels and study their dependence on the parameters of the Minimal Supersymmetric Standard Model. In particular, we discuss the prospects for observing strong, loop-induced SUSY effects in top-pair production at the Tevatron Run II and the LHC.

PACS numbers: 12.38.Bx, 12.60.Jv, 13.60.Hb, 14.65.Ha

* E-mail: berge@physik.rwth-aachen.de

† E-mail: hollik@mppmu.mpg.de

‡ now at MicroStrategy, Inc.

§ E-mail: dow@ubpheno.physics.buffalo.edu

I. INTRODUCTION

Since the discovery of the top quark at the Fermilab Tevatron $p\bar{p}$ collider in 1995 [1, 2], the top-physics program has shifted to precisely studying its properties. The high top-quark yields at the Tevatron Run II and the CERN LHC pp collider open a new, rich field of top-quark phenomenology, which may enable a precision physics program with top-quark observables, in the spirit of the successful LEP/SLC studies of precision Z boson observables [3].

The Standard Model (SM) of electroweak and strong interactions has seen impressive experimental confirmation. However, the Higgs boson, which is predicted by the SM as a direct consequence of mass generation via spontaneous electroweak symmetry breaking (ESB), has so far eluded direct observation. Moreover, the many shortcomings of the SM suggest that it may indeed be a low-energy limit of a more fundamental theory. One of the most promising candidates for a theory beyond the SM is Supersymmetry (SUSY) (for a review see, e.g., Refs. [4, 5, 6, 7, 8]). Supersymmetry solves the finetuning problem, allows for gauge coupling unification, provides a dark matter candidate, predicts a light Higgs boson and agrees with precision electroweak measurements. However, no direct experimental evidence of SUSY has been found yet.

The large mass of the top quark suggests that it plays a special role in the mechanism of ESB, and that new physics connected to ESB may be found first through precision studies of top-quark observables. Deviations of experimental measurements from the SM predictions, including electroweak and QCD corrections, could indicate new non-standard top production or decay mechanisms. If supersymmetric particles are detected at the LHC, the comparison of precisely measured top-quark observables with their predictions including SUSY loop effects may yield additional information about the underlying model, that may not be accessible otherwise. Measuring precisely the properties of the top quark therefore is an important goal at the Tevatron Run II and the LHC. To fully exploit the potential of these colliders for precision top-quark physics, it is crucial that predictions for top-quark observables include higher-order corrections within the SM and beyond. In this paper we study the impact of SUSY QCD (SQCD) one-loop corrections within the Minimal Supersymmetric SM (MSSM) on strong top-pair production at both the Tevatron Run II and the LHC.

Presently, the total top-pair production cross section has been measured at the Tevatron¹ with a relative uncertainty of $\Delta\sigma_{t\bar{t}}/\sigma_{t\bar{t}} = 12\%$ (with $\mathcal{L} = 760 \text{ pb}^{-1}$) [9] and is in good agreement with the theoretical QCD prediction [10, 11]. It is anticipated that at the Tevatron Run II the top-pair production cross section will be measured with a relative uncertainty of $\Delta\sigma_{t\bar{t}}/\sigma_{t\bar{t}} \approx 10\%$ (with $\mathcal{L} = 2 \text{ fb}^{-1}$). At the LHC, the goal is to measure $\sigma_{t\bar{t}}$ ultimately with a relative uncertainty of $< 5\%$. The current experimental uncertainty still leaves room for SUSY loop effects. Through the virtual presence of supersymmetric particles in quantum corrections, the measurement of the cross section, kinematic distributions and the extraction of masses and couplings may be affected. Among the top-quark observables under study, parity-violating asymmetries in the production of left and right-handed top quarks are of special interest. They have the potential to provide a clean signal of non-SM physics: QCD preserves parity and the SM induced asymmetries are too small to be observable, at least at the Tevatron $p\bar{p}$ collider [12, 13]. The produced top quarks decay almost entirely into a bottom quark and a W boson before they can hadronize [14] or flip their spins. The spin correlation of the top-pair system will therefore be preserved and can be measured by studying angular distributions of the decay products [15]. In order to determine the sensitivity of top-quark observables to SUSY loop effects, it is necessary to calculate the radiative corrections to the top production and decay processes, both within the SM and its supersymmetric extension, and to implement these calculations in a Monte Carlo program. The latter will allow an efficient determination of those observables that are most sensitive to supersymmetric particles, after taking into account the detector response.

In this paper, we present the calculation of the complete SQCD $\mathcal{O}(\alpha_s)$ corrections to the main production channels of strong top-pair production at the Tevatron and LHC, $q\bar{q} \rightarrow t\bar{t}$ ($q\bar{q}$ annihilation) and $gg \rightarrow t\bar{t}$ (gluon fusion), and present a detailed study of their numerical impact on top-quark observables in both unpolarized and polarized $t\bar{t}$ production (the initial-state quarks and gluons are unpolarized). We consider the MSSM with CP-conserving couplings. The inclusion of the top-quark decays and implementation in a Monte Carlo program for off-shell $t\bar{t}$ production is work in progress [16], but beyond the scope of this paper.

¹ See www-cdf.fnal.gov and www-d0.fnal.gov for most recent results from the CDF and D0 collaborations, respectively.

The SM predictions to both polarized and unpolarized $t\bar{t}$ production at hadron colliders are under good theoretical control: The Born-level amplitudes to $q\bar{q}$ annihilation and gluon fusion were first considered in Refs. [17, 18, 19, 20, 21, 22]. At next-to-leading order (NLO), the SM QCD corrections for the total cross section and spin-independent kinematic distributions have been presented in Refs. [23, 24, 25, 26, 27, 28], electroweak corrections have been studied in Refs. [29, 30, 31, 32, 33, 34, 35] and soft gluon resummation and threshold effects in Refs. [10, 36, 37, 38, 39]. To measure spin correlations and asymmetries at the Tevatron and LHC, higher-order corrections to polarized $t\bar{t}$ production need to be known as well: The NLO QCD and electroweak corrections for the polarized production have been calculated in Refs. [40, 41, 42, 43] and Refs. [12, 13, 30, 32, 44], respectively.

A number of studies of higher-order corrections within the MSSM are also available: The SUSY electroweak one-loop corrections to unpolarized on-shell $t\bar{t}$ production at hadron colliders have been calculated in Refs. [45, 46, 47] ($q\bar{q}$ annihilation) and Ref. [47] (gluon fusion), and the same set of corrections for polarized top-pair production has been considered in Ref. [12]. A study of leading logarithmic SUSY electroweak corrections can be found in Ref. [48] and of Yukawa corrections in a two-Higgs-doublet model is given in Ref. [49]. The NLO SQCD corrections to the $gg \rightarrow t\bar{t}$ subprocess without polarization have been presented in Refs. [50, 51] and in Ref. [51] for the scattering of polarized protons. The unpolarized $q\bar{q}$ annihilation subprocess has been investigated at NLO SQCD by a number of groups: In Ref. [46] the corrections with the assumption of negligible box contributions have been calculated, whereas in Refs. [52, 53] the gluon self-energy and crossed box diagram contributions have been neglected. The full NLO SQCD corrections to $q\bar{q} \rightarrow t\bar{t}$ have been examined in Refs. [54, 55, 56]. However, the results of these different calculations do not agree. The origin of this disagreement has been found (see footnote in Ref. [56]), and is due to a difference in the signs of the direct and crossed box diagrams (see Fig. 4), leading to large numerical differences that are especially pronounced in case of comparable small top squark and gluino masses. However, a reliable, complete and detailed study of the impact of NLO SQCD corrections on $t\bar{t}$ production based on the correct result is not available in the literature.

This paper represents the first detailed study of the numerical impact of NLO SQCD corrections on both polarized and unpolarized strong $t\bar{t}$ production at hadron colliders, that considers both main production channels, $q\bar{q}$ annihilation and gluon fusion. We present nu-

merical results for the total production cross section, the invariant $t\bar{t}$ mass and top transverse momentum distributions, and polarization asymmetries, at both the Tevatron Run II and the LHC, respecting current experimental bounds on the masses of the supersymmetric particles. We provide analytic expressions for the complete NLO SQCD corrections to polarized $t\bar{t}$ production and compare our results with the literature where available. Our results have been thoroughly cross-checked by performing at least two independent calculations, based on analytic methods and the FeynArts [57, 58] and FormCalc [59, 60] packages.

The paper is structured as follows: In Section II we present the analytic results for the partonic $q\bar{q}, gg \rightarrow t\bar{t}$ scattering processes, specify our renormalization procedure and our convention of the squark mixing parameters and choice of MSSM input parameters. Section III contains a detailed study of the numerical impact of the NLO SQCD corrections on polarized and unpolarized top-pair production at the Tevatron RUN II and LHC. We first discuss their impact in detail at parton level and then present their most pronounced effects to the observable, hadronic cross sections, followed by a discussion of their prospects to be observable at these colliders. We also include a comparison with available results in the literature. Finally, a summary of our results and conclusion can be found in Section IV. Details of the calculation and explicit analytic expressions are provided in the appendices. We also made available a Fortran code ² that calculates the cross sections presented in this paper to polarized and unpolarized top-pair production at hadron colliders at leading-order (LO) QCD and NLO SQCD.

II. STRONG TOP-PAIR PRODUCTION AT NLO SQCD

At the Tevatron the main production mechanism for the strong production of top-quark pairs is the annihilation of a quark-antiquark pair

$$q(p_4) + \bar{q}(p_3) \rightarrow t(p_2, \lambda_t) + \bar{t}(p_1, \lambda_{\bar{t}}) ,$$

whereas at the LHC the top-quark pairs are mainly produced via the fusion of two gluons

$$g(p_4) + g(p_3) \rightarrow t(p_2, \lambda_t) + \bar{t}(p_1, \lambda_{\bar{t}}) ,$$

² The Fortran code is provided at <http://ubpheno.physics.buffalo.edu/~dow/ppttsqcd>.

where $p_i, i = 1, \dots, 4$ are the four-momenta of the in- and outgoing particles and $\lambda_t(\lambda_{\bar{t}}) = \pm 1/2$ denotes the top(antitop) helicity state. The corresponding Feynman diagrams at LO QCD are shown in Figs. 1, 2. The partonic differential cross sections to the $q\bar{q}$ annihilation and gluon fusion processes for polarized top-quark pairs at NLO SQCD can be written as

$$\begin{aligned} d\hat{\sigma}_{q\bar{q},gg}^{NLO}(\hat{t}, \hat{s}, \lambda_t, \lambda_{\bar{t}}) &= d\hat{\sigma}_{q\bar{q},gg}^{LO}(\hat{t}, \hat{s}, \lambda_t, \lambda_{\bar{t}}) + \delta d\hat{\sigma}_{q\bar{q},gg}(\hat{t}, \hat{s}, \lambda_t, \lambda_{\bar{t}}) \\ &= \frac{d\Phi_{2 \rightarrow 2}}{8\pi^2 \hat{s}} \left[\overline{\sum} |\mathcal{M}_B^{q\bar{q},gg}|^2 + 2\mathcal{R}e \overline{\sum} (\delta \mathcal{M}_{q\bar{q},gg}^{SQCD} \times \mathcal{M}_B^{q\bar{q},gg*}) \right], \end{aligned} \quad (1)$$

where $\hat{s} = (p_1 + p_2)^2 = (p_3 + p_4)^2, \hat{t} = (p_3 - p_1)^2 = (p_4 - p_2)^2 = m_t^2 - \hat{s}(1 - \beta_t \cos \hat{\theta})/2$ are Mandelstam variables with $\hat{\theta}$ denoting the scattering angle in the parton center-of-mass system (CMS) and $\beta_t = \sqrt{1 - 4m_t^2/\hat{s}}$ is the top-quark velocity. The matrix elements squared are averaged over initial-state spin and color degrees of freedom and summed over final-state color degrees of freedom. The phase space of the $2 \rightarrow 2$ scattering process, $d\Phi_{2 \rightarrow 2}$, as usual reads

$$\int d\Phi_{2 \rightarrow 2} = \int \frac{d^3 \mathbf{p}_1}{2p_1^0} \frac{d^3 \mathbf{p}_2}{2p_2^0} \delta^{(4)}(p_3 + p_4 - p_1 - p_2) = \frac{\beta_t}{8} \int_0^{2\pi} d\phi^* \int_{-1}^1 d \cos \hat{\theta}, \quad (2)$$

where the phase space has been evaluated in the parton CMS with ϕ^* denoting the azimuthal angle. The matrix elements, $\mathcal{M}_B^{q\bar{q},gg}$ and $\delta \mathcal{M}_{q\bar{q},gg}^{SQCD}$, describe respectively the LO QCD and one-loop SQCD contributions to $q\bar{q}$ annihilation and gluon fusion. The explicit expressions for $\mathcal{M}_B^{q\bar{q},gg}$ and the spin and color averaged transition amplitude squared, $\overline{\sum} |\mathcal{M}_B^{q\bar{q},gg}|^2$, can be found in Ref. [29] (Sec. 2.1 and 2.2) for unpolarized and in [12] (Appendix A) for polarized top-pair production.

The observable hadronic differential cross sections are obtained by convoluting the partonic cross sections of Eq. (1) with parton distribution functions (PDFs)

$$\begin{aligned} d\sigma_{LO,NLO}(S, \lambda_t, \lambda_{\bar{t}}) &= \sum_{ij=q\bar{q},gg} \frac{1}{1 + \delta_{ij}} \int_0^1 dx_1 dx_2 \\ &\times \left[f_i(x_1, \mu_F) f_j(x_2, \mu_F) d\hat{\sigma}_{ij}^{LO,NLO}(\alpha_s(\mu_R), \hat{s}, \hat{t}, \lambda_t, \lambda_{\bar{t}}) + i \leftrightarrow j \right] \end{aligned} \quad (3)$$

with $S = \hat{s}/(x_1 x_2)$. In the numerical evaluation, we use the CTEQ6L1 (LO) set of parton distribution functions [61] with the QCD factorization (μ_F) and renormalization scale (μ_R) chosen to be $\mu_F = \mu_R = m_t$. Accordingly, the cross section is evaluated using the one-loop evolution of the strong coupling constant with $n_f = 5$ light flavors, $\Lambda_{QCD}^5 = 0.165$ GeV and $\alpha_s^{LO}(M_Z) = 0.130$, which yields $\alpha_s^{LO}(m_t) = 0.1176$.

In the remaining parts of this section we will present the explicit expressions for the partonic NLO SQCD differential cross sections, $d\hat{\sigma}_{q\bar{q}}^{NLO}$ and $d\hat{\sigma}_{gg}^{NLO}$, to polarized top-quark pair production. The corresponding cross sections for unpolarized $t\bar{t}$ production can be obtained by summing over the top and antitop-quark helicity states, $\sum_{\lambda_t, \lambda_{\bar{t}}=\pm 1/2} d\hat{\sigma}_{q\bar{q}, gg}^{LO, NLO}(\lambda_t, \lambda_{\bar{t}})$.

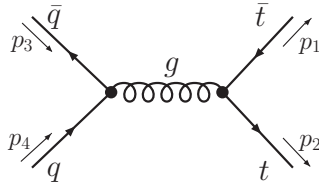


Figure 1: *Feynman diagram to the $q\bar{q} \rightarrow t\bar{t}$ subprocess at LO QCD.*

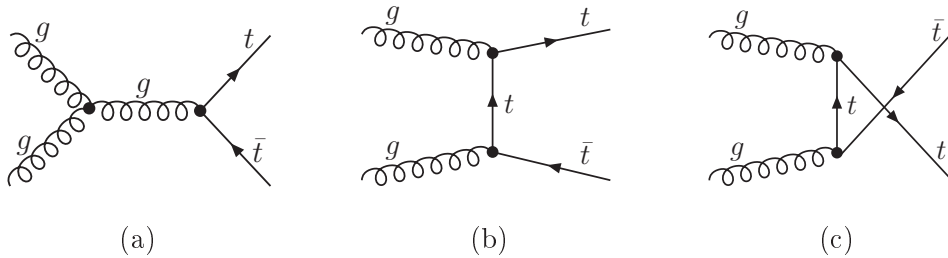


Figure 2: *Feynman diagrams to the s (diagram (a)), t (diagram (b)) and u (diagram (c)) channels of the $gg \rightarrow t\bar{t}$ subprocess at LO QCD.*

A. NLO SQCD corrections to $q\bar{q}$ annihilation and gluon fusion

The SQCD $\mathcal{O}(\alpha_s)$ corrections modify the tree-level $gt\bar{t}$, ggg and $gq\bar{q}$ vertices and the gluon propagator through the virtual presence of gluinos (\tilde{g}), squarks ($\tilde{q}_{L,R}$), stops ($\tilde{t}_{L,R}$) and sbottoms ($\tilde{b}_{L,R}$), i.e. the superpartners of the gluon, the left and right-handed light quarks, top and bottom quarks, respectively, as shown in Figs. 3-6. For completeness, we also provide the corresponding Feynman rules in Appendix A.

We closely follow Refs. [12, 29] and write the NLO SQCD matrix elements, $\delta M_{q\bar{q}, gg}^{SQCD}$, of Eq. (1) in terms of form factors that describe the SQCD one-loop corrections. In case of gluon fusion, these form factors multiply so-called standard matrix elements (SMEs) that contain the information about the Dirac matrix structure. After the interference with the Born matrix elements, the SMEs are written in terms of scalar products involving the external four-momenta and the top/antitop spin four-vectors, $s_{t, \bar{t}}^\mu$. The latter are defined after choosing the axes along which the t and \bar{t} spins are decomposed, as described in

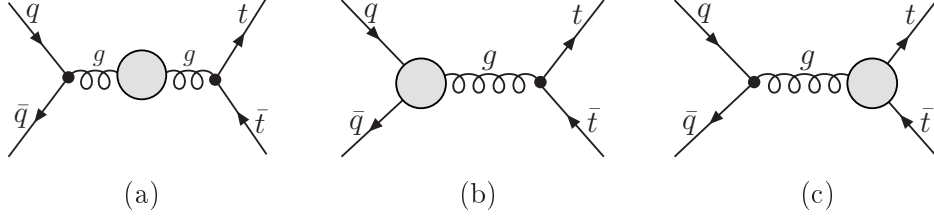


Figure 3: *Generic self-energy (diagram (a)) and vertex (diagrams (b) and (c)) corrections to $q\bar{q} \rightarrow t\bar{t}$ at NLO SQCD. The corrections to the gluon propagator and the $gq\bar{q}$ vertex are explicitly shown in Figs. 7 and 27, respectively.*

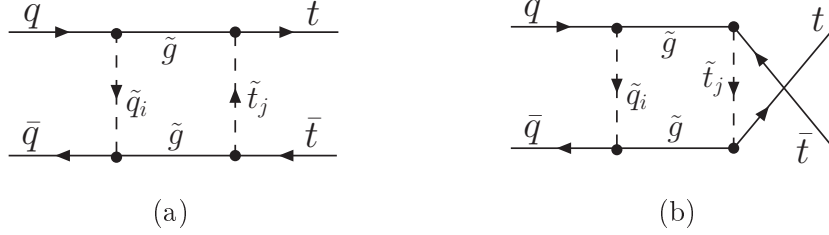


Figure 4: (a) *Direct box diagram and (b) crossed box diagram contributing to $q\bar{q} \rightarrow t\bar{t}$ at NLO SQCD. Graphs containing squarks/stops are summed over the squark/stop mass eigenstates $i,j=L,R$ (no mixing), $i,j=1,2$ (with mixing).*

Appendix A of Ref. [12]. As studied in Ref. [43], for instance, the freedom in the choice of the spin axes can be used to increase spin correlations at hadron colliders. Here we choose the helicity basis where the spin is quantized along the particle's direction of motion. Using the helicity basis, the NLO SQCD contribution to the polarized partonic cross sections of Eq. (1) read as follows (with $z = \cos \hat{\theta}$):

$q\bar{q}$ annihilation:

$$\begin{aligned}
2\mathcal{R}e \sum \overline{(\delta\mathcal{M}_{q\bar{q}}^{SQCD} \times \mathcal{M}_B^{q\bar{q}*})} = \\
\sum \overline{|\mathcal{M}_B^{q\bar{q}}|^2} \frac{\alpha_s}{2\pi} \mathcal{R}e \left(F_V(\hat{s}, m_q = 0) + F_V(\hat{s}, m_t) - \hat{\Pi}(\hat{s}) \right) + \\
\frac{4\pi\alpha_s^3}{9} \mathcal{R}e \left(\beta_t^2(1-z^2)(1+4\lambda_t\lambda_{\bar{t}})F_M(\hat{s}, m_t) - 2(\lambda_t - \lambda_{\bar{t}}) [2zG_A(\hat{s}, m_q = 0) + \right. \\
\left. \beta_t(1+z^2)G_A(\hat{s}, m_t)] \right) + \frac{32\pi\alpha_s^3}{9\hat{s}} \mathcal{R}e \left((-1)\frac{7}{3}B_t - \frac{2}{3}B_u \right) (\hat{s}, \hat{t}, \lambda_t, \lambda_{\bar{t}}), \quad (4)
\end{aligned}$$

where the $gt\bar{t}$ and $gq\bar{q}$ vertex and the gluon self-energy corrections shown in Fig. 3 are parametrized respectively in terms of UV finite (after renormalization) form factors F_V , F_M , G_A , and the subtracted gluon vacuum polarization $\hat{\Pi}(\hat{s}) \equiv \Pi(\hat{s}) - \Pi(0)$. F_V , F_M , and G_A denote the vector, magnetic and axial vector parts of the vertex correction. The direct

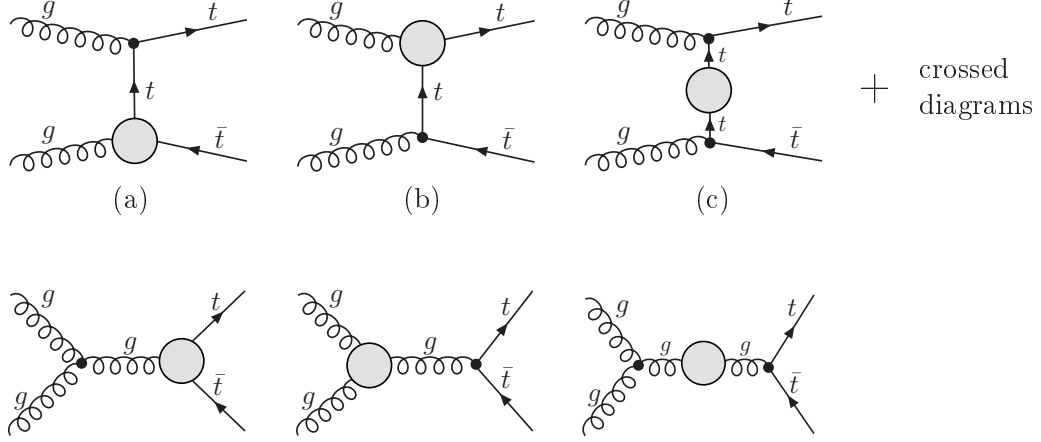


Figure 5: *Generic vertex and self-energy corrections to the $t(u)$ channel (diagrams (a)-(c)) and the s channel (lower row) of the $gg \rightarrow t\bar{t}$ subprocess at NLO SQCD. The corrections to the $gt\bar{t}$ vertex, the quark and gluon propagators, and the ggg vertex are explicitly shown in Figs. 27, 8, 7, and 29, respectively.*

and crossed box contributions to $q\bar{q}$ annihilation shown in Fig. 4 are described by B_t and B_u , respectively. Explicit expressions for these form factors and the box contributions are provided in Appendix B and $\hat{\Pi}(\hat{s})$ is given in Eq. (12).

gluon fusion:

$$\begin{aligned}
2\mathcal{R}e \overline{\sum} (\delta\mathcal{M}_{gg}^{SQCD} \times \mathcal{M}_B^{gg*}) = & \\
& \frac{4\pi\alpha_s^3}{64} 2\mathcal{R}e \left\{ \sum_{j=1,2,3} \left(c^s(j) \frac{1}{\hat{s}} \left[M_{\lambda_t\lambda_{\bar{t}}}^{V,t}(2,j) \left(F_V(\hat{s}, m_t) - \hat{\Pi}(\hat{s}) + \rho_2^{V,s}(\hat{s}) \right) \right. \right. \right. \\
& + \left. \left. M_{\lambda_t\lambda_{\bar{t}}}^{V,t}(12,j) \frac{(\hat{t} - \hat{u})}{2m_t^2} F_M(\hat{s}, m_t) + M_{\lambda_t\lambda_{\bar{t}}}^{A,t}(2,j) G_A(\hat{s}, m_t) \right] \right. \\
& + \left. c^t(j) \sum_{\substack{i=1,\dots,7 \\ 11,\dots,17}} \left[M_{\lambda_t\lambda_{\bar{t}}}^{V,t}(i,j) \left(\frac{\rho_i^{V,t}(\hat{t}, \hat{s})}{\hat{t} - m_t^2} + \frac{\rho_i^{\Sigma,t}(\hat{t}, \hat{s})}{(\hat{t} - m_t^2)^2} \right) + M_{\lambda_t\lambda_{\bar{t}}}^{A,t}(i,j) \left(\frac{\sigma_i^{V,t}(\hat{t}, \hat{s})}{\hat{t} - m_t^2} + \frac{\sigma_i^{\Sigma,t}(\hat{t}, \hat{s})}{(\hat{t} - m_t^2)^2} \right) \right] \\
& + \left. c^u(j) \sum_i \left[M_{\lambda_t\lambda_{\bar{t}}}^{V,u}(i,j) \left(\frac{\rho_i^{V,u}(\hat{u}, \hat{s})}{\hat{u} - m_t^2} + \frac{\rho_i^{\Sigma,u}(\hat{u}, \hat{s})}{(\hat{u} - m_t^2)^2} \right) + M_{\lambda_t\lambda_{\bar{t}}}^{A,u}(i,j) \left(\frac{\sigma_i^{V,u}(\hat{u}, \hat{s})}{\hat{u} - m_t^2} + \frac{\sigma_i^{\Sigma,u}(\hat{u}, \hat{s})}{(\hat{u} - m_t^2)^2} \right) \right] \\
& + \frac{1}{2} \sum_{d=a,b,c} c_d^t(j) \sum_i \left[M_{\lambda_t\lambda_{\bar{t}}}^{V,t}(i,j) \rho_{i,d}^{\square,t}(\hat{t}, \hat{s}) + M_{\lambda_t\lambda_{\bar{t}}}^{A,t}(i,j) \sigma_{i,d}^{\square,t}(\hat{t}, \hat{s}) \right] \\
& + \frac{1}{2} \sum_{d=a,b} c_d^u(j) \sum_i \left[M_{\lambda_t\lambda_{\bar{t}}}^{V,u}(i,j) \rho_{i,d}^{\square,u}(\hat{u}, \hat{s}) + M_{\lambda_t\lambda_{\bar{t}}}^{A,u}(i,j) \sigma_{i,d}^{\square,u}(\hat{u}, \hat{s}) \right] \Big) \\
& + \frac{11}{18} \left[M_{\lambda_t\lambda_{\bar{t}}}^{V,t}(12,2) + M_{\lambda_t\lambda_{\bar{t}}}^{V,t}(12,3) \right] \rho_{12}^{\square,gg\bar{t}\bar{t}}(\hat{s}) \Big\} , \tag{5}
\end{aligned}$$

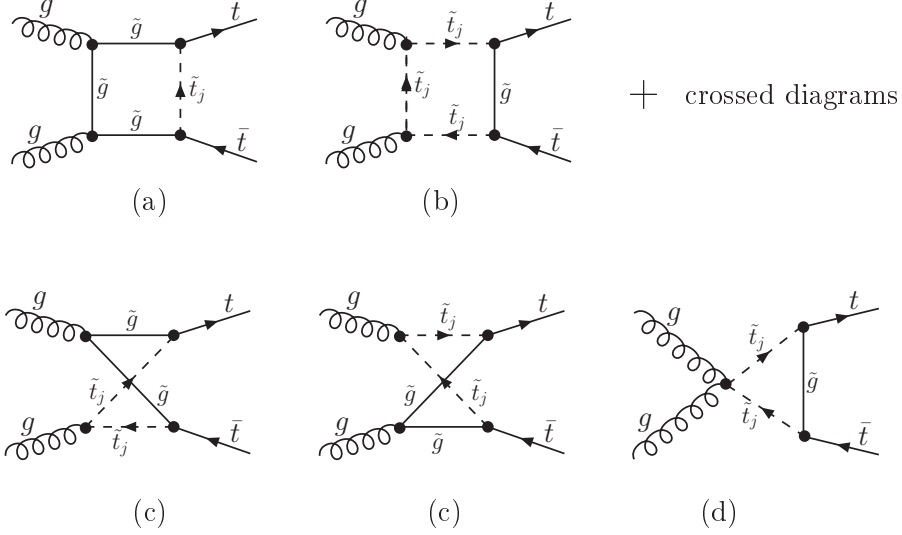


Figure 6: *Box corrections to $gg \rightarrow t\bar{t}$ at NLO SQCD. The box diagrams $d = a, b$ contribute to both the t and u (crossed) channels, whereas the box diagrams $d = c$ and the box-triangle correction (diagram (d)) involving a quartic $gg\tilde{t}\tilde{t}$ interaction only contribute to the t channel. Graphs containing stops are summed over the stop mass eigenstates $j=L,R$ (no mixing), $j=1,2$ (with mixing)*

where i numerates the 14 SMEs, $M_i^{(V,A),(t,u)}$ of Eqs. (B1), (B2) in Ref. [29], and $j = 1, 2, 3$ the s, t, u channel of the Born matrix element to the gluon-fusion subprocess. For convenience, the color factors $c^{s,t,u}(j)$ of Ref. [29] and $c_d^{t,u}(j)$ are both provided in Appendix C 3. The coefficients to the SMEs describe the parity conserving ($\rho_i^{(V,\Sigma),(t,u)}$, $\rho_{i,d}^{\square,(t,u)}$, $\rho_{12}^{\square,gg\tilde{t}\tilde{t}}$) and parity violating ($\sigma_i^{(V,\Sigma),(t,u)}$, $\sigma_{i,d}^{\square,(t,u)}$) parts of the SQCD one-loop corrections to the t and u channels of the gluon-fusion subprocess, which consist of

- vertex corrections that modify the $g\tilde{t}\bar{t}$ vertex ($\rho_i^{V,(t,u)}$, $\sigma_i^{V,(t,u)}$), shown in Fig. 5 (diagrams (a) and (b)),
- top-quark self-energy corrections that modify the top-quark propagator ($\rho_i^{\Sigma,(t,u)}$, $\sigma_i^{\Sigma,(t,u)}$), shown in Fig. 5 (diagram (c)),
- box contributions ($\rho_{i,d}^{\square,(t,u)}$, $\sigma_{i,d}^{\square,(t,u)}$), shown in Fig. 6 (diagrams (a), (b) and (c)), and
- the box-triangle correction ($\rho_{12}^{\square,gg\tilde{t}\tilde{t}}$), shown in Fig. 6 (diagram (d)).

The SQCD one-loop corrections to the s channel of the $gg \rightarrow t\bar{t}$ subprocess, shown in Fig. 5 (lower row), are parametrized in terms of the $g\tilde{t}\bar{t}$ vertex form factors (F_V, F_M, G_A),

the coefficient describing the ggg vertex corrections ($\rho_2^{V,s}$), and the subtracted gluon self-energy ($\hat{\Pi}(\hat{s})$). All coefficients to the SMEs are UV finite after applying the renormalization procedure. Their explicit expressions are provided in Appendix C. The expressions for the SMEs after the interference with the Born matrix element, $M_{\lambda_t \lambda_{\bar{t}}}^{(V,A),(t,u)}(i,j)$, can be found in Appendix C of Ref. [12].

Before we turn to the discussion of the numerical impact of these higher-order SQCD corrections on $t\bar{t}$ cross sections, we describe in detail in the following sections our choice of the renormalization scheme and the MSSM input parameters.

B. Renormalization scheme

The complete set of SQCD one-loop corrections to $q\bar{q}$ annihilation and gluon fusion is gauge invariant and IR finite. However, the self-energy and vertex corrections shown in Figs. 8,29 exhibit UV divergences that arise in form of $\Delta = 2/\epsilon - \gamma_E + \log(4\pi)$ terms when using dimensional regularization in $d = 4 - \epsilon$ dimensions. These singularities are removed by introducing a suitable set of counterterms that are fixed by a set of renormalization conditions. We employ multiplicative renormalization and perform the following replacements of the left and right-handed quark fields, $\Psi_{L,R} = \frac{1}{2}(1 \mp \gamma_5) \Psi$, the top-quark mass, m_t , the gluon field, G_μ^a , and the strong coupling constant, g_s , in the QCD Lagrangian:

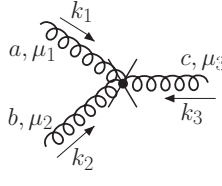
$$\Psi_{L,R} \rightarrow \sqrt{Z_{L,R}} \Psi_{L,R} \quad , \quad m_t \rightarrow m_t - \delta m_t \quad , \quad G_\mu^a \rightarrow \sqrt{Z_3} G_\mu^a \quad , \quad g_s \rightarrow Z_g g_s \quad ,$$

With $Z_i = 1 + \delta Z_i$, this yields the counterterms to the quark and gluon self-energies, $q\bar{q}g$ and ggg vertices as follows (with $\delta_{qt} = 0$ for $q \neq t$ and i, j, a, b, c denoting respectively color degrees of freedom of quarks and gluons):

$$\begin{array}{c} p \\ \rightarrow \\ q_j \end{array} \begin{array}{c} \diagup \\ \times \\ \diagdown \end{array} \begin{array}{c} \rightarrow \\ q_i \end{array} \quad : \quad i\delta_{ij}[\not{p}(\delta Z_V - \delta Z_A \gamma_5) - \delta_{qt}(m_q \delta Z_V - \delta m_q)] \quad (6)$$

$$\begin{array}{c} \text{oooo} \\ a, \mu \end{array} \begin{array}{c} \diagup \\ \times \\ \diagdown \end{array} \begin{array}{c} \rightarrow \\ q_i \end{array} \begin{array}{c} \rightarrow \\ q_j \end{array} \quad : \quad -ig_s T_{ij}^a \gamma_\mu (\delta Z_V + \delta Z_g + \frac{1}{2} \delta Z_3 - \delta Z_A \gamma_5) \quad (7)$$

$$\begin{array}{c} k \\ \rightarrow \\ \text{oooo} \\ a, \mu \end{array} \begin{array}{c} \diagup \\ \times \\ \diagdown \end{array} \begin{array}{c} \text{oooo} \\ b, \nu \end{array} \quad : \quad i\delta_{ab}(k_\mu k_\nu - k^2 g_{\mu\nu}) \delta Z_3 \quad (8)$$



$$: -g_s f_{abc} [(k_1 - k_2)_{\mu_3} g_{\mu_1 \mu_2} + (k_2 - k_3)_{\mu_1} g_{\mu_2 \mu_3} + (k_3 - k_1)_{\mu_2} g_{\mu_3 \mu_1}] \delta Z_1 \quad (9)$$

with $\delta Z_1 = \delta Z_g + 3\delta Z_3/2$ and $\delta Z_{V,A} = (\delta Z_L \pm \delta Z_R)/2$. For the renormalization of the strong coupling constant and the gluon field, we use the \overline{MS} scheme, modified to decouple the heavy SUSY particles [62, 63], i.e. divergences associated with the squark and gluino loops are subtracted at zero momentum:

- $\delta Z_3 = -\frac{\partial \Sigma_T(k^2)}{\partial k^2} \Big|_{\epsilon, \text{modified}} \equiv -\Pi(0)$, (10)

where $\Sigma_T|_{\epsilon, \text{modified}}$ denotes the terms proportional to $\Delta_m = \Delta - \ln(m^2/\mu_R^2)$ (with $m = m_{\bar{q}}, m_{\bar{g}}$) of the transverse part of the gluon self-energy, yielding

$$\Pi(0) = \frac{\alpha_s}{4\pi} \left\{ \frac{1}{6} \sum_{\substack{q=u,c,t \\ d,s,b}} \sum_j \Delta_{m_{\bar{q}_j}} + 2\Delta_{m_{\bar{g}}} \right\} . \quad (11)$$

Only the transverse part of the gluon self-energy contributes to the NLO SQCD cross section for $t\bar{t}$ production and the SQCD one-loop contribution to the renormalized gluon self-energy shown in Fig. 7 enters the partonic differential cross sections of Eqs. (4), (5) as follows:

$$\begin{aligned} \frac{\alpha_s}{4\pi} \hat{\Pi}(k^2) &= \frac{\Sigma_T(k^2)}{k^2} + \delta Z_3 \\ &= \frac{\alpha_s}{4\pi} \left\{ \sum_{\substack{q=u,c,t \\ d,s,b}} \sum_j \frac{1}{6} \left[\frac{(k^2 - 4m_{\bar{q}}^2)}{k^2} B_0(k^2, m_{\bar{q}}, m_{\bar{q}}) + \frac{4m_{\bar{q}}^2}{k^2} B_0(0, m_{\bar{q}_j}, m_{\bar{q}_j}) + \frac{2}{3} \right] \right. \\ &\quad \left. - \frac{2}{3} + 2 \frac{(2m_{\bar{g}}^2 + k^2)}{k^2} B_0(k^2, m_{\bar{g}}, m_{\bar{g}}) - \frac{4m_{\bar{g}}^2}{k^2} B_0(0, m_{\bar{g}}, m_{\bar{g}}) \right\} - \Pi(0) . \quad (12) \end{aligned}$$

where $j = L, R(1, 2)$ (no(with) mixing) sums over the two squark mass eigenstates and B_0 denotes the scalar two-point function (see, e.g., Ref. [64]).

- $\delta Z_1 = -\Gamma|_{\epsilon, \text{modified}} \equiv -\Pi(0)$, (13)

where $\Gamma|_{\epsilon, \text{modified}}$ denotes the term proportional to Δ_m (with $m = m_{\bar{q}}, m_{\bar{g}}$) of the one-loop ggg vertex correction shown in Fig. 29 that multiplies the tree level ggg vertex.

Using Eqs. (10),(13), one can verify that $\delta Z_1 = \delta Z_3$ and, thus, $\delta Z_g = -\delta Z_3/2$. It is interesting to note that in this modified version of the \overline{MS} scheme the counter term for the $q\bar{q}g$ vertex coincides with the one of Ref. [29]. Moreover, there is no contribution from self-energy insertions into external gluon legs.

To fix the renormalization constants for the external quarks, $\delta Z_{V,A}(m_q)$, and the top-quark mass renormalization constant, δm_t , we closely follow Ref. [29] and use *on-shell* renormalization conditions. The renormalization constants $\delta Z_{V,A}(m_q), \delta m_t$ are determined by the vector, axialvector and scalar parts of the quark self-energy, evaluated at the on-shell quark mass, $\Sigma_{V,A,S}(p^2 = m_t^2)$ for the top quark and $\Sigma_{V,A}(p^2 = m_q^2 = 0)$ for the incoming quarks in $q\bar{q}$ annihilation. The SQCD one-loop corrections modify these quark self-energy contributions as shown in Fig. 8 as follows:

$$\begin{aligned}\Sigma_V(p^2) &= -\frac{\alpha_s}{4\pi} \sum_j \lambda_j^+ \frac{2}{3} B_1(p^2, m_{\tilde{g}}, m_{\tilde{q}_j}) \\ \Sigma_S(p^2) &= \frac{\alpha_s}{4\pi} \sum_j \lambda_j^- \frac{2}{3} \frac{m_{\tilde{g}}}{m_q} B_0(p^2, m_{\tilde{g}}, m_{\tilde{q}_j}) \\ \Sigma_A(p^2) &= \frac{\alpha_s}{4\pi} \sum_j \lambda_j^A \frac{2}{3} B_1(p^2, m_{\tilde{g}}, m_{\tilde{q}_j}),\end{aligned}\tag{14}$$

yielding the following *on-shell* renormalization constants:

$$\begin{aligned}\delta Z_V(m_q) &= -\Sigma_V(p^2 = m_q^2) - 2m_q^2 \frac{\partial}{\partial p^2} (\Sigma_V + \Sigma_S)|_{p^2=m_q^2} \\ &= \frac{\alpha_s}{4\pi} \sum_j \frac{2}{3} [\lambda_j^+ (B_1 + 2m_q^2 B'_1) - 2m_q m_{\tilde{g}} \lambda_j^- B'_0] (m_q^2, m_{\tilde{g}}, m_{\tilde{q}_j})\end{aligned}\tag{15}$$

$$\begin{aligned}\delta Z_A(m_q) &= -\Sigma_A(p^2 = m_q^2) \\ &= -\frac{\alpha_s}{4\pi} \sum_j \lambda_j^A \frac{2}{3} B_1(m_q^2, m_{\tilde{g}}, m_{\tilde{q}_j}) \\ \frac{\delta m_t}{m_t} &= -\Sigma_V(p^2 = m_q^2) - \Sigma_S(p^2 = m_q^2)\end{aligned}\tag{16}$$

$$= -\frac{\alpha_s}{4\pi} \sum_j \frac{2}{3} \left[-\lambda_j^+ B_1 + \lambda_j^- \frac{m_{\tilde{g}}}{m_t} B_0 \right] (m_t^2, m_{\tilde{g}}, m_{\tilde{t}_j}),\tag{17}$$

where $j = L, R(1, 2)$ (no(with) mixing) sums over the two squark mass eigenstates, and the coupling constant factors, $\lambda_j^\pm, \lambda_j^A$, are given in Appendix A. The scalar and vector two-point functions, $B_{0,1}$, and their derivatives, $B'_{0,1}(p^2 = m^2) \equiv \partial B_{0,1}/\partial p^2|_{p^2=m^2}$, can be found in Ref. [64], for instance. In the *on-shell* renormalization scheme, the derivative of the renormalized quark self-energy of Fig. 8 is zero when evaluated at $p^2 = m_q^2$, and thus there

is no contribution from the self-energy insertions in the external quark lines. Finally, it is interesting to note that for our choice of renormalization scheme, the renormalized SQCD one-loop corrections only depend on μ_R through the strong coupling constant, $\alpha_s(\mu_R)$.

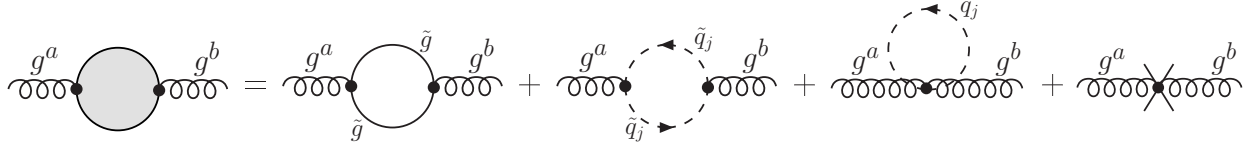


Figure 7: *Renormalized gluon self-energy*, $-i\hat{\Sigma}_{\mu\nu} = i\delta_{ab}(k_\mu k_\nu \hat{\Sigma}_L - g_{\mu\nu} \hat{\Sigma}_T)$, at *NLO SQCD*. Graphs containing squarks are summed over the squark mass eigenstates $j=L,R$ (no mixing), $j=1,2$ (with mixing) and the quark flavors $q=\{u,d,s,c,b,t\}$.

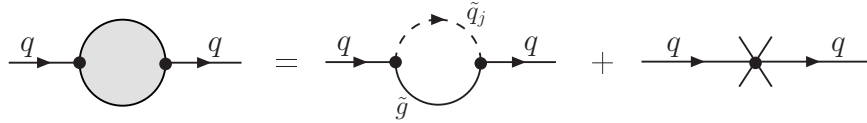


Figure 8: *Renormalized quark self-energy*, $i\hat{\Sigma} = i(\not{p}[\hat{\Sigma}_V - \hat{\Sigma}_A\gamma_5] + m_q\hat{\Sigma}_S)$, at *NLO SQCD*. Graphs containing squarks are summed over the squark mass eigenstates $j=L,R$ (no mixing), $j=1,2$ (with mixing).

C. Scalar quark sector of the MSSM

The superpartners of the left and right-handed top quarks are the left and right-handed scalar top squarks ('stops'), \tilde{t}_L and \tilde{t}_R . Assuming all supersymmetric breaking parameters are real, the part of the MSSM Lagrangian that contains the stop mass terms reads

$$\mathcal{L} = -(\tilde{t}_L^*, \tilde{t}_R^*) \mathcal{M} \begin{pmatrix} \tilde{t}_L \\ \tilde{t}_R \end{pmatrix} \quad \text{with} \quad \mathcal{M} = \begin{pmatrix} m_{\tilde{t}_L}^2 & m_t X_t \\ m_t X_t & m_{\tilde{t}_R}^2 \end{pmatrix}, \quad (18)$$

where the diagonal entries $m_{\tilde{t}_L}^2$ and $m_{\tilde{t}_R}^2$ of the stop mass matrix \mathcal{M} as well as X_t are defined as

$$\begin{aligned} m_{\tilde{t}_L}^2 &= M_{\tilde{t}_L}^2 + m_t^2 + M_Z^2 \cos 2\beta (I_3^t - Q_t s_w^2), & X_t &= (A_t - \mu/\tan\beta), \\ m_{\tilde{t}_R}^2 &= M_{\tilde{t}_R}^2 + m_t^2 + M_Z^2 \cos 2\beta Q_t s_w^2 \end{aligned} \quad (19)$$

with $I_3^t = 1/2$, $Q_t = 2/3$ and $s_w^2 = 1 - M_W^2/M_Z^2$. Furthermore, $\tan\beta = v_2/v_1$ (also v_u/v_d in the literature) denotes the ratio of the two Higgs vacuum expectation values, $A_{\tilde{t}}$ the trilinear Higgs-stop-stop coupling and μ is the Higgs-mixing parameter. $M_{\tilde{t}_L}$ and $M_{\tilde{t}_R}$ are the soft supersymmetry-breaking squark-mass parameters. As can be seen from Eq. (18), \tilde{t}_L and \tilde{t}_R are not necessarily mass eigenstates, since \mathcal{M} is of non-diagonal form. Thus, \tilde{t}_L, \tilde{t}_R can mix, so that the physical mass eigenstates \tilde{t}_1, \tilde{t}_2 are model-dependent linear combinations of these states. The latter are obtained by diagonalizing the mass matrix performing the transformation

$$\begin{pmatrix} \tilde{t}_1 \\ \tilde{t}_2 \end{pmatrix} = \begin{pmatrix} \cos\theta_{\tilde{t}} & \sin\theta_{\tilde{t}} \\ -\sin\theta_{\tilde{t}} & \cos\theta_{\tilde{t}} \end{pmatrix} \begin{pmatrix} \tilde{t}_L \\ \tilde{t}_R \end{pmatrix}. \quad (20)$$

The mass term of the supersymmetric Lagrangian will then transform to the diagonal form

$$\mathcal{L} = -(\tilde{t}_1^*, \tilde{t}_2^*) \begin{pmatrix} m_{\tilde{t}_1}^2 & 0 \\ 0 & m_{\tilde{t}_2}^2 \end{pmatrix} \begin{pmatrix} \tilde{t}_1 \\ \tilde{t}_2 \end{pmatrix}. \quad (21)$$

Inserting Eq. (20) and its adjoint form into Eq. (21) and comparing with Eq. (18) the mass matrix \mathcal{M} can be written as

$$\mathcal{M} = \begin{pmatrix} \cos^2\theta_{\tilde{t}} m_{\tilde{t}_1}^2 + \sin^2\theta_{\tilde{t}} m_{\tilde{t}_2}^2 & \sin\theta_{\tilde{t}} \cos\theta_{\tilde{t}} (m_{\tilde{t}_1}^2 - m_{\tilde{t}_2}^2) \\ \sin\theta_{\tilde{t}} \cos\theta_{\tilde{t}} (m_{\tilde{t}_1}^2 - m_{\tilde{t}_2}^2) & \sin^2\theta_{\tilde{t}} m_{\tilde{t}_1}^2 + \cos^2\theta_{\tilde{t}} m_{\tilde{t}_2}^2 \end{pmatrix}. \quad (22)$$

Comparing the two different descriptions of the mass matrix \mathcal{M} we find

$$\begin{aligned} m_{\tilde{t}_L}^2 &= \cos^2\theta_{\tilde{t}} m_{\tilde{t}_1}^2 + \sin^2\theta_{\tilde{t}} m_{\tilde{t}_2}^2, \\ m_{\tilde{t}_R}^2 &= \sin^2\theta_{\tilde{t}} m_{\tilde{t}_1}^2 + \cos^2\theta_{\tilde{t}} m_{\tilde{t}_2}^2, \\ m_t X_t &= \sin\theta_{\tilde{t}} \cos\theta_{\tilde{t}} (m_{\tilde{t}_1}^2 - m_{\tilde{t}_2}^2). \end{aligned} \quad (23)$$

As input parameters we choose the physical measurable quantities $m_{\tilde{t}_1}, m_{\tilde{t}_2}$ and the stop mixing angle $\theta_{\tilde{t}}$. Studying the properties of Eq. (23) we find that the three equations, and therefore the cross sections of Eq. (1), are invariant under the following two sets of transformations:

$$\theta_{\tilde{t}} \rightarrow \theta_{\tilde{t}} + n \cdot \pi \quad (n \in \mathcal{I}) \quad (24)$$

$$m_{\tilde{t}_1}^2 \leftrightarrow m_{\tilde{t}_2}^2 \quad \text{and} \quad \theta_{\tilde{t}} \rightarrow \theta_{\tilde{t}} + \pi/2. \quad (25)$$

Therefore, for a complete exploration of the size of the SQCD one-loop corrections, it is equivalent to either vary the masses $m_{\tilde{t}_1}^2$ and $m_{\tilde{t}_2}^2$ completely independently and vary the

mixing angle between $\pm\pi/4$, or to choose one of the squark masses to be always the lighter one and vary $\theta_{\tilde{t}}$ between $\pm\pi/2$. We choose the latter option and take $m_{\tilde{t}_2}^2$ always to be the lighter top squark and vary the stop mixing angle in the range $-\pi/2 \leq \theta_{\tilde{t}} \leq \pi/2$.

Taking $m_{\tilde{t}_1}$, $m_{\tilde{t}_2}$ and $\theta_{\tilde{t}}$ as input parameters and using Eq. (23), we can calculate $m_{\tilde{t}_L}^2$, $m_{\tilde{t}_R}^2$ and X_t . The soft supersymmetry-breaking parameters $M_{\tilde{t}_L}$ and $M_{\tilde{t}_R}$ can be determined from Eq. (19) in dependence of $\tan\beta$. Since the SQCD NLO cross sections do not directly depend on $\tan\beta$ and the dependence of $m_{\tilde{t}_L}^2$ and $m_{\tilde{t}_R}^2$ on $\tan\beta$ in the range $1 \leq \tan\beta \leq 50$ is rather weak, we choose in this paper an arbitrary value for $\tan\beta$, i.e. $\tan\beta = 10$.

The equations (18)-(23) can be formulated in a similar way for the other squark flavors, one just has to replace the index “t” by the appropriate squark index, as well as $X_t \rightarrow X_d = (A_d - \mu \tan\beta)$ for the down-type squarks. Since the off-diagonal elements of the squark mass matrices, $m_q X_q$, are proportional to the quark masses m_q , and X_q cannot be arbitrarily large ($X_q < [65]$), mixing can be neglected for the first two generations of squarks and may be only important in the sbottom sector for large values of $\tan\beta$. However, since the influence of the sbottom sector on the hadronic $t\bar{t}$ cross sections is very small, we also neglect mixing for the bottom squarks and in addition assume $m_{\tilde{b}_L} = m_{\tilde{b}_R}$. Because gauge invariance requires $M_{\tilde{t}_L} = M_{\tilde{b}_L}$, it follows that with

$$m_{\tilde{b}_L}^2 = M_{\tilde{t}_L}^2 + m_b^2 + M_Z^2 \cos 2\beta (I_3^b - Q_b s_w^2), \quad (26)$$

$I_3^b = -1/2$ and $Q_b = -1/3$, the bottom squark masses are already fixed by the input parameters of the top squark sector. We further assume universal squark masses for the first two generations of squarks:

$$m_{\tilde{u}_L} = m_{\tilde{u}_R} = m_{\tilde{d}_L} = m_{\tilde{d}_R} = m_{\tilde{c}_L} = m_{\tilde{c}_R} = m_{\tilde{s}_L} = m_{\tilde{s}_R} := m_{\tilde{q}}. \quad (27)$$

To summarize, in this paper we will study the dependence of the NLO SQCD predictions on the following MSSM parameters: $m_{\tilde{g}}$, $m_{\tilde{t}_1}$, $m_{\tilde{t}_2}$, $\theta_{\tilde{t}}$ and $m_{\tilde{q}}$.

III. NUMERICAL RESULTS

In this section, we examine the numerical impact of the SQCD one-loop corrections on the cross sections for unpolarized and polarized top-pair production at the Tevatron Run II ($\sqrt{S} = 1.96$ TeV) and LHC ($\sqrt{S} = 14$ TeV). The details of the calculation are presented

in Section II, and the Feynman rules and explicit analytic expressions are provided in Appendix A and B, C, respectively.

We performed a number of checks of our calculation: The results for both the $q\bar{q}$ annihilation and gluon fusion matrix elements for polarized and unpolarized top-pair production have been derived by at least two independent analytic calculations based on the Feynman rules of Ref. [66]. The numerical evaluation of the tensor integrals was performed with an implementation described in Ref. [29] as well as by using the packages LoopTools [60]/FF [67]. Furthermore, one of the analytic calculations used the package TRACER [68]. The results of the analytic calculations have been compared numerically with the results obtained with the FeynArts [57, 58] and FormCalc [59, 60] packages using the MSSM model file of Ref. [69]. In all cases, we found perfect numerical agreement.

In the computation of the $t\bar{t}$ observables, we use the following values for the SM input parameters [8]:

$$m_t = 175 \text{ GeV}, \quad m_b = 4.7 \text{ GeV}, \quad M_W = 80.425 \text{ GeV}, \quad M_Z = 91.1876 \text{ GeV}. \quad (28)$$

As described in Section II (Eq. (3)), we use CTEQ6L1 PDFs [61] and the strong coupling constant is evaluated at LO QCD with the factorization and renormalization scales chosen to be equal to the top-quark mass. Our choice of MSSM input parameters is described in Section II C. As an additional constraint on the MSSM parameter space, we calculate the SUSY loop corrections to the ρ parameter, $\Delta\rho(m_{\tilde{t}}, m_{\tilde{b}}, \theta_{\tilde{t}})$ (for a review see, e.g., Ref. [70]), and only allow for MSSM input parameters that yield $\Delta\rho \leq 0.0035$ [71]. If not stated otherwise, we choose the masses of the supersymmetric partners of the light quarks to be $m_{\tilde{q}} = 2 \text{ TeV}$. In varying the remaining MSSM input parameters we observe the following experimentally motivated mass limits [72, 73, 74, 75]: $m_{\tilde{g}} \geq 230 \text{ GeV}$ and $m_{\tilde{t}_2} \geq 100 \text{ GeV}$. In the following sections, we study the numerical impact of the SQCD one-loop corrections on the total $t\bar{t}$ production rate, the invariant $t\bar{t}$ mass and top transverse momentum distributions, and on polarization asymmetries. We discuss the case of unpolarized top quarks in Section III A and consider polarized $t\bar{t}$ production in Section III B. Before we present results for the observable hadronic cross sections at the Tevatron Run II and the LHC in Sections III A 3, III B 3, we perform a detailed investigation of the impact of the SQCD one-loop corrections on the parton-level cross sections in Sections III A 1, III B 1 ($q\bar{q}$ annihilation) and Sections III A 2, III B 2 (gluon fusion). Finally, in Section III C, we compare our results

with existing calculations in the literature where available.

A. Unpolarized top-pair production at NLO SQCD

We first consider the produced top quarks to be unpolarized, i.e. the corresponding partonic and hadronic cross sections are obtained from the ones of Eqs. (1),(3) by summing over the top and antitop-quark helicity states, $\sum_{\lambda_t, \lambda_{\bar{t}}=\pm 1/2} d\hat{\sigma}_{q\bar{q},gg}^{LO,NLO}(\hat{t}, \hat{s}, \lambda_t, \lambda_{\bar{t}})$ and $\sum_{\lambda_t, \lambda_{\bar{t}}=\pm 1/2} d\sigma_{LO,NLO}(S, \lambda_t, \lambda_{\bar{t}})$, respectively.

In order to reveal the numerical impact of the SQCD one-loop corrections on observables to unpolarized top-pair production and to study the dependences on the MSSM input parameters, the gluino mass ($m_{\tilde{g}}$), the two top-squark masses ($m_{\tilde{t}_{1,2}}$), and the stop mixing angle ($\theta_{\tilde{t}}$), we introduce relative corrections as follows:

- At the parton level, we use

$$\hat{\Delta}_{q\bar{q},gg}(\hat{s}) = \frac{\hat{\sigma}_{q\bar{q},gg}^{NLO} - \hat{\sigma}_{q\bar{q},gg}^{LO}}{\hat{\sigma}_{q\bar{q},gg}^{LO}}, \quad (29)$$

where $\hat{\sigma}_{q\bar{q},gg}^{LO,NLO}(\hat{s})$ denote the total partonic production rates to unpolarized $t\bar{t}$ production via $q\bar{q}$ annihilation and gluon fusion at LO QCD and NLO SQCD, respectively.

- At the hadron level, we compute the total hadronic cross section, the invariant $t\bar{t}$ mass ($M_{t\bar{t}}$) and top transverse momentum (p_T) distributions at the Tevatron Run II and the LHC, and use

$$\begin{aligned} \Delta &= \frac{\sigma_{NLO} - \sigma_{LO}}{\sigma_{LO}}, \\ \Delta(M_{t\bar{t}}) &= \frac{d\sigma_{NLO}/dM_{t\bar{t}} - d\sigma_{LO}/dM_{t\bar{t}}}{d\sigma_{LO}/dM_{t\bar{t}}}, \\ \Delta(p_T) &= \frac{d\sigma_{NLO}/dp_T - d\sigma_{LO}/dp_T}{d\sigma_{LO}/dp_T}, \end{aligned} \quad (30)$$

where $d\sigma_{LO,NLO}$ describe the hadronic cross sections to unpolarized $t\bar{t}$ production at LO QCD and NLO SQCD, respectively. All hadron level results are obtained by including both processes $q\bar{q} \rightarrow t\bar{t}$ and $gg \rightarrow t\bar{t}$.

1. *Effects of NLO SQCD corrections in $q\bar{q}$ annihilation for unpolarized top quarks*

At the Tevatron, top-quark pairs are mainly produced via $q\bar{q}$ annihilation and, thus, some of the characteristics of the corrections discussed here at the parton level will manifest themselves again in the hadron-level results for the Tevatron. In the following we study the impact of the NLO SQCD corrections on the $u\bar{u} \rightarrow t\bar{t}$ subprocess, representatively for all $q\bar{q}$ initiated processes.

Fig. 9(a) illustrates the impact of the (renormalized) gluon self-energy, shown in Fig. 7 (see also Eq. (12)), in dependence of the partonic CMS energy, $\sqrt{\hat{s}}$. The upper plot shows the relative correction $\hat{\Delta}_{q\bar{q}}$ of Eq. (29) due to the squark loops, summed over all quark flavors and with squarks degenerate in mass, and the lower plot the correction due to the gluino loop. The gluino loop correction exhibits a characteristic “dip” at the production threshold of a pair of gluinos, $\sqrt{\hat{s}} = 2m_{\tilde{g}}$, reducing the LO cross section by about -10% . The corrections then increase with $\sqrt{\hat{s}}$ due to a $\ln(\hat{s}/m_{\tilde{g}}^2)$ dependence. A similar behavior is observed in the squark loop correction, which can reduce $\hat{\sigma}_{q\bar{q}}^{LO}$ by up to about -4% , again due to a threshold at $\sqrt{\hat{s}} = 2m_{\tilde{q}}$, and then increases with $\sqrt{\hat{s}}$. Both the gluino and the squark loop corrections do not depend on the squark mixing angles.

Fig. 9(b) shows the influence of the vertex corrections of Fig. 3(b),(c), where in the upper plot it is assumed that $m_{\tilde{t}_1} = m_{\tilde{t}_2}$. The corrections are then independent of the top-squark mixing angle, because the term that is proportional to $\theta_{\tilde{t}}$ cancels in Eq. (23). The corrections show again a characteristic threshold behavior at $\sqrt{\hat{s}} = 2m_{\tilde{g}}$. This threshold is introduced by the vertex correction containing the $\tilde{g}\tilde{g}\tilde{t}_{1,2}$ loop, shown in Fig. 27. This loop correction is the dominant contribution to the vertex corrections because of a large overall color factor of $C_A^2 = 9$, arising due to the $g\tilde{g}\tilde{g}$ coupling. If the top squarks are non-degenerate in mass, as it is the case in the lower plot of Fig. 9(b), the vertex correction depends very strongly on the stop mixing angle. Shown are corrections for $m_{\tilde{t}_1} = 600$ GeV and $m_{\tilde{t}_2} = 100$ GeV for different values of the stop mixing angle. The largest correction occurs always at the gluino-pair threshold, $\sqrt{\hat{s}} = 2m_{\tilde{g}}$, for $\theta_{\tilde{t}} = \pi/4$ and the smallest corrections are obtained for $\theta_{\tilde{t}} = -\pi/4$. For other mixing angles the corrections lie between these two curves. The corrections are furthermore the larger the more pronounced the mass splitting between $m_{\tilde{t}_1}$ and $m_{\tilde{t}_2}$. The amount of allowed mass splitting, however, is restricted by the $\Delta\rho$ parameter.

The size of the box corrections is illustrated in Fig. 10(a) for $m_{\tilde{t}_1} = 600$ GeV and $m_{\tilde{t}_2} = 100$

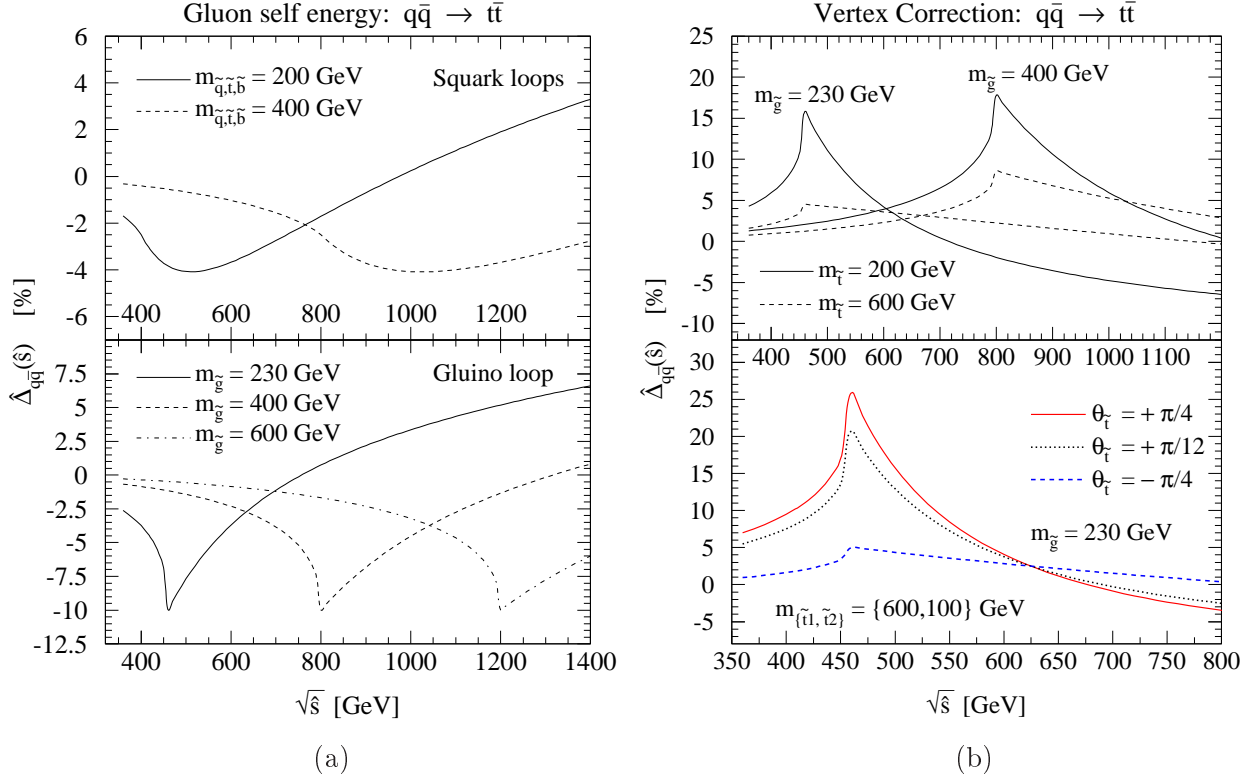


Figure 9: The relative correction $\hat{\Delta}_{q\bar{q}}(\hat{s})$ for $q\bar{q}$ annihilation due to (a) gluon self-energy and (b) vertex corrections (upper plot: $m_{\tilde{t}} \equiv m_{\tilde{t}_1} = m_{\tilde{t}_2}$).

GeV and different values of the stop mixing angle. The upper plot shows the direct box contribution of Fig. 4(a) and the lower plot the crossed box contribution of Fig. 4(b). The threshold peak at $\sqrt{\hat{s}} = 2m_{\tilde{g}}$ originates from the two gluinos occurring in the Feynman diagrams of Fig. 4. The corrections strongly depend on the stop mixing angle and in the threshold region are largest for $\theta_{\tilde{t}} = \pi/4$, and can be suppressed very effectively for $\theta_{\tilde{t}} = -\pi/4$. The direct and crossed box corrections have the same relative sign compared to the LO cross section, as discussed in Appendix B and are always negative in the threshold region. The direct box correction is usually three to four times larger than the crossed box contribution. Both box corrections depend on the masses of the spartners of the initial-state quarks. The corrections are small in this scenario, because of our choice of the squark masses, $m_{\tilde{q}} = 2$ TeV (for $m_{\tilde{q}} \gtrsim 1$ TeV the corrections hardly change anymore). The direct box correction increases for smaller squark masses, e.g., for $m_{\tilde{q}} = 200$ GeV at the gluino-pair threshold of $\sqrt{\hat{s}} = 460$ GeV to $\hat{\Delta}_{q\bar{q}} = -22\%$ (for $m_{\tilde{g}} = 230$ GeV, $m_{\tilde{t}_{1,2}} = 600, 100$ GeV, $\theta_{\tilde{t}} = +\pi/4$). However, the positive vertex correction also grows by the same amount and cancels the effect of the box corrections. We found that for every configuration with large box

corrections (and negative as always), the vertex corrections are positive and also large, so that both largely cancel, resulting into a small positive contribution to $\hat{\Delta}_{q\bar{q}}$. As already observed in the case of the vertex corrections, for top squarks degenerate in mass, $m_{\tilde{t}_1} = m_{\tilde{t}_2}$, the direct and crossed box corrections are independent of the top-squark mixing angle, and are largest for the smallest possible choice of their masses.

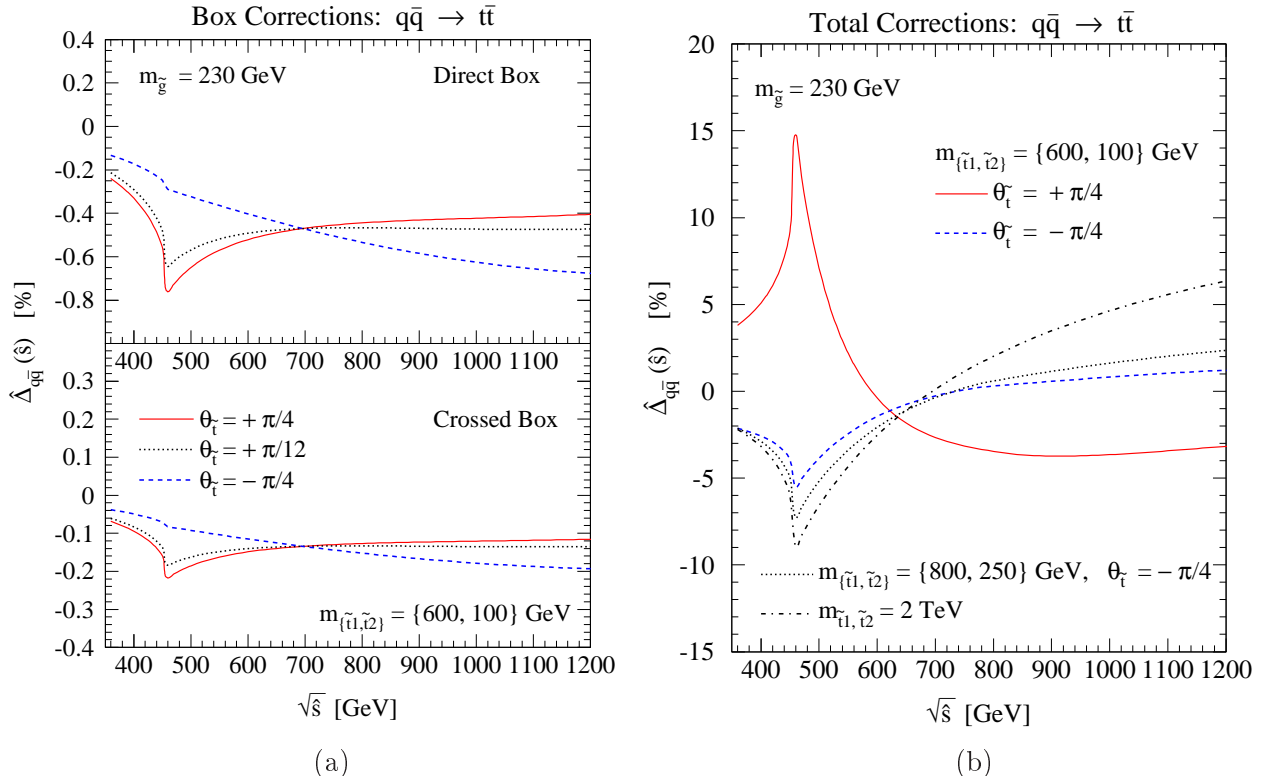


Figure 10: *The relative correction $\hat{\Delta}_{q\bar{q}}(\hat{s})$ for $q\bar{q}$ annihilation due to (a) box corrections and (b) when including the complete SQCD one-loop corrections for $m_{\tilde{g}} = 230$ GeV.*

One can now deduce from the detailed discussion above, for which MSSM scenarios the complete SQCD one-loop corrections, consisting of the sum of self-energy, vertex and box corrections (see Eq. (4)), affect the $q\bar{q} \rightarrow t\bar{t}$ total cross section the most. In Fig. 10(b), we show four representative scenarios, where we choose a light gluino mass of $m_{\tilde{g}} = 230$ GeV. If the top squarks are degenerate in mass, $m_{\tilde{t}_1} = m_{\tilde{t}_2}$, the corrections are independent of the squark mixing angle. If furthermore the stop masses are relatively light, i.e. smaller than 500 GeV, no large corrections occur because of a cancellation between the positive vertex correction and the negative gluon self-energy. Only if the stops are very heavy, i.e. about 2 TeV (dot-dashed line in Fig. 10(b)), the vertex and box corrections are strongly suppressed, and the negative gluon self-energy determines the NLO SQCD $u\bar{u} \rightarrow t\bar{t}$ cross section.

If the stops are non-degenerate in mass, the corrections strongly depend on $\theta_{\tilde{t}}$ (red solid line and blue dashed line in Fig. 10(b)). Large positive corrections can only occur, if the positive vertex correction becomes large (and all other, negative corrections are small) as is the case for $\theta_{\tilde{t}} = \pi/4$. Furthermore, the corrections are largest, if the lighter stop mass, $m_{\tilde{t}_2}$, is as light as allowed by the current mass limit, i.e. $m_{\tilde{t}_2} \approx 100$ GeV, and for the largest possible mass splitting. The smallest correction for top squarks non-degenerate in mass occurs for $\theta_{\tilde{t}} = -\pi/4$ because then the vertex correction is negligible and the total correction is again dominated by the negative gluon self-energy. For all other values of the stop mixing angle, the relative correction $\hat{\Delta}_{q\bar{q}}$ will lie between the red solid and blue dashed curves in Fig. 10(b).

2. Effects of NLO SQCD corrections in gluon fusion for unpolarized top quarks

Top-pair production at the LHC is dominated by gluon fusion and, thus, the discussion of the SQCD one-loop corrections to $gg \rightarrow t\bar{t}$ at parton level is a good indicator of what to expect at the LHC.

The impact of the gluon self-energy, top self-energy, and vertex corrections to the total partonic cross section in gluon fusion is shown in Fig. 11, in form of the relative correction $\hat{\Delta}_{gg}$ of Eq. (29). The gluon self-energy correction to $gg \rightarrow t\bar{t}$ is displayed in Fig. 11(a), where the upper and lower plot shows respectively the squark-loop (summed over all quark flavors and with squarks degenerate in mass) and gluino-loop contributions. Both corrections are positive and much less pronounced than in $q\bar{q}$ annihilation. This is because the s channel contribution to the gluon fusion cross section (see Fig. 5) reduces the total LO cross section by only 7%, interfering destructively with the t and u channels. For the same reason, the corrections are practically independent of the masses of the light squarks, since diagrams that contain \tilde{u} , \tilde{d} , \tilde{c} , \tilde{s} or \tilde{b} quarks occur only in the s channel correction.

The upper plot of Fig. 11(b) shows the effects of the off-shell top quark self-energy contribution in the t and u channels of gluon fusion (see Figs. 5(b)). Again the SQCD one-loop corrections are the larger the lighter the gluino and the stops. They are positive, increase with rising $\sqrt{\hat{s}}$ up to about $\hat{\Delta}_{gg} = +3\%$ at $\sqrt{\hat{s}} = 1200$ GeV. They strongly depend on the stop mixing angle, if the squarks are non-degenerate in mass, and become largest for $\theta_{\tilde{t}} = \pi/4$ (solid red line). A similar behavior can be observed, if $m_{\tilde{t}_1} = m_{\tilde{t}_2}$ and small,

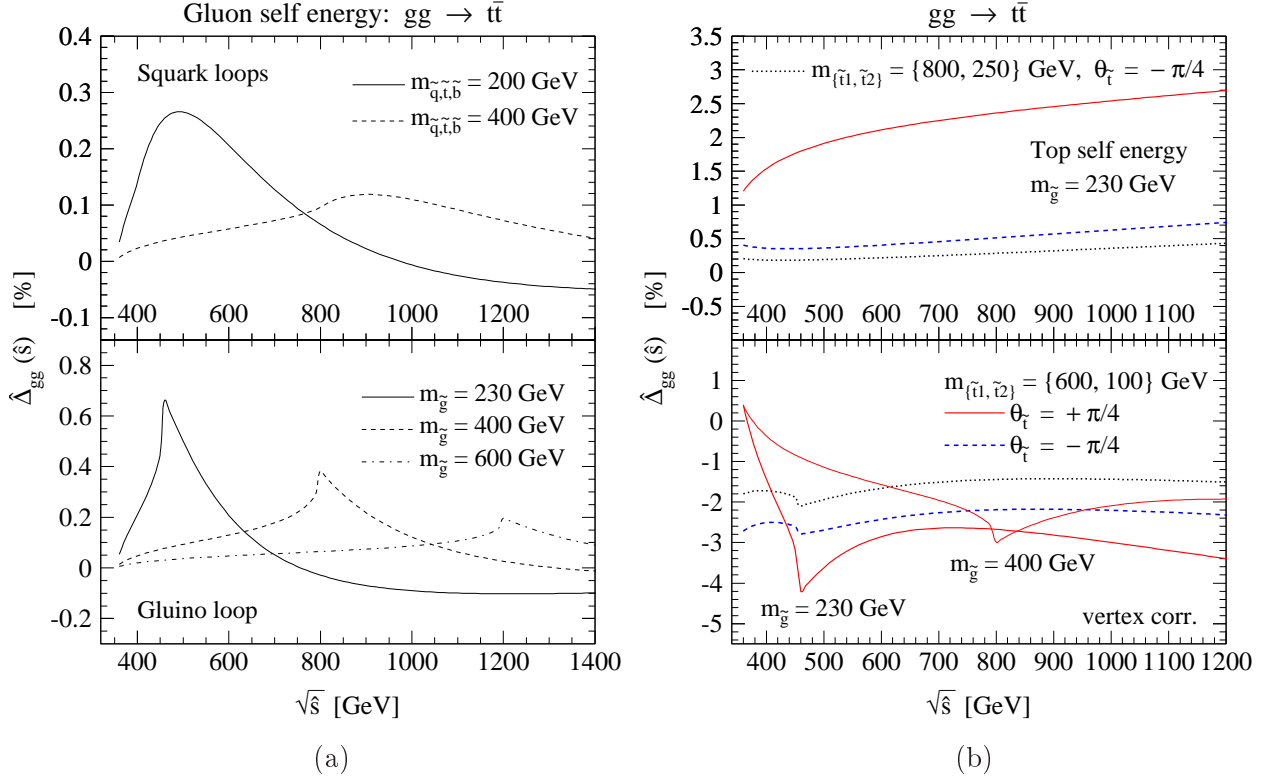


Figure 11: The relative correction $\hat{\Delta}_{gg}(\hat{s})$ for gluon fusion due to (a) gluon self-energy, (b)(upper plot) off-shell top quark self-energy, and (b)(lower plot) vertex corrections.

i.e. ≈ 200 GeV. With increasing stop masses this correction quickly decreases.

The effects of the vertex corrections are displayed in the lower plot of Fig. 11(b). The corrections are negative and exhibit the gluon-pair threshold behavior at $\sqrt{\hat{s}} = 2m_{\tilde{g}}$ due to the vertex diagrams including the $\tilde{g}\tilde{g}\tilde{t}_i$ loop (see Fig. 27). The largest corrections arise again for light gluino masses, a large mass splitting of the top squarks and small values of $m_{\tilde{t}_2}$. However, the influence of the mixing angle is small and changes the correction in the threshold region by maximally 1.2%. Again, if both top squarks become heavier the size of the corrections quickly decreases.

The largest corrections in gluon fusion arise due to the box diagrams of Fig. 6, as can be seen in Fig. 12(a). In the gluino-pair threshold region the corrections can reach up to $\hat{\Delta}_{gg} = +16\%$ for light gluino masses of 230 GeV, large mass splitting of the top squarks and $\theta_{\tilde{t}} = \pi/4$. The corrections depend again strongly on the stop mixing angle, if the stop masses are not equal, as displayed in the lower plot of Fig. 12(a). If $m_{\tilde{t}_1} = m_{\tilde{t}_2}$, the box corrections at the gluino-pair threshold reach $\hat{\Delta}_{gg} = +8\%$ for stop masses of 200 GeV and only $\hat{\Delta}_{gg} = +2\%$ for masses of 500 GeV.

Since the top self-energy and vertex correction add destructively and the gluon self-energy is negligible, the complete SQCD one-loop correction to gluon fusion is dominated by the box corrections and exhibits the same characteristics. This is illustrated in Fig. 12(b), where we show the impact of the complete SQCD one-loop correction to the partonic total cross section of gluon fusion for four different MSSM scenarios, which differ by the choices of top-squark masses and mixing angles. The corrections are practically independent of the light squark masses, $m_{\tilde{q}}$, because they contribute only to the gluon self-energy. The corrections are mostly positive, with a size of maximally $\hat{\Delta}_{gg} = +15\%$ at the gluino-pair threshold. They can become negative, reaching maximally $\hat{\Delta}_{gg} = -2.5\%$ for $\sqrt{\hat{s}} \approx 1$ TeV.

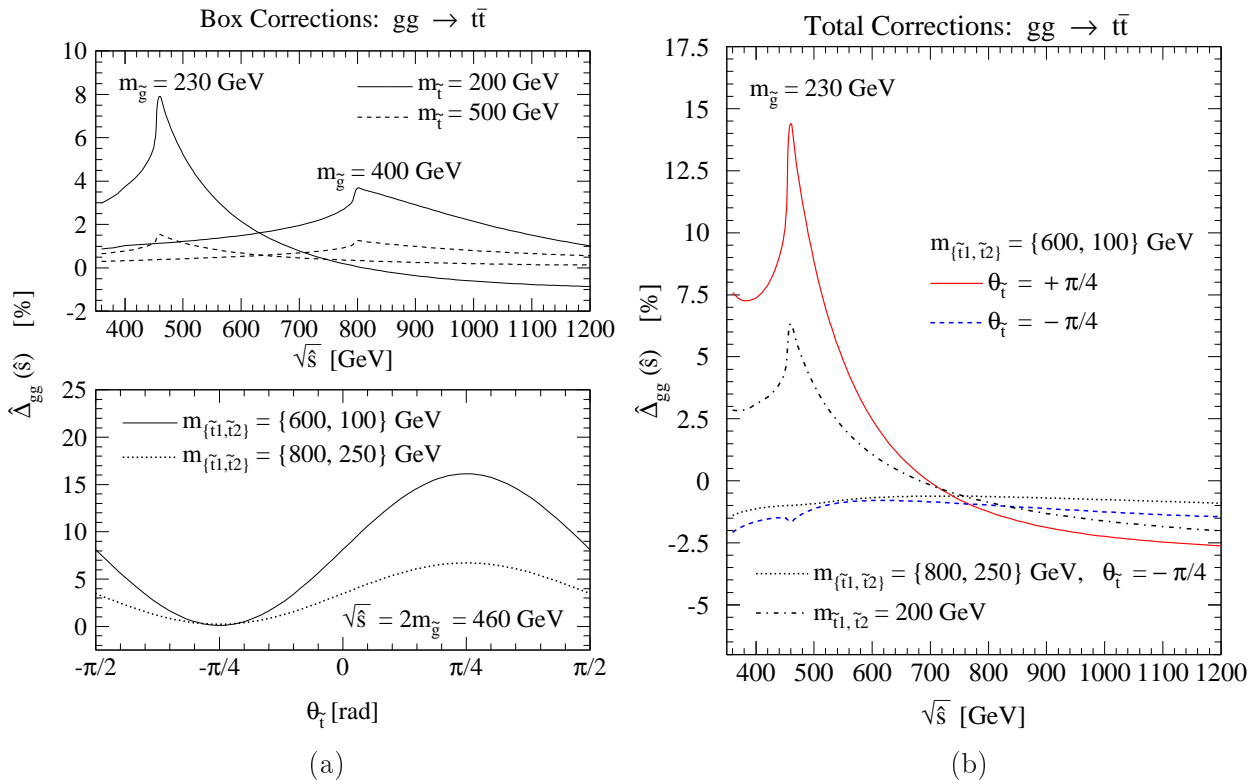


Figure 12: The relative correction $\hat{\Delta}_{gg}(\hat{s})$ for gluon fusion due to (a) box corrections (upper plot: $m_{\tilde{t}} \equiv m_{\tilde{t}_1} = m_{\tilde{t}_2}$) and (b) when including the complete SQCD one-loop corrections.

3. Hadronic cross sections to unpolarized $pp, p\bar{p} \rightarrow t\bar{t}$ at NLO SQCD

The effects of the NLO SQCD corrections to the hadronic cross sections result from the combination of the already discussed effects to the partonic cross sections and the PDFs (see Eq. (3)). The hadronic $t\bar{t}$ cross sections at the Tevatron Run II and the LHC are dominated

respectively by the quark and gluon PDFs, which both emphasize parton-level effects in the vicinity of the $t\bar{t}$ threshold, $\sqrt{\hat{s}} = 2m_t = 350$ GeV, but are rapidly decreasing for increasing values of $\sqrt{\hat{s}}$. The choice of the values for the MSSM input parameters, $m_{\tilde{g}}$, $m_{\tilde{t}_1}$, $m_{\tilde{t}_2}$ and $\theta_{\tilde{t}}$, is guided by the discussion of the SQCD effects at the parton level of Sections III A 1, III A 2. We first study the dependence of the relative correction Δ of Eq. (30) on the gluino and heavier stop masses for four different choices of the light stop mass and the stop mixing angle. These choices are representative for the possible choices that affect the $t\bar{t}$ cross sections the most.

The impact of the SQCD one-loop corrections on the total hadronic cross section in dependence of the gluino mass is shown in Fig. 13(a) for the Tevatron Run II and in Fig. 13(b) for the LHC. The corrections are largest for gluino masses of 200 – 250 GeV, since for these masses the gluino-pair threshold lies in the vicinity of the $t\bar{t}$ threshold. For $m_{\tilde{g}} = 230$ GeV the SQCD one-loop corrections vary between $\Delta = -4\%$ and $\Delta = +5\%$ at the Tevatron Run II, and between $\Delta = -1.5\%$ and $\Delta = +5.5\%$ at the LHC. They decrease to approximately $\Delta = -0.5\%$ (Tevatron Run II) and $\Delta = +1\%$ (LHC) for gluino masses of 500 GeV. Since large corrections always originate from the gluino-pair threshold, the relative corrections decrease for heavier gluinos.

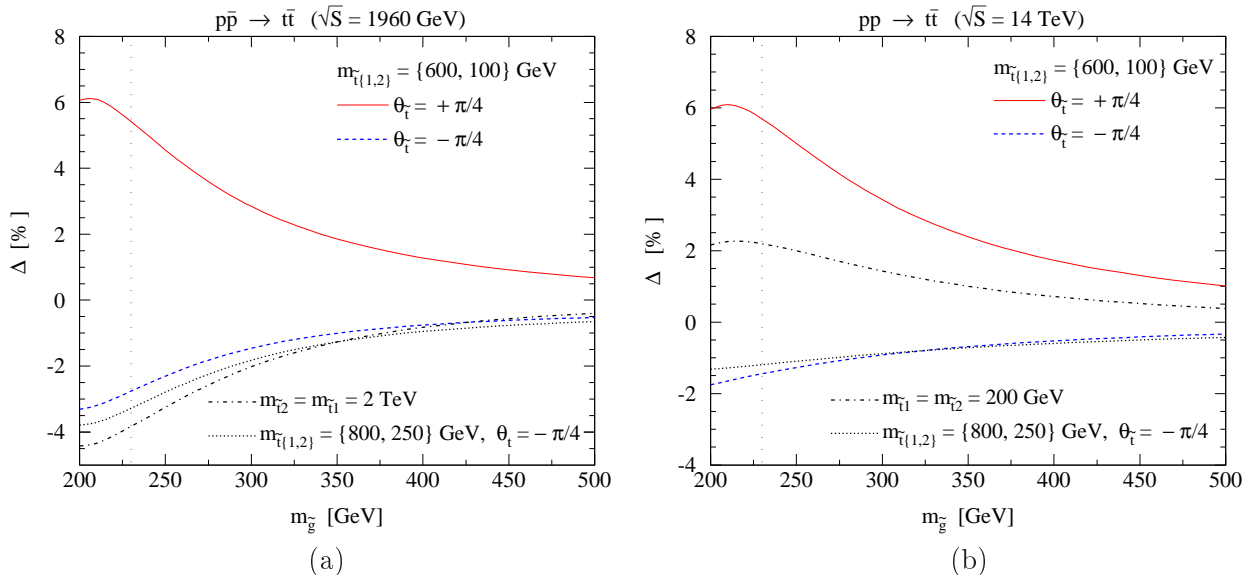


Figure 13: *The relative correction Δ due to SQCD one-loop corrections in dependence of the gluino mass, $m_{\tilde{g}}$, at (a) the Tevatron Run II and (b) the LHC.*

The influence of the top-squark masses on the SQCD one-loop corrections is shown in

Fig. 14(a) for the Tevatron Run II and in Fig. 14(b) for the LHC. Varied for these plots is either the heavier top-squark mass alone ($m_{\tilde{t}_1}$), or, in case of the dot-dashed line, both stop masses are varied together. The solid red, dashed blue and dotted black lines show that the corrections increase with increasing difference in the top-squark masses, as discussed at the parton level in Section III A 1, III A 2. The solid red and dashed blue lines end at $m_{\tilde{t}_1} \approx 650$ GeV and the dotted line at $m_{\tilde{t}_1} \approx 850$ GeV, because for larger values of $m_{\tilde{t}_1}$, the parameter $\Delta\rho$ exceeds the current limit of 0.0035 [71]. At the Tevatron Run II, if the top squarks are degenerate in mass, the largest correction arises for very large top-squark masses because then the correction is determined by the gluino loop in the gluon self-energy, which amounts to $\Delta \approx -4\%$ at hadron level. For $m_{\tilde{t}} > 2$ TeV the correction does not increase much anymore and stays at about $\Delta = -4\%$. At the LHC, the gluon self-energy plays a very minor role, and all other corrections depend on the top squark mass. Therefore, the corrections decouple and approach zero if both top squarks are heavy.

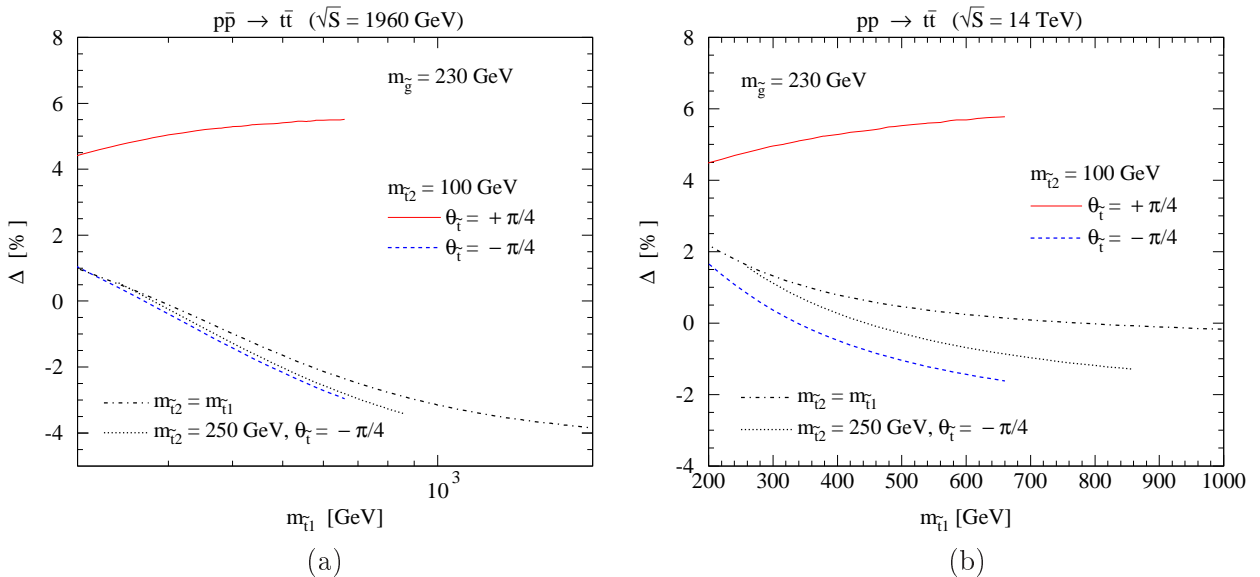


Figure 14: *The relative correction Δ due to SQCD one-loop corrections in dependence of the heavier top-squark mass, $m_{\tilde{t}_1}$, at (a) the Tevatron Run II and (b) the LHC.*

The relative corrections to the $M_{t\bar{t}}$ and p_T distributions of Eq. (30) are shown in Fig. 15 and Fig. 16, respectively. Both the $M_{t\bar{t}}$ and the p_T distribution exhibit the characteristic effects of the gluino-pair threshold, which can lead to a significant distortion of the shape of these distributions. At the Tevatron Run II, for instance, when choosing $m_{\tilde{t}_1, \tilde{t}_2} = 600, 100$ GeV, $\theta_{\tilde{t}} = \pi/4$ and $m_{\tilde{g}} = 230$ GeV, the corrections to the $M_{t\bar{t}}(p_T)$ distri-

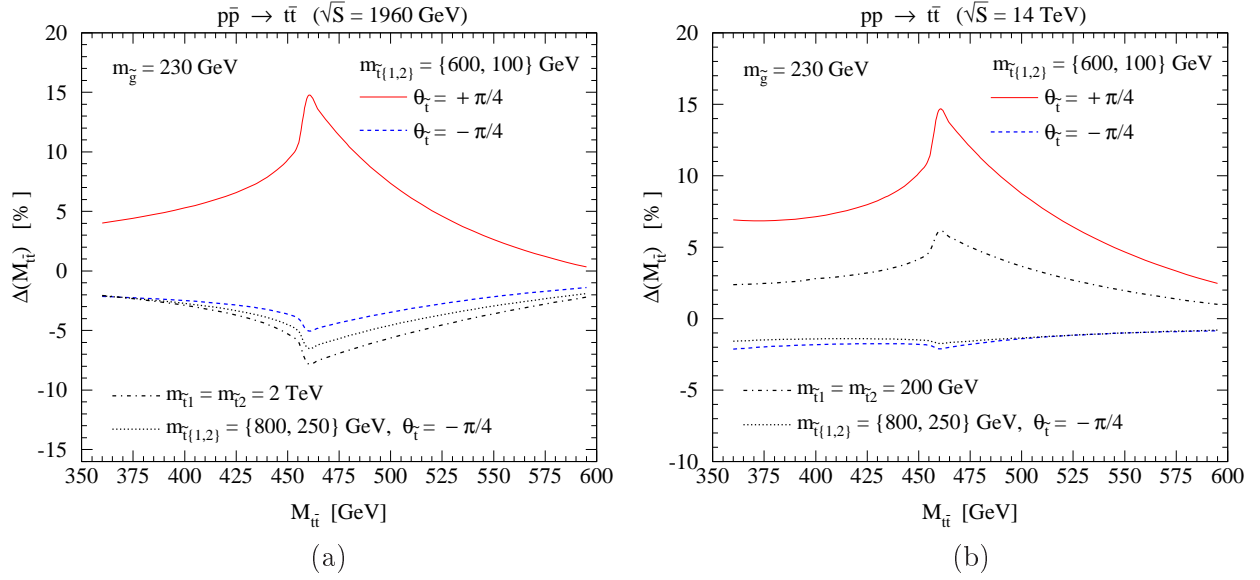


Figure 15: The relative correction $\Delta(M_{t\bar{t}})$ due to SQCD one-loop corrections at (a) the Tevatron Run II and (b) the LHC.

bution increase for $M_{t\bar{t}} < 460$ GeV ($p_T < 150$ GeV) and can enhance the LO distribution by up to $\Delta(M_{t\bar{t}})(\Delta(p_T)) = +15(+9.5)\%$ and then decrease quickly for larger values of $M_{t\bar{t}}(p_T)$. This behavior suggests that the relative corrections to the total $t\bar{t}$ cross section can be enhanced by applying cuts on the p_T of the top quark. For instance, when restricting the top quark p_T to the range 75 GeV $< p_T < 170$ GeV, the relative correction at the Tevatron Run II reaches $\Delta = +7.1\%$ (instead of $\Delta = +5.4\%$ without cuts, see Fig. 13). Keeping the same top-squark parameters but choosing $m_{\tilde{g}} = 260$ GeV and 100 GeV $< p_T < 210$ GeV, we find $\Delta = +5.5\%$ (instead of $\Delta = +4.1\%$ without cuts). At the LHC, choosing $m_{\tilde{t}_1, \tilde{t}_2} = 600, 100$ GeV, $\theta_{\tilde{t}} = \pi/4$, $m_{\tilde{g}} = 230$ GeV and 100 GeV $< p_T < 170$ GeV, we find $\Delta = +7.5\%$ (instead of $\Delta = +5.7\%$ without cuts). We also studied the effects of rapidity cuts and found that they do not affect the relative corrections much, because the NLO SQCD corrections are quite stable with respect to the rapidity distribution of the top quark.

In view of anticipated experimental uncertainties of about 10% and 5% in the total $t\bar{t}$ production rate at the Tevatron Run II and the LHC, respectively, and a current theoretical uncertainty of the QCD prediction of about 12% [10, 11], it will be difficult to reach sensitivity on SQCD effects in this observable. The $M_{t\bar{t}}$ and p_T distributions exhibit an interesting signature of SQCD one-loop corrections, but they are strongly affected in only a few bins and the final verdict on its observability must be left to an analysis, that includes for in-

stance top decays and the detector response. However, the inclusion of the known SUSY electroweak one-loop effects [47] may help to enhance SUSY loop-induced effects. First results of combined SUSY electroweak and SQCD one-loop corrections have been presented at the Tevatron in Ref. [56], but a detailed study at the LHC and the Tevatron Run II still needs to be done.

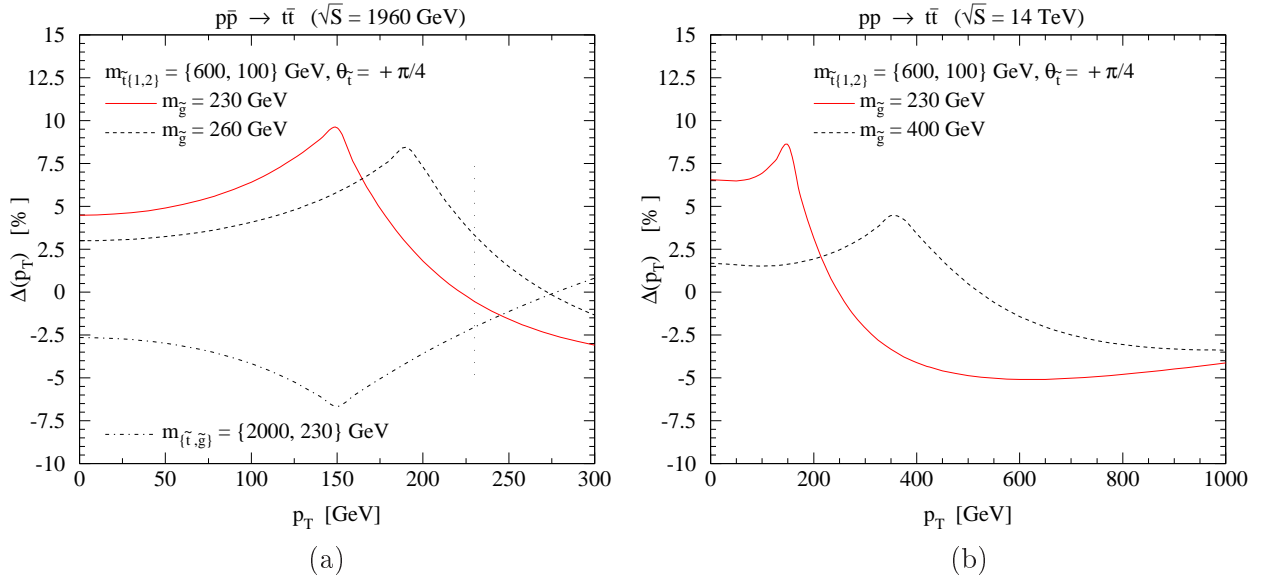


Figure 16: *The relative correction $\Delta(p_T)$ due to SQCD one-loop corrections at (a) the Tevatron Run II and (b) the LHC.*

B. Polarized top-pair production at NLO SQCD

In this section, we consider the production of polarized top-quark pairs at the Tevatron Run II and the LHC. We are working in the helicity basis of left- and right-handed top quarks, as discussed in Section II A. The incoming quarks and gluons are still considered to be unpolarized. In the following, we use the notation that the indices 'L' and 'R' denote left ($\lambda_{t(\bar{t})} = -1/2$) and right-handed ($\lambda_{t(\bar{t})} = +1/2$) top(antitop) quarks, respectively.

Since the SQCD couplings of gluinos and squarks contain an axial-vector part (see Appendix A, Fig. 24), the SQCD one-loop corrections may affect the production of left and right-handed top quarks differently. To study these differences in detail, we first discuss in Sections III B 1 ($q\bar{q}$ annihilation) and Section III B 2 (gluon fusion) the impact of the SQCD one-loop corrections on the total partonic $t\bar{t}$ cross sections of Eq. (1) for each top and antitop

helicity state separately, using the following relative corrections at the parton level:

$$\hat{\Delta}_{q\bar{q},gg}^{ab}(\hat{s}) = \frac{\hat{\sigma}_{q\bar{q},gg}^{NLO}(\lambda_t, \lambda_{\bar{t}}) - \hat{\sigma}_{q\bar{q},gg}^{LO}(\lambda_t, \lambda_{\bar{t}})}{\hat{\sigma}_{q\bar{q},gg}^{LO}(\lambda_t, \lambda_{\bar{t}})}, \quad (31)$$

with $ab = LL, RR$ denoting the relative correction for spin-like $t\bar{t}$ production with $\lambda_t = -1/2, \lambda_{\bar{t}} = -1/2$ and $\lambda_t = +1/2, \lambda_{\bar{t}} = +1/2$, respectively. Similarly, $ab = LR, RL$ denotes the relative correction for spin-unlike $t\bar{t}$ production with $\lambda_t = -1/2, \lambda_{\bar{t}} = +1/2$ and $\lambda_t = +1/2, \lambda_{\bar{t}} = -1/2$, respectively. Naturally, since QCD preserves parity, there is no difference in the spin-unlike amplitudes at LO QCD, i.e. $\hat{\sigma}_{q\bar{q},gg}^{LO}(+1/2, -1/2) = \hat{\sigma}_{q\bar{q},gg}^{LO}(-1/2, +1/2)$. Since we are not considering any CP violating couplings, the spin-like amplitudes are the same at both LO QCD and NLO SQCD, i.e. $\hat{\sigma}_{q\bar{q},gg}^{LO,NLO}(-1/2, -1/2) = \hat{\sigma}_{q\bar{q},gg}^{LO,NLO}(+1/2, +1/2)$.

Differences in the spin-unlike amplitudes at NLO SQCD manifest themselves in parity-violating polarization asymmetries, which we study in detail at hadron level in Section III B 3. We consider the following differential and integrated polarization asymmetries [12]:

- The left-right asymmetry in the $M_{t\bar{t}}$ distribution

$$\delta\mathcal{A}_{LR}(M_{t\bar{t}}) = \frac{d\sigma_{RL}/dM_{t\bar{t}} - d\sigma_{LR}/dM_{t\bar{t}}}{d\sigma_{RL}/dM_{t\bar{t}} + d\sigma_{LR}/dM_{t\bar{t}}} \quad (32)$$

and in the total hadronic $t\bar{t}$ cross section

$$\mathcal{A}_{LR} = \frac{\sigma_{RL} - \sigma_{LR}}{\sigma_{RL} + \sigma_{LR}}, \quad (33)$$

where we introduced the notation $d\sigma_{LR(RL)} \equiv d\sigma_{NLO}(\lambda_t = -1/2(+1/2), \lambda_{\bar{t}} = +1/2(-1/2))$ with the hadronic NLO SQCD cross sections of Eq. (3).

- The left-right asymmetry in the $M_{t\bar{t}}$ distribution, when assuming that the polarization of the antitop quark is not measured in the experiment (denoted by U =unpolarized),

$$\begin{aligned} \delta\mathcal{A}(M_{t\bar{t}}) &= \frac{(d\sigma_{RL}/dM_{t\bar{t}} + d\sigma_{RR}/dM_{t\bar{t}}) - (d\sigma_{LL}/dM_{t\bar{t}} + d\sigma_{LR}/dM_{t\bar{t}})}{(d\sigma_{RL}/dM_{t\bar{t}} + d\sigma_{RR}/dM_{t\bar{t}}) + (d\sigma_{LL}/dM_{t\bar{t}} + d\sigma_{LR}/dM_{t\bar{t}})} \\ &= \frac{d\sigma_{RU}/dM_{t\bar{t}} - d\sigma_{LU}/dM_{t\bar{t}}}{d\sigma_{NLO}/dM_{t\bar{t}}} \end{aligned} \quad (34)$$

and the corresponding asymmetry in the total hadronic $t\bar{t}$ cross section

$$\mathcal{A} = \frac{(\sigma_{RL} + \sigma_{RR}) - (\sigma_{LL} + \sigma_{LR})}{\sigma_{RL} + \sigma_{RR} + \sigma_{LL} + \sigma_{LR}} = \frac{\sigma_{RU} - \sigma_{LU}}{\sigma_{NLO}} \quad (35)$$

with the unpolarized NLO SQCD cross sections, $d\sigma_{NLO} = \sum_{\lambda_t, \lambda_{\bar{t}}=\pm 1/2} d\sigma_{NLO}(S, \lambda_t, \lambda_{\bar{t}})$. In this way, one complicated polarization measurement is avoided.

These parity-violating asymmetries are zero for stop mixing angles $\theta_{\tilde{t}} = \pm\frac{\pi}{4}$ (then $\lambda_j^A = 0$, see Appendix A) and top squarks degenerate in mass. The latter is due a cancellation of the parity-violating terms in the sum of the \tilde{t}_1 and \tilde{t}_2 contributions, since $\lambda_1^A = -\lambda_2^A$ and for equal stop masses the terms multiplying λ_A^j are the same.

In addition to the parity-violating polarization asymmetries, we study in Section III B 3 the spin correlation functions of Ref. [76], which are parity-conserving asymmetries in the spin-like and spin-unlike contributions to the $t\bar{t}$ cross sections. They are defined as follows:

$$\begin{aligned} \overline{C} &= \frac{(d\sigma_{RR}/dM_{t\bar{t}} + d\sigma_{LL}/dM_{t\bar{t}}) - (d\sigma_{LR}/dM_{t\bar{t}} + d\sigma_{RL}/dM_{t\bar{t}})}{(d\sigma_{RR}/dM_{t\bar{t}} + d\sigma_{LL}/dM_{t\bar{t}}) + (d\sigma_{LR}/dM_{t\bar{t}} + d\sigma_{RL}/dM_{t\bar{t}})} \\ &= \frac{(d\sigma_{RR}/dM_{t\bar{t}} + d\sigma_{LL}/dM_{t\bar{t}}) - (d\sigma_{LR}/dM_{t\bar{t}} + d\sigma_{RL}/dM_{t\bar{t}})}{d\sigma_{NLO}/dM_{t\bar{t}}} \end{aligned} \quad (36)$$

and

$$C = \frac{(\sigma_{RR} + \sigma_{LL}) - (\sigma_{LR} + \sigma_{RL})}{(\sigma_{RR} + \sigma_{LL}) + (\sigma_{LR} + \sigma_{RL})} = \frac{(\sigma_{RR} + \sigma_{LL}) - (\sigma_{LR} + \sigma_{RL})}{\sigma_{NLO}}. \quad (37)$$

1. Effects of NLO SQCD corrections in $q\bar{q}$ annihilation for polarized top quarks

In this section, we study the effects of the SQCD one-loop corrections on the partonic cross sections for polarized top quarks in $q\bar{q}$ annihilation. We are especially interested in the differences between the corrections to $t_L\bar{t}_R$ and $t_R\bar{t}_L$ production, since they will determine the size of the polarization asymmetries at hadron level at the Tevatron. As in the unpolarized case, we only show results for $u\bar{u} \rightarrow t\bar{t}$, representatively for all $q\bar{q}$ -initiated processes. In Fig. 17, we show the relative correction $\hat{\Delta}_{q\bar{q}}^{ab}$ of Eq. (31) for the sum of the direct and crossed box corrections, separately for each top(antitop) polarization state. The characteristics of the box corrections are similar to the ones observed in the unpolarized case, which we discussed in Section III A 1. In particular, the polarized box correction also exhibits the threshold behavior at $\sqrt{\hat{s}} = 2m_{\tilde{g}}$. Fig. 17(a) shows the correction in dependence of the partonic CMS energy for a small gluino mass of $m_{\tilde{g}} = 230$ GeV and for a choice of the stop mixing angle, where we expect the left-right asymmetry to be large. The dependence of the box correction on the stop mixing angle is shown in Fig. 17(b) with $\sqrt{\hat{s}}$ chosen to be at the gluino-pair threshold. As can be seen, the differences between the relative corrections to $t_L\bar{t}_R$ and $t_R\bar{t}_L$ production are largest for $\theta_{\tilde{t}} = \pm\pi/2, 0$.

In Fig. 18 we show the relative correction due to the complete SQCD one-loop correction in dependence of the partonic CMS energy (upper plots) and the stop mixing angle (lower

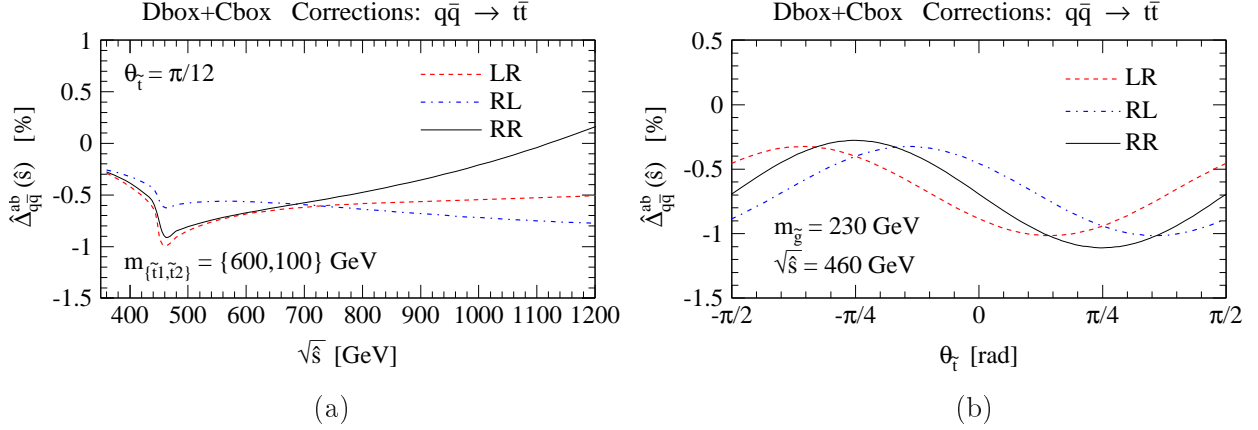


Figure 17: The relative corrections $\hat{\Delta}_{q\bar{q}}^{ab}(\hat{s})$ ($ab = LR, RL, RR = LL$) due to the box correction for polarized top-quark pairs in $q\bar{q}$ annihilation in dependence of (a) the partonic CMS energy and (b) the stop mixing angle.

plots). Since the box correction is very small compared to the complete correction, and the gluon self-energy is independent of the top(antitop) polarization (and thus cancel in the polarization asymmetries), the differences between the relative corrections to $t_L\bar{t}_R$ and $t_R\bar{t}_L$ production observed in Fig. 18 are mainly due to the vertex correction. Fig. 18(a) shows the corrections for $m_{\tilde{g}} = 230$ GeV and $m_{\tilde{t}_2} = 100$ GeV, and Fig. 18(b) the corrections for somewhat heavier particles, $m_{\tilde{g}} = 300$ GeV and $m_{\tilde{t}_2} = 250$ GeV. The vertex correction introduces large partonic left-right asymmetries in the gluino-pair threshold region and at high $\sqrt{\hat{s}}$ for $\theta_{\tilde{t}} = \pm\pi/2, 0$. Furthermore, as illustrated in Fig. 18 (lower plots), the largest relative corrections occur in spin-like top-pair production ($\hat{\Delta}_{q\bar{q}}^{RR} = \hat{\Delta}_{q\bar{q}}^{LL}$) at $\theta_{\tilde{t}} = \pm\pi/4$. In this case, the relative difference between the corrections to spin-like ($t_R\bar{t}_R, t_L\bar{t}_L$) and spin-unlike ($t_R\bar{t}_L, t_L\bar{t}_R$) top-pair production increases with increasing gluino mass. We found that if the stops are degenerate in mass, the corrections to spin-like and spin-unlike $t\bar{t}$ production are of comparable size. If in addition the top squarks are very heavy ($m_{\tilde{t}_1} = m_{\tilde{t}_2} \approx 2$ TeV), the corrections are completely independent of the top polarization states, because then they are determined by the gluon self-energy, as discussed in Section III A 1.

2. Effects of NLO SQCD corrections in gluon fusion for polarized top quarks

When studying the effects of the SQCD one-loop corrections on the partonic cross sections for polarized top quarks in gluon fusion, we again are especially interested in the differences

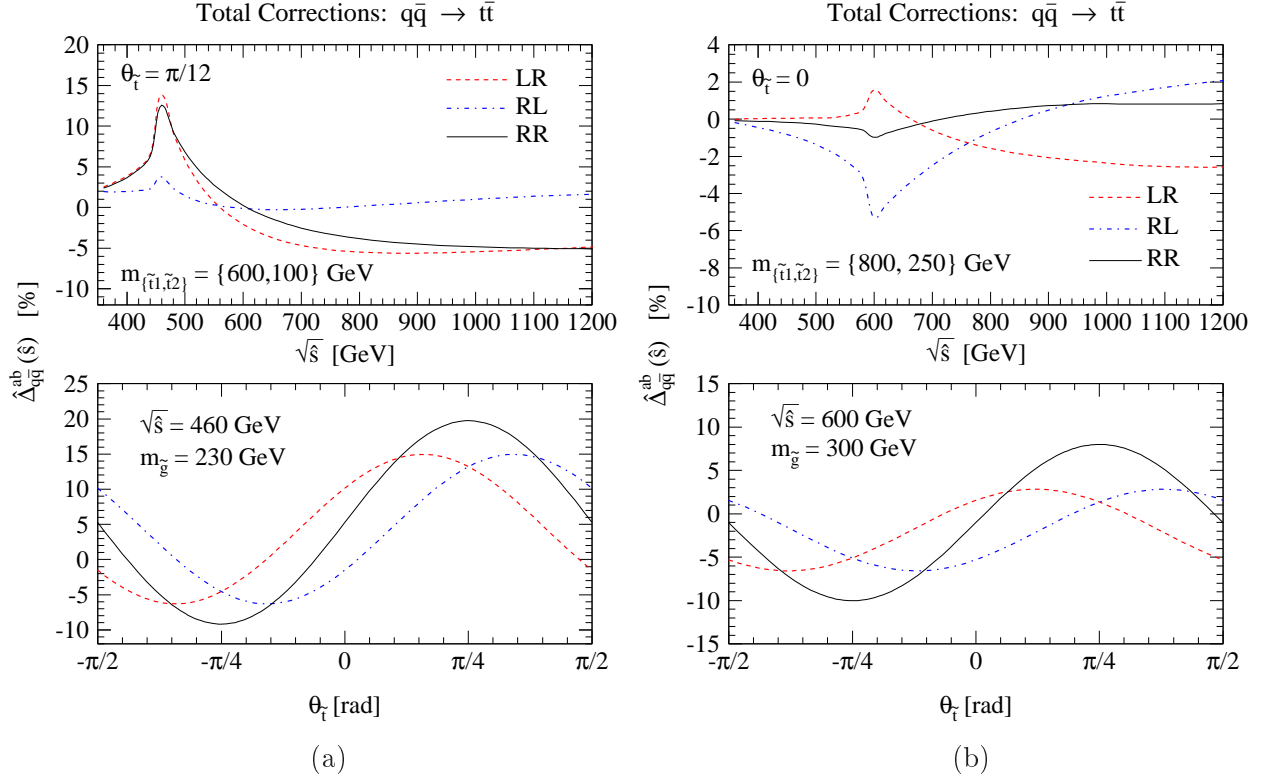


Figure 18: The relative corrections $\hat{\Delta}_{q\bar{q}}^{ab}(\hat{s})$ ($ab = LR, RL, RR = LL$) due to the complete SQCD one-loop corrections for polarized top-quark pairs in $q\bar{q}$ annihilation in dependence of the partonic CMS energy (upper plots) and the stop mixing angle (lower plots) for two sets of choices of the MSSM parameters: (a) $m_{\tilde{g}} = 230$ GeV, $m_{\tilde{t}_{1,2}} = 600, 100$ GeV and (b) $m_{\tilde{g}} = 300$ GeV, $m_{\tilde{t}_{1,2}} = 800, 250$ GeV.

between $t_R\bar{t}_L$ and $t_L\bar{t}_R$ production, since this will determine the size of the polarization asymmetries at hadron level at the LHC. As for $q\bar{q}$ annihilation, also in gluon fusion the gluon self-energy correction is independent of the top(antitop) polarization states. In Fig. 19(a) we therefore show the relative corrections $\hat{\Delta}_{gg}^{ab}$ of Eq. (31) separately only for the top self-energy and vertex corrections, choosing $m_{\tilde{g}} = 230$ GeV and $m_{\tilde{t}_{1,2}} = 600, 100$ GeV. As can be seen, the top self-energy and the vertex corrections depend strongly on the polarizations of the top and antitop quarks, inducing differences between the corrections to $t_R\bar{t}_L$ and $t_L\bar{t}_R$ production of several percent. However, the partonic left-right asymmetries due to these two corrections are of opposite sign and therefore almost cancel in the complete SQCD one-loop correction. Also the corrections to spin-like top-pair production have opposite signs and interfere destructively. Therefore, the relative correction due to the complete SQCD one-loop correction, shown in Fig. 19(b), is largely determined by the box correction.

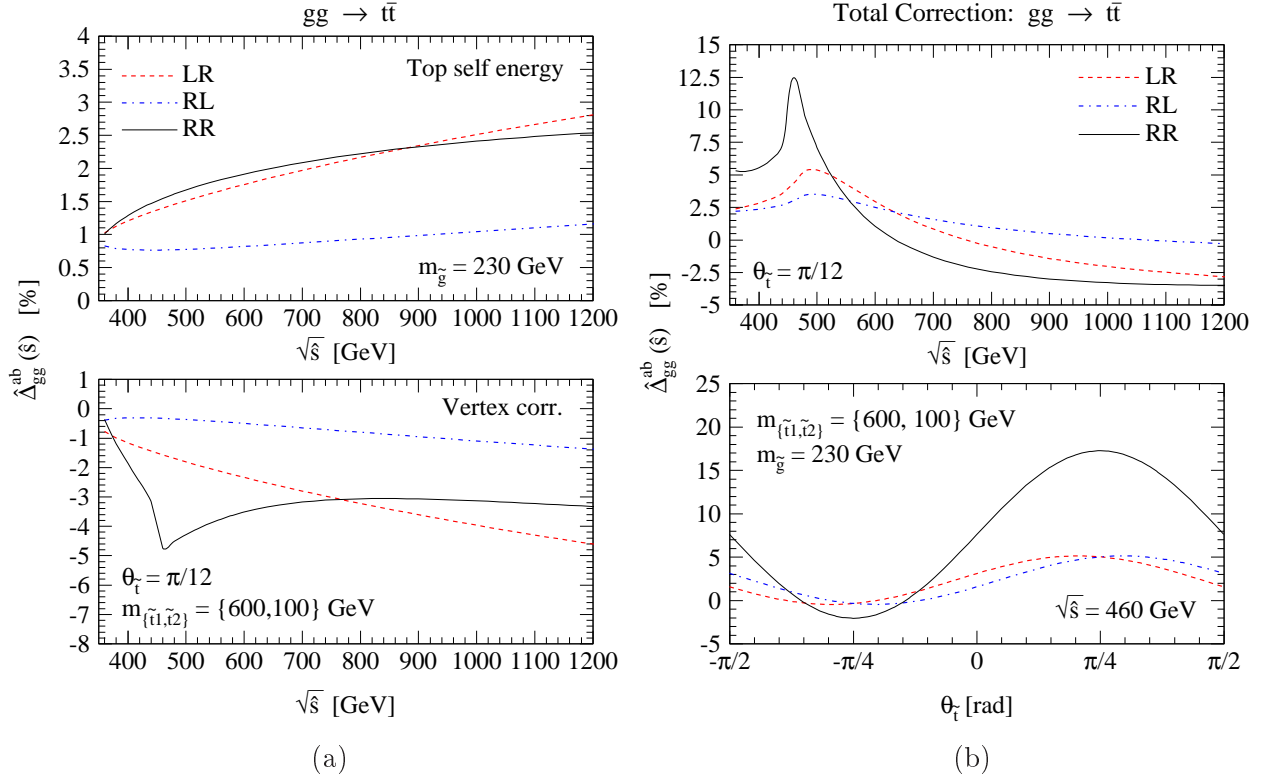


Figure 19: The relative corrections $\hat{\Delta}_{gg}^{ab}(\hat{s})$ ($ab = LR, RL, RR = LL$) for polarized top-quark pairs in gluon fusion due to (a) top self-energy and vertex corrections and (b) the complete SQCD one-loop correction in dependence of the partonic CMS energy. Also shown is the stop mixing angle dependence of the complete SQCD one-loop correction ((b) lower plot).

The relative correction for spin-like top-pair production is much larger than the one for $t_R\bar{t}_L, t_L\bar{t}_R$ production, which is still the case for larger values of $m_{\tilde{g}}$. The difference in the box correction to $t_R\bar{t}_L$ and $t_L\bar{t}_R$ production is relatively small and therefore also the partonic left-right asymmetry induced by the complete SQCD one-loop corrections is small.

3. Hadronic cross sections to polarized $pp, p\bar{p} \rightarrow t\bar{t}$ at NLO SQCD

In the following discussion of parity violating effects in polarized $t\bar{t}$ production at the Tevatron Run II and the LHC, we benefit from the detailed study of these effects at the parton level in Sections IIIB 1, IIIB 2, so that we can restrict our discussion to the following two sets of choices for the stop masses and mixing angle:

$$(I) \quad m_{\tilde{t}_1} = 600 \text{ GeV}, \quad m_{\tilde{t}_2} = 100 \text{ GeV}, \quad \theta_{\tilde{t}} = \pi/12$$

$$(II) \quad m_{\tilde{t}_1} = 800 \text{ GeV}, \quad m_{\tilde{t}_2} = 250 \text{ GeV}, \quad \theta_{\tilde{t}} = 0 \quad (38)$$

and to a few values of the gluino mass. These parameter sets are representative for the choices that yield the largest numerical impact. The top-squark mixing angle of set (I) is chosen to be $\pi/12$ instead of zero, since in this case smaller values of $\theta_{\tilde{t}}$ render the soft supersymmetry breaking mass $M_{\tilde{t}_R}^2$ negative.

At the Tevatron Run II, the integrated left-right asymmetries in the total hadronic cross section of Eqs. (33), (35) are largest for set (I): We find $\mathcal{A}_{LR} = -1.08\%$, $\mathcal{A} = -0.79\%$ for $m_{\tilde{g}} = 230 \text{ GeV}$, and $\mathcal{A}_{LR} = -0.72\%$, $\mathcal{A} = -0.53\%$ for $m_{\tilde{g}} = 300 \text{ GeV}$. These small asymmetries are clearly not observable at the Tevatron: For instance, the statistical significance N_S of Eq. (19) in Ref. [12] only amounts to $N_S = 2.0(1.7)$ for $|\mathcal{A}_{LR}| = 1.08\%$ ($|\mathcal{A}| = 0.79\%$) for an integrated luminosity of $\mathcal{L} = 8 \text{ fb}^{-1}$, while conservatively $N_S > 4$ is required to be statistically significant. In Fig. 20(a) we show the parity-violating asymmetries in the $M_{t\bar{t}}$ distribution, $\delta\mathcal{A}_{LR}(M_{t\bar{t}})$ of Eq. (32) and $\delta\mathcal{A}(M_{t\bar{t}})$ of Eq. (34), for sets (I) and (II) and a gluino mass of 230 GeV and 300 GeV. The asymmetry $\delta\mathcal{A}(M_{t\bar{t}})$ could be an interesting observable at the Tevatron, since the cross sections for the spin-like polarization states ($t_L\bar{t}_L, t_R\bar{t}_R$) are much smaller than the ones for the spin-unlike polarization states ($t_L\bar{t}_R, t_R\bar{t}_L$) and, thus, do not significantly decrease this asymmetry compared to $\delta\mathcal{A}_{LR}(M_{t\bar{t}})$. Due to characteristic peaks at the gluino-pair threshold, $\delta\mathcal{A}(M_{t\bar{t}})$ can reach -3.4% (-4.1%) for set (I) and $m_{\tilde{g}} = 230(300) \text{ GeV}$, and -2.1% (-3.0%) for the heavier top-squark mass set (II). If the polarization of the antitop quark is also measured, the resulting left-right asymmetry $\delta\mathcal{A}_{LR}(M_{t\bar{t}})$ of Eq. (32) could reach -4.7% (set (I) and $m_{\tilde{g}} = 230 \text{ GeV}$) and -4.6% (set (I) and $m_{\tilde{g}} = 300 \text{ GeV}$).

In Fig. 20(b), we show the parity-violating asymmetries in the $M_{t\bar{t}}$ distribution of Eqs. (32), (34) at the LHC. Since at the LHC the cross section of $t_R\bar{t}_R, t_L\bar{t}_L$ production is much larger (roughly three times) than the one for $t_L\bar{t}_R, t_R\bar{t}_L$ production, the asymmetries $\delta\mathcal{A}(M_{t\bar{t}}), \mathcal{A}$ of Eqs. (34), (35) are significantly smaller than $\delta\mathcal{A}_{LR}(M_{t\bar{t}}), \mathcal{A}_{LR}$ of Eqs. (32), (33). At the LHC, the left-right asymmetry $\delta\mathcal{A}_{LR}(M_{t\bar{t}})$ reaches a maximum for set (I) of -2.0% for $m_{\tilde{g}} = 230 \text{ GeV}$ and -1.1% for $m_{\tilde{g}} = 400 \text{ GeV}$. In comparison, if the polarization of the antitop quark is not measured, we find for the same set of MSSM parameters that $\delta\mathcal{A}(M_{t\bar{t}})$ is maximally -0.64% and -0.58% . The asymmetries in the total hadronic cross section, \mathcal{A}_{LR} of Eq. (33) and \mathcal{A} of Eq. (35), reach for set (I) a maximum value of -0.24% and -0.08% for $m_{\tilde{g}} = 230 \text{ GeV}$ and -0.37% and -0.13% for $m_{\tilde{g}} = 280 \text{ GeV}$. For set (II) the

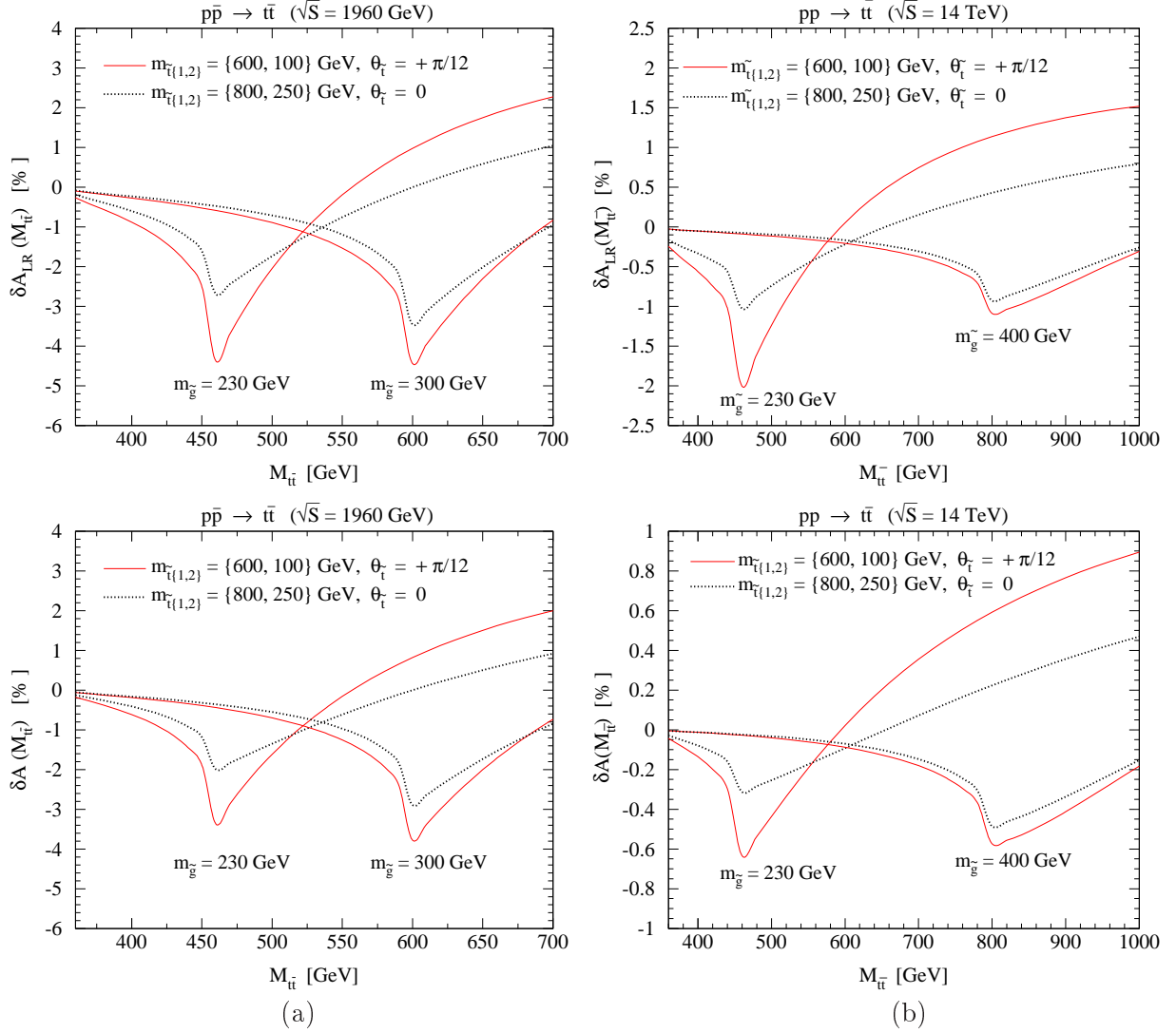


Figure 20: *Parity-violating asymmetries in the $M_{t\bar{t}}$ distribution for polarized top-quark pairs (upper plots) and for polarized top and unpolarized antitop quarks (lower plots) at (a) the Tevatron Run II and (b) the LHC.*

asymmetries are maximal at roughly $m_{\tilde{g}} = 300$ GeV with $\mathcal{A}_{LR} = -0.26\%$ and $\mathcal{A} = -0.09\%$. For both parameter sets, \mathcal{A}_{LR} and \mathcal{A} decrease slowly for heavier gluinos. At the LHC, integrated parity-violating asymmetries as small as 0.1% may be accessible: For instance, we find statistical significances of $N_S = 9.0(5.3)$ for $|\mathcal{A}_{LR}| = 0.37\%(|\mathcal{A}| = 0.13\%)$ (with $\mathcal{L} = 30 \text{ fb}^{-1}$).

In the remaining part of this section we will provide numerical results for the spin correlation functions of Eqs. (36), (37) at the LHC. Fig. 21(a) shows the difference between the LO QCD and NLO SQCD predictions for the spin correlation function C of Eq. (36)

in dependence of the top-squark mixing angle. A comparison of the LO QCD and NLO SQCD predictions for the spin correlation function \overline{C} of Eq. (37) is shown in Fig. 21(b). The LO QCD predictions are obtained from Eqs. (36), (37) by replacing the NLO cross section with the LO cross sections. As shown in Fig. 19(b), the SQCD one-loop corrections to the $t_R\bar{t}_R, t_L\bar{t}_L$ and $t_L\bar{t}_R, t_R\bar{t}_L$ production can differ considerably, resulting in large deviations from the LO QCD prediction for C , and thus can lead to potentially observable effects at the LHC. Since this difference strongly depends on the stop mixing angle, this spin correlation function may have the potential for extracting information about $\theta_{\tilde{t}}$. In Fig. 22, we

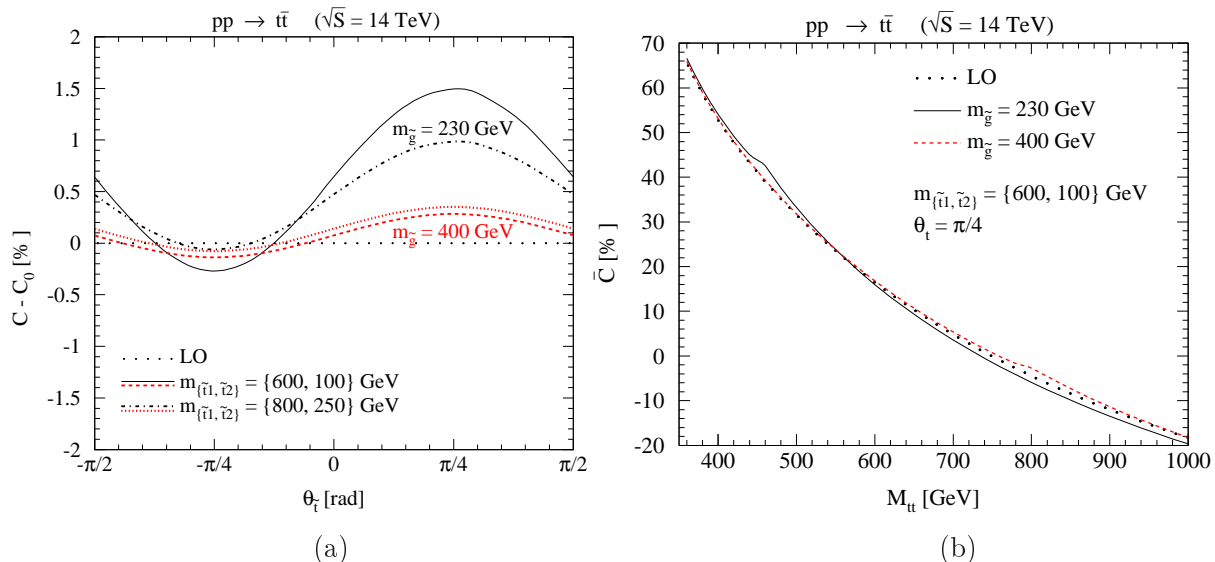


Figure 21: Spin correlation functions in polarized $t\bar{t}$ production at the LHC at LO QCD and NLO SQCD. Shown is (a) the difference between the LO QCD and NLO SQCD spin correlation functions, C_0 and C , in dependence of the top-squark mixing angle $\theta_{\tilde{t}}$ and (b) \overline{C} in dependence of the invariant $t\bar{t}$ mass.

discuss the difference between the LO QCD (\overline{C}_0) and NLO SQCD (\overline{C}) predictions for the spin correlation function of Eq. (37) in more detail. As can be seen in Fig. 22(a), a deviation from the LO QCD prediction of maximal 3.7% can be achieved for light stop and gluino masses and a top-squark mixing angle of $\theta_{\tilde{t}} = \pi/4$. Since the spin correlation functions C, \overline{C} do not suffer from luminosity uncertainties (they cancel in the cross section ratios), and due to the high $t\bar{t}$ yield at the LHC, they may be interesting observables to search for loop-induced SUSY effects in $t\bar{t}$ production. To see how these effects compare to theoretical uncertainties in the predictions for \overline{C} we show again in Fig. 22(b) the difference $\overline{C}_X - \overline{C}_0$

with $\overline{C}_X = \overline{C}$ for $m_{\tilde{t}_1} = 600$ GeV, $m_{\tilde{t}_2} = 100$ GeV, $\theta_{\tilde{t}} = \pi/4$ and a light and heavier gluino, together with the uncertainty bands induced by the LO QCD scale dependence, varied between $m_t/2 < \mu_F = \mu_R < 2m_t$, and an experimental top-mass uncertainty of $\Delta m_t = 1$ GeV. The bands are calculated with \overline{C}_X being the LO spin correlation function for different values of m_t and μ_R, μ_F , and \overline{C}_0 is calculated for $m_t = \mu_F = \mu_R = 175$ GeV. Since the scale uncertainty is obtained at LO QCD, we expect the corresponding band to be considerably less pronounced when including the known QCD NLO results [23, 24, 25, 26, 27, 28]. In view of an anticipated relative experimental error on \overline{C} of about 4% [77], this observable has the potential to be sensitive to loop-induced SUSY effects.

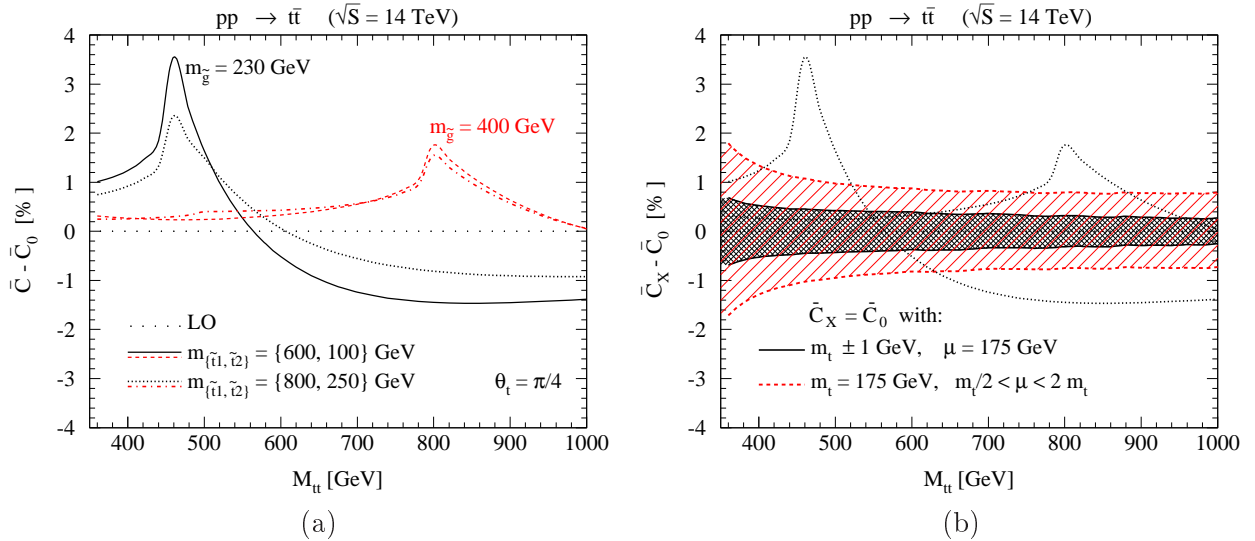


Figure 22: *Difference between the LO QCD and NLO SQCD spin correlation functions, \overline{C}_0 and \overline{C} , at the LHC in dependence of the invariant $t\bar{t}$ mass. In (b) we compare the NLO SQCD prediction for this difference (dotted lines with $\overline{C}_X = \overline{C}$ and $m_{\tilde{t}_1} = 600$ GeV, $m_{\tilde{t}_2} = 100$ GeV, $\theta_{\tilde{t}} = \pi/4$, $m_{\tilde{g}} = 230, 400$ GeV) to the LO QCD prediction with \overline{C}_X describing the LO spin correlation function for varying top mass and renormalization and factorization scales. The bands are obtained due to a variation of m_t by ± 1 GeV (grey, cross-hatched band with the lower line corresponding to $m_t - 1$ GeV and the upper line to $m_t + 1$ GeV) and due to a variation of μ_F and μ_R by $m_t/2 < \mu_F = \mu_R < 2m_t$ (red, hatched band). \overline{C}_0 in (a) and (b) is calculated for $m_t = \mu_F = \mu_R = 175$ GeV.*

C. Comparison with existing calculations

The NLO SQCD corrections to $q\bar{q} \rightarrow t\bar{t}$ for unpolarized top quarks have also been calculated in Refs. [53, 54, 55], however in Ref. [53] the contribution of the gluon self-energy and the crossed box diagram (Fig. 4(b)) is missing. We compared our results analytically and numerically with those presented in Refs. [54, 55] and found agreement, if we adjust for a missing (-1) sign for the direct box (Fig. 4(a)) contribution in Ref. [54] and missing (-1) signs for the direct (Fig. 4(a)) and crossed box (Fig. 4(b)) contributions of Ref. [55]. A detailed discussion of the box contributions can be found in Appendix B. The NLO SQCD corrections to gluon fusion for unpolarized top quarks have also been calculated in Ref. [50]. When we use their choices of the SM and MSSM input parameters and assume $\alpha_s = 0.120$ we were able to reproduce the numerical results presented in the figures of Ref. [50].

IV. CONCLUSION

We studied in detail the effects of SQCD one-loop corrections to the main production processes for polarized and unpolarized strong $t\bar{t}$ production, $q\bar{q} \rightarrow t\bar{t}$ and $gg \rightarrow t\bar{t}$, at the Tevatron Run II and the LHC. We presented numerical results for the total $t\bar{t}$ production rate, the invariant $t\bar{t}$ mass and top transverse momentum distributions in unpolarized $t\bar{t}$ production and for a number of asymmetries in polarized $t\bar{t}$ production for different choices of the MSSM input parameters, $m_{\tilde{g}}$, $m_{\tilde{t}_1}$, $m_{\tilde{t}_2}$ and $\theta_{\tilde{t}}$. We found that the largest corrections occur for the lightest gluino allowed by current experimental limits and large stop-mass splittings. For instance, for $m_{\tilde{t}_1}, m_{\tilde{t}_2} = 600, 100$ GeV and $\theta_{\tilde{t}} = \pi/4$, the SQCD one-loop corrections enhance the LO total hadronic $t\bar{t}$ cross section by 7.1% (when restricting the top quark p_T to $75 \text{ GeV} < p_T < 170 \text{ GeV}$) at the Tevatron Run II for $m_{\tilde{g}} = 230$ GeV and by 7.5% ($100 \text{ GeV} < p_T < 210 \text{ GeV}$) at the LHC for $m_{\tilde{g}} = 260$ GeV. The NLO SQCD $M_{t\bar{t}}$ and p_T distributions can be significantly distorted due to a gluino-pair production threshold at $\sqrt{\hat{s}} = 2m_{\tilde{g}}$. For $M_{t\bar{t}}$ and p_T values in the vicinity of this threshold, the SQCD one-loop corrections can enhance the LO $M_{t\bar{t}}$ and p_T distributions by 15% and 9.5%, respectively. When considering polarized $t\bar{t}$ production, we studied the effects on parity-violating and parity-conserving asymmetries in the total hadronic cross section and the $M_{t\bar{t}}$ distribution. We found that in view of the anticipated top-quark yield at the Tevatron Run II, it will

be difficult to observe loop-induced SUSY effects in polarization asymmetries. At the LHC, however, we find promising effects: The parity-violating asymmetries in the production of left and right-handed top and antitop quarks can reach up to $|\delta\mathcal{A}_{LR}(M_{t\bar{t}})| = 2.0\%$ in the $M_{t\bar{t}}$ distribution and $|\mathcal{A}_{LR}| = 0.37\%$ in the total hadronic cross section. The parity-conserving spin correlation function, \overline{C} , that describes an asymmetry in the $M_{t\bar{t}}$ distributions of spin-like and spin-unlike $t\bar{t}$ production can differ from the LO QCD prediction by up to 3.7%. These effects are promising enough to motivate a future study which includes top-quark decays and the detector response, in order to determine whether they are observable at the LHC. Such a study should also include SM and SUSY electroweak one-loop corrections, since they can either enhance or diminish the SQCD induced effects.

Acknowledgments

We thank F. I. Olness, W. Bernreuther, S. Heinemeyer and B. Kehoe for discussion. W.M. M. is grateful for the kind hospitality extended to him by the Particle Physics Theory Group of the Paul-Scherrer Institut, where part of this work was done. D. W. is particularly grateful to D. Dicus for the opportunity to spend a research semester at the Center for Particles and Fields of the University of Texas at Austin, where a substantial part of this work was completed, supported in part by the U.S. Department of Energy under grant DE-FG03-93ER40757. This research is supported in part by the European Community's Marie-Curie Research Training Network under contract MRTN-CT-2006-035505 *Tools and Precision Calculations for Physics Discoveries at Colliders* (HEPTOOLS). The work of D. W. is supported in part by the National Science Foundation under grants NSF-PHY-0244875, NSF-PHY-0456681 and NSF-PHY-0547564. The work of S. B. is supported in part by the U.S. Department of Energy under grant DE-FG03-95ER40908, Contract W-31-109-ENG-38, by the Lightner-Sams Foundation, and by Deutsche Forschungsgemeinschaft SFB/TR9.

Appendix A: FEYNMAN RULES

The relevant QCD Lagrangian of the MSSM is given in Ref. [6] with the convention of the covariant derivative $D_\mu = \partial_\mu + ig_s G_\mu^a T^a$ with the gluon field G_μ^a , strong coupling parameter

$g_s = \sqrt{4\pi\alpha_s}$, and $T^a = \lambda^a/2$, where λ^a denote the Gell-Mann-matrices. Furthermore the methods of Ref. [66] are applied to address Feynman graphs containing Majorana particles. In [66] a ‘‘fermion flow’’, denoted by a thin line with arrow, is introduced in addition to the standard ‘‘fermion number flow’’ to deal with diagrams containing fermion number violating fermion chains. The relevant SQCD Feynman rules used in this paper are given in Figs. 23-25.

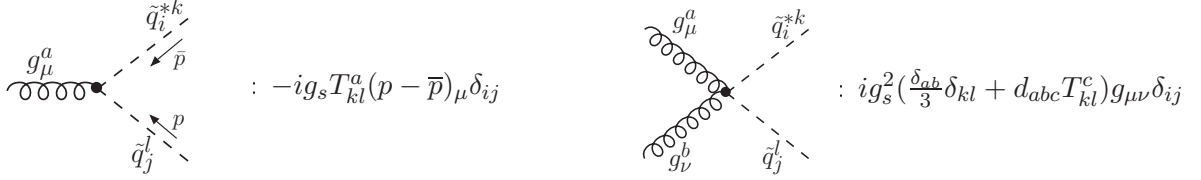


Figure 23: The Feynman rules for the triple and quartic squark-gluon interactions. $a, b, c = 1 \dots 8$ and $k, l = 1 \dots 3$ are color indices and $i, j = L, R$ and $i, j = 1, 2(L, R)$ with(without) mixing are the squark indices. Here d^{abc} is total symmetric, defined by $d^{abc} = 2\text{Tr}[\{T^a, T^b\}T^c]$.

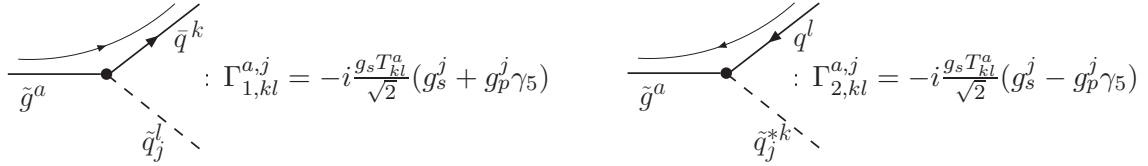


Figure 24: The \tilde{g} - \tilde{q}_j - q vertex written in generalized form in terms of scalar and pseudo scalar couplings, $g_{s,p}^{L,R}$, with $g_s^{L,R} = \pm 1$ and $g_p^{L,R} = 1$. The thin line with arrow represents the fermion flow of Ref. [66].

When considering \tilde{q}_L - \tilde{q}_R -mixing the interaction eigenstates are replaced by the mass eigenstates in the interaction Lagrangian, as discussed in Section II C, which has the following impact on the squark couplings of Fig. 24:

$$\begin{aligned}
 g_s^{1,2} &= \cos \theta_{\tilde{q}} g_s^{L,R} \pm \sin \theta_{\tilde{q}} g_s^{R,L} \\
 g_p^{1,2} &= \cos \theta_{\tilde{q}} g_p^{L,R} \pm \sin \theta_{\tilde{q}} g_p^{R,L} .
 \end{aligned}
 \tag{A1}$$

For convenience we introduce the abbreviations

$$\lambda_j^\pm = (g_s^j)^2 \pm (g_p^j)^2 \quad \text{and} \quad \lambda_j^A = 2g_s^j g_p^j .
 \tag{A2}$$

The SM QCD Feynman rules which we need to calculate the $t\bar{t}$ cross sections are given in Fig. 26.

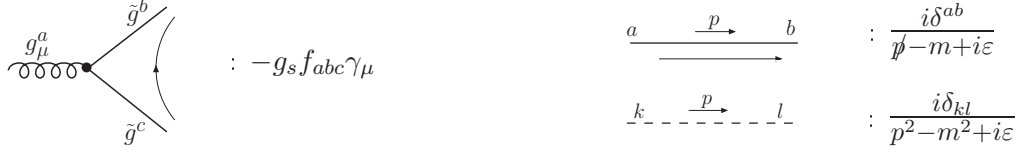


Figure 25: The g - \tilde{g} - \tilde{g} - vertex with the SU(3) structure constants f_{abc} , and the gluino and squark propagators.

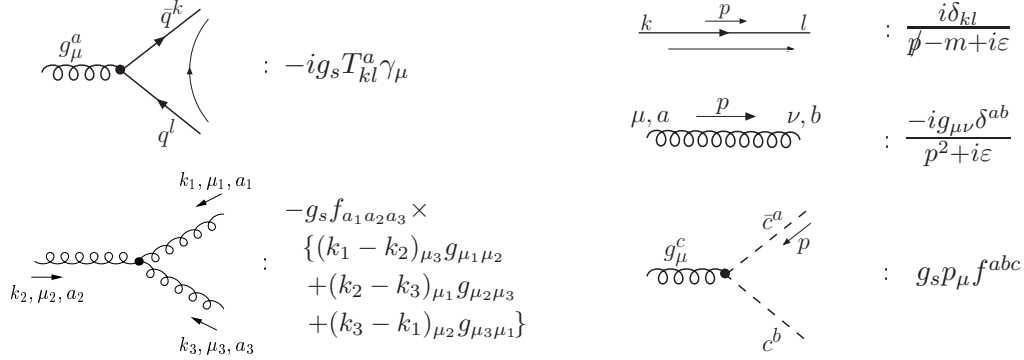


Figure 26: SM QCD Feynman rules. The long thin lines with arrows denote the fermion flow of Ref. [66].

To obtain the Feynman rules with reversed “fermion flow” for diagrams containing Dirac fermions (Fig. 24, $g\bar{q}q$ -vertex and quark propagator in Fig. 26) one has to replace in the above rules the strings of Dirac matrices $\Gamma_i = 1, i\gamma_5, \gamma_\mu\gamma_5, \gamma_\mu, \sigma_{\mu\nu}$ by

$$\Gamma'_i = \eta_i \Gamma_i = C \Gamma_i^T C^{-1} \quad \text{with} \quad \eta_i = \begin{cases} 1 & \text{for } \Gamma_i = 1, i\gamma_5, \gamma_\mu\gamma_5 \\ -1 & \text{for } \Gamma_i = \gamma_\mu, \sigma_{\mu\nu} \end{cases}, \quad (\text{A3})$$

where C denotes the charge conjugation operator. Further rules for dealing with external spinors can be found in Ref. [66].

Appendix B: ANALYTICAL NLO SQCD CORRECTIONS TO $q\bar{q} \rightarrow t\bar{t}$

With the Feynman rules presented in Appendix A and the counterterms of the renormalization procedure as described in Section II B the SQCD one-loop corrections to the $q\bar{q}$ annihilation subprocess can be given in the compact form of Eq. (4). The explicit expressions of the UV finite (after renormalization) gluon self-energy contribution, $\hat{\Pi}(\hat{s})$, is given in Eq. (12) of Section II B. The renormalized $gq\bar{q}$ vertex is parametrized in terms of UV finite (after renormalization) formfactors, F_V, F_M, G_A (introduced in Ref. [29]), describing the vector, magnetic and axial vector parts, respectively. The SQCD one-loop vertex

corrections of Fig. 27 modify these formfactors as follows:

$$\begin{aligned} \frac{\alpha_s}{4\pi} F_V(\hat{s}, m_q) &= \frac{\alpha_s}{4\pi} \sum_{j=1,2} \left\{ -\frac{1}{6} \lambda_j^+ C_{00}(\hat{s}, m_{\tilde{g}}, m_{\tilde{q}_j}, m_{\tilde{q}_j}) \right. \\ &+ \frac{3}{4} \left[\lambda_j^+ (B_0(\hat{s}, m_{\tilde{g}}, m_{\tilde{g}}) - (2C_{00} + (m_q^2 + m_{\tilde{g}}^2 - m_{\tilde{q}_j}^2) C_0)(\hat{s}, m_{\tilde{q}_j}, m_{\tilde{g}}, m_{\tilde{g}})) \right. \\ &\left. \left. - \lambda_j^- 2m_{\tilde{g}} m_q C_0(\hat{s}, m_{\tilde{q}_j}, m_{\tilde{g}}, m_{\tilde{g}}) \right] \right\} + \delta Z_V \end{aligned} \quad (\text{B1})$$

$$\begin{aligned} \frac{\alpha_s}{4\pi} F_M(\hat{s}, m_q) &= \frac{\alpha_s}{4\pi} \sum_{j=1,2} \left\{ \lambda_j^+ \frac{m_q^2}{6} (C_1 + C_2 + C_{11} + C_{22} + 2C_{12})(\hat{s}, m_{\tilde{g}}, m_{\tilde{q}_j}, m_{\tilde{q}_j}) \right. \\ &- \lambda_j^- \frac{1}{6} m_{\tilde{g}} m_q (C_0 + C_1 + C_2)(\hat{s}, m_{\tilde{g}}, m_{\tilde{q}_j}, m_{\tilde{q}_j}) \\ &\left. + \frac{3}{2} m_q^2 \left[\lambda_j^+ (C_1 + C_2 + C_{11} + C_{22} + 2C_{12}) + \lambda_j^- \frac{m_{\tilde{g}}}{m_q} (C_1 + C_2) \right] (\hat{s}, m_{\tilde{q}_j}, m_{\tilde{g}}, m_{\tilde{g}}) \right\} \end{aligned} \quad (\text{B2})$$

$$\begin{aligned} \frac{\alpha_s}{4\pi} G_A(\hat{s}, m_q) &= \frac{\alpha_s}{4\pi} \sum_{j=1,2} \left\{ \frac{1}{6} \lambda_j^A C_{00}(\hat{s}, m_{\tilde{g}}, m_{\tilde{q}_j}, m_{\tilde{q}_j}) + \frac{3}{4} \lambda_j^A [-B_0(\hat{s}, m_{\tilde{g}}, m_{\tilde{g}}) \right. \\ &\left. + (2C_{00} - (m_q^2 - m_{\tilde{g}}^2 + m_{\tilde{q}_j}^2) C_0 - 2m_q^2 (C_1 + C_2))(\hat{s}, m_{\tilde{q}_j}, m_{\tilde{g}}, m_{\tilde{g}}) \right\} + \delta Z_A \end{aligned} \quad (\text{B3})$$

with $\delta Z_{V,A}$ of Eq. (15) and λ_j^\pm , λ_j^A defined in Eq. (A2). The two point functions, $B_0(\hat{s}, m_1, m_2) = B_0(\hat{s}, m_1^2, m_2^2)$, and the three point functions, $[C_l, C_{lm}](\hat{s}, m_1, m_2, m_3) = [C_l, C_{lm}](m_q^2, \hat{s}, m_q^2, m_1^2, m_2^2, m_3^2)$, follow the notation of Ref. [60].

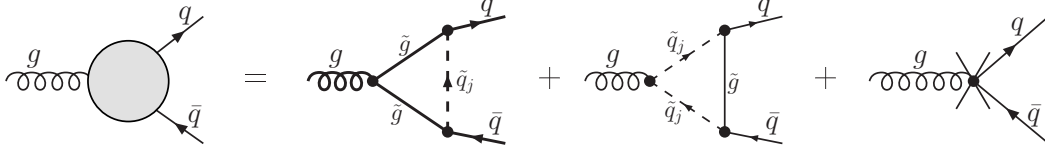


Figure 27: Renormalized gluon-quark-quark vertex correction at NLO Susy-QCD. Graphs containing squarks are summed over the squark mass eigenstates $j=L,R(1,2)$ (no(with) mixing).

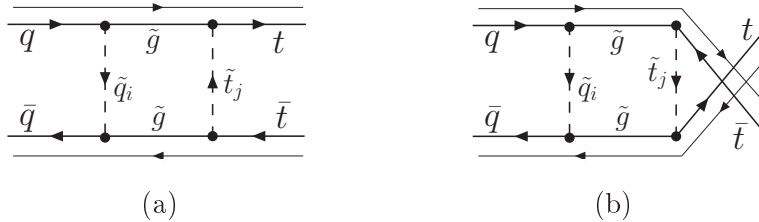


Figure 28: (a) Direct box diagram and (b) crossed box diagram contributing to $q\bar{q} \rightarrow t\bar{t}$ at NLO SQCD, where we explicitly indicate our choice for the fermion flow (see Ref. [66]).

Finally, we provide the explicit expressions for the direct (B_t) and crossed box diagrams (B_u) in $q\bar{q}$ annihilation. To determine the relative sign between the direct and crossed box

diagrams (as well as between box and Born contributions) we apply the rules of Ref. [66]. Fixing the reference order as $t\bar{t}q\bar{q}$ and choosing the fermion flow as indicated in Fig. 28 we only need to assign an additional minus sign to the direct box contribution. Because of differences in previous calculations of the direct and crossed box diagrams in $q\bar{q}$ annihilation, we also provide the explicit expressions for the corresponding matrix elements, $\delta\mathcal{M}_{box}^t$ and $\delta\mathcal{M}_{box}^u$, and of the Born matrix element $\mathcal{M}_B^{q\bar{q}}$:

$$\begin{aligned}\delta\mathcal{M}_{box}^t &= -\int \frac{d^4k}{X(p_2)} \bar{v}_k(p_3) \Gamma_{1,kl}^{a,i} i(-\not{k}-\not{p}_3+m_{\bar{g}}) \Gamma_{2,on}^{a,j} v_n(p_1) \bar{u}_r(p_2) \Gamma_{1,ro}^{b,j} i(\not{p}_4-\not{k}+m_{\bar{g}}) \Gamma_{2,lm}^{b,i} u_m(p_4) \\ \delta\mathcal{M}_{box}^u &= \int \frac{d^4k}{X(p_1)} \bar{v}_k(p_3) \Gamma_{1,kl}^{a,i} i(-\not{k}-\not{p}_3+m_{\bar{g}}) (\Gamma_{1,ro}^{a,j})' v_r(p_2) \bar{u}_n(p_1) (\Gamma_{2,on}^{b,j})' i(\not{p}_4-\not{k}+m_{\bar{g}}) \Gamma_{2,lm}^{b,i} u_m(p_4) \\ \mathcal{M}_B^{q\bar{q}} &= \bar{u}_r(p_2) (-ig_s T_{rn}^a \gamma^\mu) v_n(p_1) \left(-i \frac{g_{\mu\nu}}{\hat{s}} \delta^{ab} \right) \bar{v}_k(p_3) (-ig_s T_{km}^b \gamma^\nu) u_m(p_4)\end{aligned}\quad (\text{B4})$$

with $X(p_i) = (2\pi)^4 [k^2 - m_{\bar{q}_i}^2] [(p_4 - k)^2 - m_{\bar{g}}^2] [(p_3 + k)^2 - m_{\bar{g}}^2] [(p_i + k - p_4)^2 - m_{\bar{t}_j}^2]$, $\hat{s} = (p_3 + p_4)^2$ and $i, j = 1, 2(L, R)$ denoting squark indices, and a, b, k - r color indices. The couplings $\Gamma_{(1,2),kl}^{a,j}$ are specified in Fig. 24 and the momenta of the external particles are defined in Fig. 1. The matrix element for the direct box diagram, $\delta\mathcal{M}_{box}^t$, of Eq. (B4) receives an additional minus sign because of the permutation parity of the spinors with respect to the Born diagram of Fig. 1 that has been chosen as the reference diagram.

Direct box

The Feynman diagram of the direct box is shown in Fig. 28(a). The corresponding spin-like contribution to the NLO SQCD matrix element squared of Eq. (4) reads (with $z = \cos \hat{\theta}$)

$$\begin{aligned}B_t(\hat{s}, \hat{t}, \lambda_t = 1/2, \lambda_{\bar{t}} = 1/2) &= B_t(\hat{s}, \hat{t}, \lambda_t = -1/2, \lambda_{\bar{t}} = -1/2) = \sum_{i,j} \frac{m_t \hat{s}}{16} (1 - z^2) \\ &\times \left\{ A_3^{\bar{q}_i \bar{t}_j} m_t [2m_t^2 (D_0 + 2D_2 + D_{22} + 2D_{13}) - 2\hat{s} \beta_t^2 (D_1 + D_{12}) - \hat{s} (1 + \beta_t^2) D_{11} - 4D_{00}] \right. \\ &\quad \left. + A_2^{\bar{t}_j} m_{\bar{g}} [4m_t^2 (D_0 + D_2) - 2\hat{s} \beta_t^2 D_1] + A_1^{\bar{q}_i \bar{t}_j} 2m_{\bar{g}}^2 m_t D_0 \right\}\end{aligned}\quad (\text{B5})$$

with $[D_l, D_{lm}] = [D_l, D_{lm}](m_t^2, 0, 0, m_t^2, \hat{t}, \hat{s}, m_{\bar{t}_j}^2, m_{\bar{g}}^2, m_{\bar{q}_i}^2, m_{\bar{g}}^2)$ defined in Ref. [60] and depending on the squark flavors i and j . The spin-unlike parts of the direct box can be written as follows

$$\begin{aligned}B_t(\hat{s}, \hat{t}, \lambda_t = 1/2, \lambda_{\bar{t}} = -1/2) &= (B_t^a + B_t^b)(\hat{s}, \hat{t}) \\ B_t(\hat{s}, \hat{t}, \lambda_t = -1/2, \lambda_{\bar{t}} = 1/2) &= (B_t^a - B_t^b)(\hat{s}, \hat{t})\end{aligned}\quad (\text{B6})$$

with

$$B_t^a(\hat{s}, \hat{t}) = \sum_{i,j} \frac{\hat{s}^2}{16} \left\{ A_3^{\bar{q}_i \bar{t}_j} \left[-m_t^2 \beta_t 4z D_1 + \frac{1}{2} m_t^2 (1 - 2\beta_t z + z^2) (2D_2 + D_0 + D_{22}) \right. \right.$$

$$\begin{aligned}
& - (1 + 2\beta_t z + z^2)(m_{\tilde{t}}^2 D_{11} + D_{00}) - 4m_{\tilde{t}}^2 \beta_t z D_{12} + \frac{1}{4} \hat{s}(1 + \beta_t^2)(1 + 2\beta_t z + z^2) D_{13} \Big] \\
& + A_2^{\tilde{t}j} m_{\tilde{g}} m_t [-\beta_t 4z D_1 + (1 - 2\beta_t z + z^2)(D_2 + D_0)] + \frac{1}{2} A_1^{\tilde{q}i\tilde{t}j} m_g^2 (1 - 2\beta_t z + z^2) D_0 \Big\} \\
B_t^b(\hat{s}, \hat{t}) = & \sum_{i,j} \frac{\hat{s}^2}{16} \left\{ A_4^{\tilde{q}i\tilde{t}j} [-2m_{\tilde{t}}^2 \beta_t (1 + z^2)(D_1 + D_{12}) - (\beta_t + 2z + \beta_t z^2)(m_{\tilde{t}}^2 D_{11} + D_{00}) \right. \\
& + \frac{1}{4} \hat{s}(1 + \beta_t^2)(\beta_t + 2z + \beta_t z^2) D_{13} - \frac{1}{2} m_{\tilde{t}}^2 (\beta_t - 2z + \beta_t z^2)(D_0 + 2D_2 + D_{22}) \Big] \\
& + A_2^{\tilde{t}j} A_2^{\tilde{q}i} m_{\tilde{g}} m_t [-2\beta_t (1 + z^2) D_1 - (\beta_t - 2z + \beta_t z^2)(D_2 + D_0)] \\
& \left. + \frac{1}{2} A_5^{\tilde{q}i\tilde{t}j} m_g^2 (\beta_t - 2z + \beta_t z^2) D_0 \right\} \tag{B7}
\end{aligned}$$

The coefficients A_k are defined by the mixing matrices of the squarks occurring inside the loop. In case of a real mixing matrix these coefficients can be expressed in terms of the squark mixing angles $\theta_{\tilde{q}}$ and $\theta_{\tilde{t}}$:

$$\begin{aligned}
A_1^{\tilde{q}i\tilde{t}j} &= 2 \cdot \begin{cases} \cos^2 \theta_{\tilde{q}} \sin^2 \theta_{\tilde{t}} + \sin^2 \theta_{\tilde{q}} \cos^2 \theta_{\tilde{t}} & \text{if } i = j \\ \cos^2 \theta_{\tilde{q}} \cos^2 \theta_{\tilde{t}} + \sin^2 \theta_{\tilde{q}} \sin^2 \theta_{\tilde{t}} & \text{if } i \neq j \end{cases}, \\
A_2^{\tilde{t}j} &= (-1)^j \sin 2\theta_{\tilde{t}}, \\
A_2^{\tilde{q}i} &= -(-1)^i \cos 2\theta_{\tilde{q}}, \\
A_3^{\tilde{q}i\tilde{t}j} &= 2 \cdot \begin{cases} \cos^2 \theta_{\tilde{q}} \cos^2 \theta_{\tilde{t}} + \sin^2 \theta_{\tilde{q}} \sin^2 \theta_{\tilde{t}} & \text{if } i = j \\ \cos^2 \theta_{\tilde{q}} \sin^2 \theta_{\tilde{t}} + \sin^2 \theta_{\tilde{q}} \cos^2 \theta_{\tilde{t}} & \text{if } i \neq j \end{cases}. \\
A_4^{\tilde{q}i\tilde{t}j} &= -[(-1)^j \cos 2\theta_{\tilde{t}} + (-1)^i \cos 2\theta_{\tilde{q}}] \\
A_5^{\tilde{q}i\tilde{t}j} &= -[(-1)^j \cos 2\theta_{\tilde{t}} - (-1)^i \cos 2\theta_{\tilde{q}}] \tag{B8}
\end{aligned}$$

Crossed box

The Feynman diagram of the crossed box is shown in Fig. 28(b). The corresponding spin-like contributions, $B_u(\hat{s}, \hat{t}, \lambda_t = 1/2, \lambda_{\tilde{t}} = 1/2) = B_u(\hat{s}, \hat{t}, \lambda_t = -1/2, \lambda_{\tilde{t}} = -1/2)$, and spin-unlike contributions, $B_u(\hat{s}, \hat{t}, \lambda_t = 1/2, \lambda_{\tilde{t}} = -1/2)$ and $B_u(\hat{s}, \hat{t}, \lambda_t = -1/2, \lambda_{\tilde{t}} = 1/2)$, to the NLO SQCD matrixelement squared of Eq. (4) can be obtained from the expressions for the direct box of Eqs. (B5), (B6) by performing the following replacements:

$$\begin{aligned}
z &\rightarrow -z \\
A_2^{\tilde{q}i} &\rightarrow -A_2^{\tilde{q}i} \\
A_1^{\tilde{q}i\tilde{t}j} &\leftrightarrow A_3^{\tilde{q}i\tilde{t}j} \\
A_4^{\tilde{q}i\tilde{t}j} &\leftrightarrow A_5^{\tilde{q}i\tilde{t}j} \tag{B9}
\end{aligned}$$

and the four point functions D_l and D_{lm} are evaluated at $[D_l, D_{lm}] = [D_l, D_{lm}](m_t^2, 0, 0, m_t^2, \hat{u}, \hat{s}, m_{\tilde{t}_j}^2, m_{\tilde{g}}^2, m_{\tilde{q}_i}^2, m_{\tilde{g}}^2)$.

Appendix C: ANALYTIC EXPRESSIONS FOR THE NLO SQCD CORRECTIONS

TO $gg \rightarrow t\bar{t}$

The Feynman-diagrams of Figs. 5 and 6 represent the SQCD $\mathcal{O}(\alpha_s)$ contributions to the gluon fusion subprocess consisting of the following contributions:

- the modification of the $gt\bar{t}$ -vertex in the s - and $t(u)$ -production channels described by the UV finite (after renormalization) form factors F_V, F_M, G_A and $\rho_i^{V,(t,u)}, \sigma_i^{V,(t,u)}$, respectively,
- the modification of the ggg vertex ($\rho_2^{V,s}$) and the gluon self-energy ($\hat{\Pi}$) in the s production channel,
- the self-energy insertion to the off-shell top quark propagator in the $t(u)$ -production channel ($\rho_i^{\Sigma,(t,u)}, \sigma_i^{\Sigma,(t,u)}$),
- and the box diagrams of the t and u production channels, ($\rho_{i,(a,b,c)}^{\square,t}, \rho_{12}^{\square,gg\bar{t}\bar{t}}, \sigma_{i,(a,b,c)}^{\square,t}$) and ($\rho_{i,(a,b)}^{\square,u}, \sigma_{i,(a,b)}^{\square,u}$), respectively.

The form factors for the $gt\bar{t}$ vertex, F_V, F_M, G_A , and the subtracted gluon self-energy, $\hat{\Pi}$, are provided in Appendix B and Section II B, respectively. The contribution of the renormalized ggg vertex of Fig. 29 to the NLO SQCD matrix element of Eq. (5) reads as follows:

$$\begin{aligned} \frac{\alpha_s}{4\pi} \rho_2^{V,s}(\hat{s}) = & \frac{\alpha_s}{4\pi} \left\{ \sum_{\substack{q=u,c,t \\ d,s,b}} \sum_j \left[\frac{1}{6\hat{s}} (\hat{s} + 8m_{\tilde{q}_j}^2) B_0(\hat{s}, m_{\tilde{q}_j}^2, m_{\tilde{q}_j}^2) - \frac{4m_{\tilde{q}_j}^2}{3\hat{s}} B_0(0, m_{\tilde{q}_j}^2, m_{\tilde{q}_j}^2) \right. \right. \\ & + m_{\tilde{q}_j}^2 C_0(0, \hat{s}, 0, m_{\tilde{q}_j}^2, m_{\tilde{q}_j}^2, m_{\tilde{q}_j}^2) + \frac{5}{18} \left. \right] - 6 \left[\frac{1}{3\hat{s}} (4m_{\tilde{g}}^2 - \hat{s}) B_0(\hat{s}, m_{\tilde{g}}^2, m_{\tilde{g}}^2) \right. \\ & \left. \left. - \frac{4m_{\tilde{g}}^2}{3\hat{s}} B_0(0, m_{\tilde{g}}^2, m_{\tilde{g}}^2) + m_{\tilde{g}}^2 C_0(0, \hat{s}, 0, m_{\tilde{g}}^2, m_{\tilde{g}}^2, m_{\tilde{g}}^2) + \frac{5}{18} \right] \right\} + \delta Z_1 \end{aligned} \quad (C1)$$

with δZ_1 of Eq. (13) and the B_0 and C_0 functions in the convention of Ref. [60].

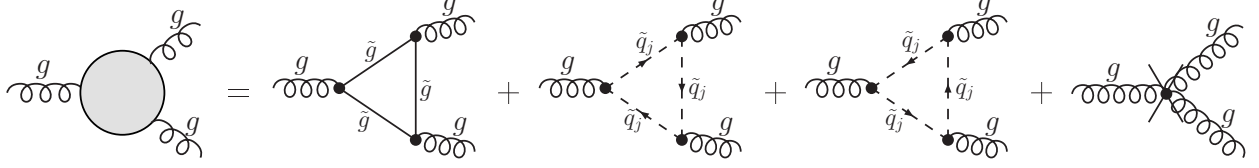


Figure 29: Renormalized gluon-gluon-gluon vertex correction at NLO SQCD. Graphs containing squarks are summed over the squark-mass eigenstates $j=L,R(1,2)$ (no(with) mixing) and the quark flavors $q=\{u,d,s,c,b,t\}$.

1. Parity conserving coefficients to the SMEs $M_i^{V,t}$

The t -channel parity conserving coefficients to the SMEs $M_i^{V,t}$ read as follows:

Vertex corrections:

The vertex corrections consist of the stop-stop-gluino, $\rho_{i,ttg}^{V,t}$, the gluino-gluino-stop, $\rho_{i,ggg}^{V,t}$, contributions and the counterterm, $\rho_{i,CT}$, as shown in Fig. 27:

$$\rho_i^{V,t} = \rho_{i,ttg}^{V,t} + \rho_{i,ggg}^{V,t} + \rho_{i,CT}^{V,t} \quad (C2)$$

with

$$\begin{aligned} \rho_{1,ttg}^{V,t} &= - \sum_{j=1,2} \frac{1}{3} \lambda_j^+ C_{00} \\ \rho_{4,ttg}^{V,t} &= \sum_{j=1,2} \frac{1}{6} \lambda_j^+ (m_t^2 - \hat{t}) (C_2 + C_{22} + C_{12}) \\ \rho_{11,ttg}^{V,t} &= -\rho_{1,ttg}^{V,t} \\ \rho_{14,ttg}^{V,t} &= \sum_{j=1,2} \frac{1}{6} \left\{ \lambda_j^+ (C_{11} + C_{22} + 2C_{12} + C_1 + C_2) - \lambda_j^- \frac{m_{\tilde{g}}}{m_t} (C_0 + C_1 + C_2) \right\} \\ \rho_{16,ttg}^{V,t} &= -4\rho_{14,ttg}^{V,t} \end{aligned} \quad (C3)$$

with $[C_l, C_{lm}] = [C_l, C_{lm}](m_t^2, 0, \hat{t}, m_{\tilde{g}}^2, m_{\tilde{t}_j}^2, m_{\tilde{t}_j}^2)$ of Ref. [60], and

$$\begin{aligned} \rho_{1,ggg}^{V,t} &= \sum_{j=1,2} \frac{3}{2} \left\{ \lambda_j^+ \left[(m_{\tilde{t}_j}^2 - m_t^2 - m_{\tilde{g}}^2) C_0 + (\hat{t} - m_t^2) C_2 - 2C_{00} + B_0(0, m_{\tilde{g}}^2, m_{\tilde{g}}^2) \right] \right. \\ &\quad \left. - 2\lambda_j^- m_{\tilde{g}} m_t C_0 \right\} \\ \rho_{4,ggg}^{V,t} &= \sum_{j=1,2} \frac{3}{2} \lambda_j^+ (m_t^2 - \hat{t}) [C_2 + C_{22} + C_{12}] \\ \rho_{11,ggg}^{V,t} &= \sum_{j=1,2} \frac{3}{2} \left\{ \lambda_j^+ \left[(\hat{t} - m_{\tilde{t}_j}^2 + m_{\tilde{g}}^2) C_0 + (\hat{t} - m_t^2) C_1 + 2C_{00} - B_0(0, m_{\tilde{g}}^2, m_{\tilde{g}}^2) \right] \right\} \end{aligned}$$

$$\begin{aligned}
& + \lambda_j^- \frac{m_{\tilde{g}}}{m_t} (\hat{t} + m_t^2) C_0 \Big\} \\
\rho_{14,gg}^{V,t} &= \sum_{j=1,2} \frac{3}{2} \left\{ \lambda_j^+ (C_{11} + C_{22} + 2C_{12} + C_1 + C_2) + \lambda_j^- \frac{m_{\tilde{g}}}{m_t} (C_1 + C_2) \right\} \\
\rho_{16,gg}^{V,t} &= -4\rho_{14,gg}^{V,t}
\end{aligned} \tag{C4}$$

with $[C_l, C_{lm}] = [C_l, C_{lm}](m_t^2, 0, \hat{t}, m_{\tilde{t}_j}^2, m_{\tilde{g}}^2, m_{\tilde{g}}^2)$ and the counterterm

$$\frac{\alpha_s}{4\pi} \rho_{1,CT}^{V,t} = -\frac{\alpha_s}{4\pi} \rho_{11,CT}^{V,t} = 2\delta Z_V \tag{C5}$$

with δZ_V of Eq. (15). The parameters λ_j^\pm are given in Eq. (A2).

Top quark self-energy insertion:

The self-energy insertion in the off-shell top-quark propagator as shown in Fig. 5 with the SQCD one-loop corrections shown in Fig. 8 is described by:

$$\begin{aligned}
\frac{\alpha_s}{4\pi} \rho_1^{\Sigma,t} &= -(\hat{t} + m_t^2)(\Sigma_V(\hat{t}) + \delta Z_V) - 2m_t^2(\Sigma_S(\hat{t}) - \delta Z_V - \Sigma_S(m_t^2) - \Sigma_V(m_t^2)) \\
\frac{\alpha_s}{4\pi} \rho_{11}^{\Sigma,t} &= 2\hat{t}(\Sigma_V(\hat{t}) + \delta Z_V) \\
&+ (\hat{t} + m_t^2)(\Sigma_S(\hat{t}) - \delta Z_V - \Sigma_S(m_t^2) - \Sigma_V(m_t^2)),
\end{aligned} \tag{C6}$$

where the SQCD one-loop contribution to the vector and scalar parts of the top quark self-energy, $\Sigma_{V,S}$, and δZ_V are provided in Section II B.

Box contribution:

The box diagrams of Fig. 6 can also be parametrized in terms of coefficients to the SMEs $M_i^{V,t}$ as follows:

Box a: $\tilde{g} - \tilde{g} - \tilde{g} - \tilde{t}_j$

$$\begin{aligned}
\rho_{1,a}^{\square,t} &= + \sum_{j=1,2} \left\{ \lambda_j^+ [C_0 + (m_{\tilde{t}_j}^2 - m_t^2 - m_{\tilde{g}}^2) D_0 + (m_{\tilde{g}}^2 - m_t^2) D_2 - 6D_{00}] \right. \\
&- \hat{t} (2D_{22} + D_{222}) - 2(\hat{t} + m_t^2) (D_{12} + D_{122}) - 6D_{002} - 2m_t^2 D_{112} + (\hat{s} - 2m_t^2) D_{123}] \\
&+ \lambda_j^- [-2m_{\tilde{g}} m_t D_0] \Big\} \\
\rho_{2,a}^{\square,t} &= - \sum_{j=1,2} 2\lambda_j^+ [D_{00} + D_{002}] \\
\rho_{4,a}^{\square,t} &= + \sum_{j=1,2} 2\lambda_j^+ [(m_t^2 - m_{\tilde{g}}^2) (D_1 + D_2) + 2D_{00} + m_t^2 (2D_{11} + 2D_{13} + D_{111}) \\
&+ (\hat{t} + m_t^2) D_{22} + (\hat{t} + 5m_t^2) D_{12} + 2(D_{001} + 2D_{002}) \\
&+ \hat{t} D_{222} + (\hat{t} + 3m_t^2) D_{112} + (3\hat{t} + 2m_t^2) D_{122} + (3m_t^2 - \hat{s}) D_{113} + (\hat{t} - \hat{s} + 3m_t^2) D_{123}]
\end{aligned}$$

$$\begin{aligned}
\rho_{6,a}^{\square,t} &= + \sum_{j=1,2} 2\lambda_j^+ [D_{22} + 2D_{12} + D_{222} + 2D_{112} + 4D_{122} + 2D_{123}] \\
\rho_{11,a}^{\square,t} &= - \sum_{j=1,2} \left\{ 2\lambda_j^+ [C_0 + (m_{\tilde{t}_j}^2 - m_{\tilde{g}}^2) D_0 + (\hat{t} + 2m_{\tilde{t}}^2 - m_{\tilde{g}}^2) D_1 \right. \\
&\quad + (\hat{t} + m_{\tilde{t}}^2) (D_{11} + D_{13} + D_{112} + D_{123}) \\
&\quad + \hat{t} (D_2 + 2D_{12} + D_{122}) - 2D_{00} + 6D_{001} + m_{\tilde{t}}^2 D_{111} - (\hat{s} - 3m_{\tilde{t}}^2) D_{113}] \\
&\quad \left. - \lambda_j^- \frac{m_{\tilde{g}}}{m_t} [(m_{\tilde{g}}^2 + m_{\tilde{t}}^2 - m_{\tilde{t}_j}^2) D_0 - 2(\hat{t} + m_{\tilde{t}}^2) D_1 - 2\hat{t} D_2 - C_0] \right\} \\
\rho_{12,a}^{\square,t} &= + \sum_{j=1,2} 4 \left\{ \lambda_j^+ [D_{00} + 2D_{001} + D_{002}] + \lambda_j^- \frac{m_{\tilde{g}}}{m_t} D_{00} \right\} \\
\rho_{14,a}^{\square,t} &= + \sum_{j=1,2} 2 \left\{ \lambda_j^+ [2D_1 + D_2 + 2D_{11} + D_{22} + 4D_{12} + 2D_{13}] \right. \\
&\quad \left. + \lambda_j^- \frac{m_{\tilde{g}}}{m_t} [2D_1 + D_2] \right\} \\
\rho_{16,a}^{\square,t} &= - \sum_{j=1,2} 4 \left\{ \lambda_j^+ [4D_1 + 2D_2 + 3D_{22} + 12D_{12} + 2D_{111} + D_{222}] \right. \\
&\quad + 6(D_{11} + D_{13} + D_{112} + D_{113} + D_{122} + D_{123}) \\
&\quad \left. + \lambda_j^- \frac{m_{\tilde{g}}}{m_t} [4D_1 + 2D_2 + 2D_{11} + D_{22} + 4D_{12} + 2D_{13}] \right\} \tag{C7}
\end{aligned}$$

where the three- and four-point functions are denoted by $C_0 \equiv C_0(0, 0, \hat{s}, m_{\tilde{g}}^2, m_{\tilde{g}}^2, m_{\tilde{g}}^2)$ and $[D_l, D_{lm}, D_{lmn}] = [D_l, D_{lm}, D_{lmn}](m_{\tilde{t}}^2, 0, 0, m_{\tilde{t}}^2, \hat{t}, \hat{s}, m_{\tilde{t}_j}^2, m_{\tilde{g}}^2, m_{\tilde{g}}^2, m_{\tilde{g}}^2)$, respectively.

Box b: $\tilde{t}_j - \tilde{t}_j - \tilde{t}_j - \tilde{g}$

$$\begin{aligned}
\rho_{2,b}^{\square,t} &= - \sum_{j=1,2} 2\lambda_j^+ D_{002} \\
\rho_{4,b}^{\square,t} &= - \sum_{j=1,2} 4\lambda_j^+ [D_{00} + 2D_{001} + D_{002}] \\
\rho_{6,b}^{\square,t} &= + \sum_{j=1,2} 2\lambda_j^+ [D_2 + D_{222} + 2(2D_{12} + D_{22} + D_{112} + D_{123} + 2D_{122})] \\
\rho_{12,b}^{\square,t} &= - \sum_{j=1,2} 4 \left\{ -\lambda_j^+ [2D_{001} + D_{002}] + \lambda_j^- \frac{m_{\tilde{g}}}{m_t} D_{00} \right\} \\
\rho_{16,b}^{\square,t} &= - \sum_{j=1,2} 4 \left\{ \lambda_j^+ [D_2 + D_{222} + 2(D_1 + 2D_{11} + 4D_{12} + 2D_{13} + D_{22} + D_{111}) \right. \\
&\quad + 3D_{112} + 3D_{123} + 3D_{113} + 3D_{122}] \\
&\quad \left. - \lambda_j^- \frac{m_{\tilde{g}}}{m_t} [D_0 + D_{22} + 2(2D_1 + D_2 + D_{11} + 2D_{12} + D_{13})] \right\} , \tag{C8}
\end{aligned}$$

with the 4-point functions $[D_l, D_{lm}, D_{lmn}] = [D_l, D_{lm}, D_{lmn}](m_t^2, 0, 0, m_t^2, \hat{t}, \hat{s}, m_{\tilde{g}}^2, m_{\tilde{t}_j}^2, m_{\tilde{t}_j}^2, m_{\tilde{t}_j}^2)$.

Box c: $\tilde{t}_j - \tilde{t}_j - \tilde{g} - \tilde{g}$ and $\tilde{g} - \tilde{g} - \tilde{t}_j - \tilde{t}_j$

$$\begin{aligned}
\rho_{1,c}^{\square,t} &= - \sum_{j=1,2} 4\lambda_j^+ D_{00} \\
\rho_{2,c}^{\square,t} &= - \sum_{j=1,2} 2\lambda_j^+ [2D_{00} + 2D_{002} + 2D_{003}] \\
\rho_{4,c}^{\square,t} &= - \sum_{j=1,2} 2\lambda_j^+ [-2D_{00} + (m_{\tilde{g}}^2 - m_t^2)(D_1 + D_2) - m_t^2(2D_{11} + 3D_{12} + D_{22}) \\
&\quad - \hat{t}(D_{12} + D_{22}) - 2D_{001} - 2D_{002} - m_t^2(D_{111} + 2D_{112} - 2D_{123} - D_{113} + D_{122} - D_{223}) \\
&\quad - \hat{s}(D_{123} + D_{113}) - \hat{t}(D_{112} + 2D_{123} + D_{113} + D_{222} + 2D_{122} + D_{223})] \\
\rho_{6,c}^{\square,t} &= + \sum_{j=1,2} 4\lambda_j^+ [D_{12} + D_{22} + D_{112} + 2D_{123} + D_{113} + D_{222} + 2D_{122} + D_{223}] \\
\rho_{11,c}^{\square,t} &= + \sum_{j=1,2} 4\lambda_j^+ D_{00} \\
\rho_{12,c}^{\square,t} &= + \sum_{j=1,2} 4 \left\{ \lambda_j^+ [2D_{00} + 2D_{001} + 2D_{002}] + \lambda_j^- \frac{m_{\tilde{g}}}{m_t} 2D_{00} \right\} \\
\rho_{14,c}^{\square,t} &= + \sum_{j=1,2} 2 \left\{ \lambda_j^+ [D_1 + D_2 + D_{11} + 2D_{12} + D_{22}] + \lambda_j^- \frac{m_{\tilde{g}}}{m_t} (D_1 + D_2) \right\} \\
\rho_{16,c}^{\square,t} &= - \sum_{j=1,2} 8 \left\{ \lambda_j^+ [D_1 + D_2 + 2D_{11} + 4D_{12} + 2D_{22} + D_{111} + 3D_{112} + D_{222} + 3D_{122}] \right. \\
&\quad \left. + \lambda_j^- \frac{m_{\tilde{g}}}{m_t} [D_1 + D_2 + D_{11} + 2D_{12} + D_{22}] \right\} . \tag{C9}
\end{aligned}$$

with $[D_l, D_{lm}, D_{lmn}] = [D_l, D_{lm}, D_{lmn}](m_t^2, 0, m_t^2, 0, \hat{t}, \hat{u}, m_{\tilde{t}_j}^2, m_{\tilde{g}}^2, m_{\tilde{g}}^2, m_{\tilde{t}_j}^2)$.

Triangle-box: $\tilde{t}_j - \tilde{t}_j - \tilde{g}$

$$\rho_{12}^{\square,gg\tilde{t}\tilde{t}} = \sum_{j=1,2} \left\{ \lambda_j^+ (C_1 + C_2) - \lambda_j^- \frac{m_{\tilde{g}}}{m_t} C_0 \right\} (m_t^2, \hat{s}, m_{\tilde{t}_j}^2, m_{\tilde{g}}^2, m_{\tilde{t}_j}^2, m_{\tilde{t}_j}^2) . \tag{C10}$$

2. Parity violating coefficients to the SMEs $M_i^{A,t}$

The t -channel parity violating coefficients to the SMEs $M_i^{A,t}$ read as follows:

Vertex corrections:

$$\sigma_i^{V,t} = \sigma_{i,ttg}^{V,t} + \sigma_{i,gg\tilde{t}}^{V,t} + \sigma_{i,CT}^{V,t} \tag{C11}$$

with

$$\sigma_{1,ttg}^{V,t} = - \sum_{j=1,2} \frac{1}{3} \lambda_j^A C_{00}$$

$$\begin{aligned}
\sigma_{4,ttg}^{V,t} &= + \sum_{j=1,2} \frac{1}{6} \lambda_j^A (m_t^2 - \hat{t}) [C_2 + C_{22} + C_{12}] \\
\sigma_{14,ttg}^{V,t} &= - \sum_{j=1,2} \frac{1}{6} \lambda_j^A [C_{11} - C_{22} + C_1 - C_2]
\end{aligned} \tag{C12}$$

with $[C_l, C_{lm}] = [C_l, C_{lm}](m_t^2, 0, \hat{t}, m_{\tilde{g}}^2, m_{\tilde{t}_j}^2, m_{\tilde{t}_j}^2)$ and

$$\begin{aligned}
\sigma_{1,gg t}^{V,t} &= + \sum_{j=1,2} \frac{3}{2} \lambda_j^A \left[(m_{\tilde{t}_j}^2 + m_t^2 - m_{\tilde{g}}^2) C_0 + 2m_{\tilde{t}_j}^2 C_1 + (\hat{t} + m_{\tilde{t}_j}^2) C_2 - 2C_{00} + B_0(0, m_{\tilde{g}}^2, m_{\tilde{g}}^2) \right] \\
\sigma_{4,gg t}^{V,t} &= + \sum_{j=1,2} \frac{3}{2} \lambda_j^A (m_t^2 - \hat{t}) [C_2 + C_{22} + C_{12}] \\
\sigma_{14,gg t}^{V,t} &= - \sum_{j=1,2} \frac{3}{2} \lambda_j^A [C_{11} - C_{22} + C_1 - C_2]
\end{aligned} \tag{C13}$$

with $[C_l, C_{lm}] = [C_l, C_{lm}](m_t^2, 0, \hat{t}, m_{\tilde{t}_j}^2, m_{\tilde{g}}^2, m_{\tilde{g}}^2)$ and the counterterm

$$\frac{\alpha_s}{4\pi} \sigma_{1,CT}^{V,t} = -2\delta Z_A, \tag{C14}$$

where the renormalization constant, δZ_A , is given in Eq. (15). The parameters λ_j^A are given in Eq. (A2).

Top quark self-energy insertion:

$$\frac{\alpha_s}{4\pi} \sigma_1^{\Sigma,t} = (\hat{t} - m_t^2)(\Sigma_A(\hat{t}) + \delta Z_A) \tag{C15}$$

with the axial vector part of the top quark self-energy, Σ_A , of Eq. (14).

Box contribution:

Box a: $\tilde{g} - \tilde{g} - \tilde{g} - \tilde{t}_j$

$$\begin{aligned}
\sigma_{1,a}^{\square,t} &= \sum_{j=1,2} \lambda_j^A \left[C_0 + (m_{\tilde{t}_j}^2 + m_t^2 - m_{\tilde{g}}^2) D_0 + (m_{\tilde{g}}^2 + m_{\tilde{t}_j}^2) D_2 - 6 D_{00} \right. \\
&\quad - \hat{t} (2D_{22} + D_{222}) + 4m_{\tilde{t}_j}^2 D_1 - 2(\hat{t} + m_{\tilde{t}_j}^2) (D_{12} + D_{122}) - 6 D_{002} - 2 m_{\tilde{t}_j}^2 D_{112} \\
&\quad \left. + (\hat{s} - 2m_{\tilde{t}_j}^2) D_{123} \right] \\
\sigma_{2,a}^{\square,t} &= -2 \sum_{j=1,2} \lambda_j^A [D_{00} + D_{002}] \\
\sigma_{4,a}^{\square,t} &= \sum_{j=1,2} 2\lambda_j^A \left[2D_{00} + m_{\tilde{t}_j}^2 (2(D_{11} + D_{13}) + D_{111}) \right. \\
&\quad + (m_{\tilde{t}_j}^2 - m_{\tilde{g}}^2) (D_1 + D_2) + (\hat{t} + 5m_{\tilde{t}_j}^2) D_{12} + 2D_{001} + 4D_{002} + \hat{t} D_{222} + (\hat{t} + 3m_{\tilde{t}_j}^2) D_{112} \\
&\quad \left. + (3\hat{t} + 2m_{\tilde{t}_j}^2) D_{122} + (3m_{\tilde{t}_j}^2 - \hat{s}) D_{113} + (\hat{t} - \hat{s} + 3m_{\tilde{t}_j}^2) D_{123} + (\hat{t} + m_{\tilde{t}_j}^2) D_{22} \right] \\
\sigma_{6,a}^{\square,t} &= \sum_{j=1,2} 2\lambda_j^A [D_{22} + 2D_{12} + D_{222} + 2D_{112} + 4D_{122} + 2D_{123}] \\
\sigma_{14,a}^{\square,t} &= \sum_{j=1,2} 2\lambda_j^A [D_2 + 2D_{12} + D_{22}]
\end{aligned} \tag{C16}$$

with the three- and four-point functions are denoted by $C_0 \equiv C_0(0, 0, \hat{s}, m_g^2, m_g^2, m_g^2)$ and $[D_l, D_{lm}, D_{lmn}] = [D_l, D_{lm}, D_{lmn}](m_t^2, 0, 0, m_t^2, \hat{t}, \hat{s}, m_{\tilde{t}_j}^2, m_g^2, m_g^2, m_g^2)$, respectively.

Box b: $\tilde{t}_j - \tilde{t}_j - \tilde{t}_j - \tilde{g}$

$$\begin{aligned}\sigma_{2,b}^{\square,t} &= - \sum_{j=1,2} 2\lambda_j^A D_{002} \\ \sigma_{4,b}^{\square,t} &= - \sum_{j=1,2} 4\lambda_j^A [D_{00} + 2D_{001} + D_{002}] \\ \sigma_{6,b}^{\square,t} &= \sum_{j=1,2} 2\lambda_j^A [D_2 + D_{222} + 2(2D_{12} + D_{22} + D_{112} + D_{123} + 2D_{122})]\end{aligned}\quad (C17)$$

with the 4-point functions $[D_l, D_{lm}, D_{lmn}] = [D_l, D_{lm}, D_{lmn}](m_t^2, 0, 0, m_t^2, \hat{t}, \hat{s}, m_g^2, m_{\tilde{t}_j}^2, m_{\tilde{t}_j}^2, m_{\tilde{t}_j}^2)$.

Box c: $\tilde{g} - \tilde{g} - \tilde{t}_j - \tilde{t}_j$ and $\tilde{t}_j - \tilde{t}_j - \tilde{g} - \tilde{g}$

$$\begin{aligned}\sigma_{1,c}^{\square,t} &= - \sum_{j=1,2} 4\lambda_j^A D_{00} \\ \sigma_{2,c}^{\square,t} &= - \sum_{j=1,2} 4\lambda_j^A [D_{00} + D_{002} + D_{003}] \\ \sigma_{4,c}^{\square,t} &= \sum_{j=1,2} 2\lambda_j^A [2D_{00} + 2D_{001} + 2D_{002} - m_g^2(D_1 + D_2) \\ &\quad + m_t^2(D_1 + D_2 + 2D_{11} + 3D_{12} + D_{22} + D_{111} + 2D_{112} - 2D_{123} - D_{113} + D_{122} - D_{223}) \\ &\quad + \hat{t}(D_{12} + D_{22} + D_{112} + 2D_{123} + D_{113} + D_{222} + 2D_{122} + D_{223}) + \hat{s}(D_{123} + D_{113})] \\ \sigma_{6,c}^{\square,t} &= \sum_{j=1,2} 4\lambda_j^A [D_{12} + D_{22} + D_{112} + 2D_{123} + D_{113} + D_{222} + 2D_{122} + D_{223}] \\ \sigma_{14,c}^{\square,t} &= \sum_{j=1,2} 2\lambda_j^A [D_1 + D_2 + D_{11} + 2D_{12} + 2D_{13} + D_{22} + 2D_{23}]\end{aligned}\quad (C18)$$

with $[D_l, D_{lm}, D_{lmn}] = [D_l, D_{lm}, D_{lmn}](m_t^2, 0, m_t^2, 0, \hat{t}, \hat{u}, m_{\tilde{t}_j}^2, m_g^2, m_g^2, m_{\tilde{t}_j}^2)$.

Finally, the u -channel contributions $\rho_i^{(V,\Sigma),u}$, $\rho_{i,(a,b)}^{(\square),u}$ and $\sigma_i^{(V,\Sigma),u}$, $\sigma_{i,(a,b)}^{(\square),u}$ can be obtained from the t -channel form factors by replacing \hat{t} with \hat{u} .

3. The color factors

The summation (average) over the color degrees of freedom in the course of the derivation of the parton cross sections leads to the following color factors:

$$\begin{aligned}c^s(1) &= \sum_{\substack{a,b,c; \\ j,l}} (f_{abc} T_{jl}^c) (f_{abd} T_{jl}^d)^* = 3 \sum_{c,d} \delta_{cd} \mathcal{Tr}\{T^c T^d\} = 12 \\ c^t(1) &= \sum_{\substack{a,b,c; \\ j,l}} (iT_{jm}^a T_{ml}^b) (f_{abc} T_{jl}^c)^* = c^s(2) = -6\end{aligned}$$

$$\begin{aligned}
c^u(1) &= \sum_{\substack{a,b,c; \\ j,l}} (iT_{jm}^b T_{ml}^a) (f_{abc} T_{jl}^c)^* = c^s(3) = 6 \\
c^t(2) &= - \sum_{\substack{a,b,c; \\ j,l}} (iT_{jm}^a T_{ml}^b) (-iT_{jm}^a T_{ml}^b)^* = c^u(3) = \frac{16}{3} \\
c^u(2) &= - \sum_{\substack{a,b,c; \\ j,l}} (iT_{jm}^b T_{ml}^a) (-iT_{jm}^a T_{ml}^b)^* = c^t(3) = -\frac{2}{3}
\end{aligned} \tag{C19}$$

and

$$\begin{aligned}
c_a^t(1) &= \sum_{\substack{a,b,c; \\ j,l}} \left(\frac{3}{2} (-iT_{jm}^a T_{ml}^b) - \frac{1}{4} (i\delta_{ab}\delta_{ij}) \right) (f_{abc} T_{jl}^c)^* = \frac{3}{2} c^t(1) \\
c_a^t(2) &= \frac{3}{2} c^t(2) - \frac{1}{4} \sum_{\substack{a,b,c; \\ j,l}} (i\delta_{ab}\delta_{ij}) (-iT_{jm}^a T_{ml}^b)^* = \frac{3}{2} c^t(2) + 1 \\
c_a^t(3) &= \frac{3}{2} c^t(3) - \frac{1}{4} \sum_{\substack{a,b,c; \\ j,l}} (i\delta_{ab}\delta_{ij}) (-iT_{jm}^b T_{ml}^a)^* = \frac{3}{2} c^t(3) + 1 \\
c_b^t(1) &= \frac{1}{6} c^t(1) \\
c_b^t(2) &= \frac{1}{6} c^t(2) + \frac{1}{4} \sum_{\substack{a,b,c; \\ j,l}} (i\delta_{ab}\delta_{ij}) (-iT_{jm}^a T_{ml}^b)^* = \frac{1}{6} c^t(2) - 1 \\
c_b^t(3) &= \frac{1}{6} c^t(3) + \frac{1}{4} \sum_{\substack{a,b,c; \\ j,l}} (i\delta_{ab}\delta_{ij}) (-iT_{jm}^b T_{ml}^a)^* = \frac{1}{6} c^t(3) - 1 \\
c_c^t(1) &= 0 \\
c_c^t(2) &= c_c^t(3) = -\frac{1}{4} \sum_{\substack{a,b,c; \\ j,l}} (i\delta_{ab}\delta_{ij}) (-iT_{jm}^a T_{ml}^b)^* = 1 \\
c_a^u(1) &= \frac{3}{2} c^u(1) \\
c_a^u(2) &= \frac{3}{2} c^u(2) - \frac{1}{4} \sum_{\substack{a,b,c; \\ j,l}} (i\delta_{ab}\delta_{ij}) (-iT_{jm}^a T_{ml}^b)^* = \frac{3}{2} c^u(2) + 1 \\
c_a^u(3) &= \frac{3}{2} c^u(3) - \frac{1}{4} \sum_{\substack{a,b,c; \\ j,l}} (i\delta_{ab}\delta_{ij}) (-iT_{jm}^b T_{ml}^a)^* = \frac{3}{2} c^u(3) + 1 \\
c_b^u(1) &= \frac{1}{6} c^u(1) \\
c_b^u(2) &= \frac{1}{6} c^u(2) + \frac{1}{4} \sum_{\substack{a,b,c; \\ j,l}} (i\delta_{ab}\delta_{ij}) (-iT_{jm}^a T_{ml}^b)^* = \frac{1}{6} c^u(2) - 1 \\
c_b^u(3) &= \frac{1}{6} c^u(3) + \frac{1}{4} \sum_{\substack{a,b,c; \\ j,l}} (i\delta_{ab}\delta_{ij}) (-iT_{jm}^b T_{ml}^a)^* = \frac{1}{6} c^u(3) - 1.
\end{aligned} \tag{C20}$$

-
- [1] F. Abe et al. (CDF Collaboration), Phys. Rev. Lett. **74**, 2626 (1995), hep-ex/9503002.
- [2] S. Abachi et al. (DØ Collaboration), Phys. Rev. Lett. **74**, 2632 (1995), hep-ex/9503003.
- [3] ALEPH, DELPHI, L3, OPAL, and LEPWWG (2005), hep-ex/0511027.
- [4] P. Fayet and S. Ferrara, Phys. Rept. **32**, 249 (1977).
- [5] H. P. Nilles, Phys. Rept. **110**, 1 (1984).
- [6] H. E. Haber and G. L. Kane, Phys. Rept. **117**, 75 (1985).
- [7] J. Wess and J. Bagger, *Supersymmetry and supergravity* (Princeton, USA: University Press (1992) 259 pages, 1992).
- [8] W. M. Yao et al. (Particle Data Group), J. Phys. **G33**, 1 (2006).
- [9] V. Boisvert (CDF Collaboration) (2006), prepared for 20th Rencontres de Physique de La Vallée d'Aoste: Results and Perspective in Particle Physics, La Thuile, Aosta Valley, Italy, 5-12 Mar 2006.
- [10] N. Kidonakis and R. Vogt, Phys. Rev. **D68**, 114014 (2003), hep-ph/0308222.
- [11] M. Cacciari, S. Frixione, M. L. Mangano, P. Nason, and G. Ridolfi, JHEP **04**, 068 (2004), hep-ph/0303085.
- [12] C. Kao and D. Wackerth, Phys. Rev. **D61**, 055009 (2000), hep-ph/9902202.
- [13] W. Bernreuther, M. Fuecker, and Z.-G. Si, Phys. Rev. **D74**, 113005 (2006), hep-ph/0610334.
- [14] I. I. Y. Bigi, Y. L. Dokshitzer, V. A. Khoze, J. H. Kühn, and P. M. Zerwas, Phys. Lett. **B181**, 157 (1986).
- [15] J. H. Kühn, Nucl. Phys. **B237**, 77 (1984).
- [16] M. Beneke et al. (2000), hep-ph/0003033.
- [17] H. M. Georgi, S. L. Glashow, M. E. Machacek, and D. V. Nanopoulos, Ann. Phys. **114**, 273 (1978).
- [18] B. L. Combridge, Nucl. Phys. **B151**, 429 (1979).
- [19] M. Glück, J. F. Owens, and E. Reya, Phys. Rev. **D17**, 2324 (1978).
- [20] J. Babcock, D. W. Sivers, and S. Wolfram, Phys. Rev. **D18**, 162 (1978).
- [21] K. Hagiwara and T. Yoshino, Phys. Lett. **B80**, 282 (1979).
- [22] L. M. Jones and H. W. Wyld, Phys. Rev. **D17**, 1782 (1978).
- [23] P. Nason, S. Dawson, and R. K. Ellis, Nucl. Phys. **B303**, 607 (1988).

- [24] W. Beenakker, H. Kuijf, W. L. van Neerven, and J. Smith, Phys. Rev. **D40**, 54 (1989).
- [25] G. Altarelli, M. Diemoz, G. Martinelli, and P. Nason, Nucl. Phys. **B308**, 724 (1988).
- [26] W. Beenakker, W. L. van Neerven, R. Meng, G. A. Schuler, and J. Smith, Nucl. Phys. **B351**, 507 (1991).
- [27] M. L. Mangano, P. Nason, and G. Ridolfi, Nucl. Phys. **B373**, 295 (1992).
- [28] S. Frixione, M. L. Mangano, P. Nason, and G. Ridolfi, Phys. Lett. **B351**, 555 (1995), hep-ph/9503213.
- [29] W. Beenakker, A. Denner, W. Hollik, T. Mertig, R. Sack, and D. Wackerroth, Nucl. Phys. **B411**, 343 (1994).
- [30] C. Kao, G. A. Ladinsky, and C. P. Yuan, Int. J. Mod. Phys. **A12**, 1341 (1997).
- [31] J. H. Kühn, A. Scharf, and P. Uwer (2005), hep-ph/0508092.
- [32] W. Bernreuther, M. Fuecker, and Z. G. Si, Phys. Lett. **B633**, 54 (2006), hep-ph/0508091.
- [33] S. Moretti, M. R. Nolten, and D. A. Ross, Phys. Lett. **B639**, 513 (2006), hep-ph/0603083.
- [34] S. Moretti, M. R. Nolten, and D. A. Ross (2006), hep-ph/0606201.
- [35] J. H. Kühn, A. Scharf, and P. Uwer (2006), hep-ph/0610335.
- [36] R. Bonciani, S. Catani, M. L. Mangano, and P. Nason, Nucl. Phys. **B529**, 424 (1998), hep-ph/9801375.
- [37] N. Kidonakis, E. Laenen, S. Moch, and R. Vogt, Phys. Rev. **D64**, 114001 (2001), hep-ph/0105041.
- [38] N. Kidonakis and R. Vogt, Int. J. Mod. Phys. **A20**, 3171 (2005), hep-ph/0410367.
- [39] A. Banfi and E. Laenen, Phys. Rev. **D71**, 034003 (2005), hep-ph/0411241.
- [40] W. Bernreuther, A. Brandenburg, and Z. G. Si, Phys. Lett. **B483**, 99 (2000), hep-ph/0004184.
- [41] W. Bernreuther, A. Brandenburg, Z. G. Si, and P. Uwer, Phys. Rev. Lett. **87**, 242002 (2001), hep-ph/0107086.
- [42] W. Bernreuther, A. Brandenburg, Z. G. Si, and P. Uwer, Phys. Lett. **B509**, 53 (2001), hep-ph/0104096.
- [43] W. Bernreuther, A. Brandenburg, Z. G. Si, and P. Uwer, Nucl. Phys. **B690**, 81 (2004), hep-ph/0403035.
- [44] C. Kao, Phys. Lett. **B348**, 155 (1995), hep-ph/9411337.
- [45] J. M. Yang and C. S. Li, Phys. Rev. **D54**, 4380 (1996), hep-ph/9603442.
- [46] J. Kim, J. L. Lopez, D. V. Nanopoulos, and R. Rangarajan, Phys. Rev. **D54**, 4364 (1996),

- hep-ph/9605419.
- [47] W. Hollik, W. M. Mosle, and D. Wackerroth, Nucl. Phys. **B516**, 29 (1998), hep-ph/9706218.
 - [48] M. Beccaria, S. Bentvelsen, M. Cobal, F. M. Renard, and C. Verzegnassi, Phys. Rev. **D71**, 073003 (2005), hep-ph/0412249.
 - [49] A. Stange and S. Willenbrock, Phys. Rev. **D48**, 2054 (1993), hep-ph/9302291.
 - [50] H.-Y. Zhou and C.-S. Li, Phys. Rev. **D55**, 4421 (1997).
 - [51] Z.-H. Yu, H. Pietschmann, W.-G. Ma, L. Han, and J. Yi, Eur. Phys. J. **C9**, 463 (1999), hep-ph/9804331.
 - [52] C.-S. Li, H.-Y. Zhou, Y.-L. Zhu, and J.-M. Yang, Phys. Lett. **B379**, 135 (1996), hep-ph/9606271.
 - [53] C.-S. Li, B.-Q. Hu, J.-M. Yang, and C.-G. Hu, Phys. Rev. **D52**, 5014 (1995).
 - [54] S. Alam, K. Hagiwara, and S. Matsumoto, Phys. Rev. **D55**, 1307 (1997), hep-ph/9607466.
 - [55] Z. Sullivan, Phys. Rev. **D56**, 451 (1997), hep-ph/9611302.
 - [56] D. Wackerroth (1998), hep-ph/9807558.
 - [57] T. Hahn, Comput. Phys. Commun. **140**, 418 (2001), hep-ph/0012260.
 - [58] J. Küblbeck, M. Böhm, and A. Denner, Comput. Phys. Commun. **60**, 165 (1990).
 - [59] T. Hahn, Nucl. Phys. Proc. Suppl. **135**, 333 (2004), hep-ph/0406288.
 - [60] T. Hahn and M. Perez-Victoria, Comput. Phys. Commun. **118**, 153 (1999), hep-ph/9807565.
 - [61] H. L. Lai et al. (CTEQ Collaboration), Eur. Phys. J. **C12**, 375 (2000), hep-ph/9903282.
 - [62] J. C. Collins, F. Wilczek, and A. Zee, Phys. Rev. **D18**, 242 (1978).
 - [63] P. Nason, S. Dawson, and R. K. Ellis, Nucl. Phys. **B327**, 49 (1989).
 - [64] W. F. L. Hollik, Fortschr. Phys. **38**, 165 (1990).
 - [65] J. M. Frere, D. R. T. Jones, and S. Raby, Nucl. Phys. **B222**, 11 (1983).
 - [66] A. Denner, H. Eck, O. Hahn, and J. Küblbeck, Nucl. Phys. **B387**, 467 (1992).
 - [67] G. J. van Oldenborgh and J. A. M. Vermaseren, Z. Phys. **C46**, 425 (1990).
 - [68] M. Jamin and M. E. Lautenbacher, Comput. Phys. Commun. **74**, 265 (1993).
 - [69] T. Hahn and C. Schappacher, Comput. Phys. Commun. **143**, 54 (2002), hep-ph/0105349.
 - [70] S. Heinemeyer, W. Hollik, and G. Weiglein, Phys. Rept. **425**, 265 (2006), hep-ph/0412214.
 - [71] LEP and SLD (LEPEWWG, SLD Electroweak and Heavy Flavour Working Groups), Phys. Rept. **427**, 257 (2006), hep-ex/0509008.
 - [72] V. M. Abazov et al. (DØ Collaboration), Phys. Lett. **B638**, 119 (2006), hep-ex/0604029.

- [73] V. M. Abazov et al. (DØ Collaboration) (2006), hep-ex/0611003.
- [74] A. A. Affolder et al. (CDF Collaboration), Phys. Rev. Lett. **88**, 041801 (2002), hep-ex/0106001.
- [75] A. A. Affolder et al. (CDF Collaboration), Phys. Rev. Lett. **87**, 251803 (2001), hep-ex/0106061.
- [76] T. Stelzer and S. Willenbrock, Phys. Lett. **B374**, 169 (1996), hep-ph/9512292.
- [77] F. Hubaut, E. Monnier, P. Pralavorio, K. Smolek, and V. Simak, Eur. Phys. J. **C44S2**, 13 (2005), hep-ex/0508061.